

ROBUST FAT AND FLUID SUPPRESSION IN MR IMAGING: TECHNICAL  
DEVELOPMENTS AND ADVANCED CLINICAL APPLICATIONS

APPROVED BY SUPERVISORY COMMITTEE

Ananth Madhuranthakam, Ph.D.

---

Elena Vinogradov, Ph.D.

---

Robert Lenkinski, Ph.D.

---

Ivan Pedrosa, M.D., Ph.D.

---

Matthew Lewis, Ph.D.

---

---



## DEDICATION

To my family and friends.

This dissertation is a summary of my Ph.D. work, which has been completed with the generous support and help from many people in the past five years. It is my great honor and pleasure to have these people in my life.

First and foremost, I want to thank my mentor, Dr. Ananth J. Madhuranthakam for his generous support and great mentorship. From him, I have learned how to make discoveries from important details, solve problems with critical thinking, tell a good story of my research and be professional in MR community. I appreciate the training opportunities he gave to me to expand my horizon. I am also grateful for his sincere advice on my research, career and life.

I would like to thank the original and current members of my Graduate Thesis Committee, Dr. Elena Vinogradov, Dr. Matthew Lewis, Dr. Baohong Yuan, Dr. Ivan Pedrosa and Dr. Robert E. Lenkinski. During each committee meeting, they gave me lots of suggestions and feedback on research projects to keep my research moving in the right direction.

I want to thank Dr. Avneesh Chhabra for his support and help with the musculoskeletal MR imaging projects. I am impressed by his quick response to our questions and paper revisions. I would like to thank Dr. Marco C. Pinho and Dr. Joseph Maldjian for their support on the MR neuroimaging. Dr. Pinho gave me lots of suggestions on the image analysis of cervical spine images. I would like to thank Dr. Ivan Pedrosa, Dr. Neil M. Rofsky and Dr. Ali Pirasteh for their time, support and suggestions on the abdominal and whole-body MR imaging projects. Their deep knowledge of clinical body imaging helps me to keep my research focusing on important clinical questions. I also would like to thank Dr. James Brugarolas for referring clinical patients. I would like to thank Dr. Kelli Key for finding volunteers for our research. I also want to thank Trevor Wigal for his great support on human scans. Without the generous support from these clinical collaborators, these research projects would not have been completed.

I am grateful to the Philips collaborators, Dr. Ivan Dimitrov, Dr. Holger Eggers, Dr. Andrea Wiethoff and others for their support and help. Dr. Dimitrov provided me with a lot of help and resources I needed for the development of MR sequences. I also appreciate his advice on the industrial career. I appreciate Dr. Eggers for providing the support on Dixon reconstruction.

I want to thank all the lab members, Josh Greer, Dr. Crystal E. Harrison, Dr. Yue Zhang, Dr. Huajun She, Dr. Ece Ercan, Dr. Quyen Do and Dr. Durgesh Dwivedi for their friendship and support. I enjoyed the discussions with Josh and Crystal on our research as well as the Texas cultures and life. Yue and Huajun gave me many suggestions for research

and shared a lot of life experiences. I enjoyed discussing research and career plans with Ece and Quyen, and I also appreciate their arrangement for lab activities.

I would especially like to thank my lovely wife, Shu Zhang, who is also my closest labmate. I truly appreciate her love and support. I will never forget the time we spend on our research and life. I also appreciate the best Father's Day gift she gave to me, our newborn daughter, Emily. I want to thank my parents and brother for their selfless support and encouragement.

ROBUST FAT AND FLUID SUPPRESSION IN MR IMAGING: TECHNICAL  
DEVELOPMENTS AND ADVANCED CLINICAL APPLICATIONS

by

XINZENG WANG

DISSERTATION

Presented to the Faculty of the Graduate School of Biomedical Sciences

The University of Texas Southwestern Medical Center at Dallas

In Partial Fulfillment of the Requirements

For the Degree of

DOCTOR OF PHILOSOPHY

The University of Texas Southwestern Medical Center at Dallas

Dallas, Texas

August, 2018

Copyright

by

Xinzeng Wang, 2018

All Rights Reserved

ROBUST FAT AND FLUID SUPPRESSION IN MR IMAGING: TECHNICAL  
DEVELOPMENTS AND ADVANCED CLINICAL APPLICATIONS

Publication No. \_\_\_\_\_

Xinzeng Wang, M.S.

The University of Texas Southwestern Medical Center at Dallas, 2018

Supervising Professor: Ananth Madhuranthakam, Ph.D.

Fat and fluid suppression methods are widely used in MR imaging to improve the lesion conspicuity, reduce the artifacts, increase quantification accuracy etc. However, these methods often suffer from either low signal to noise ratio (SNR), incomplete fat suppression or long scan times in some challenging clinical applications, such as MR Neurography, abdominal imaging, whole-body imaging and diffusion-weighted imaging. The research in this thesis aims to improve and develop MR sequences and reconstruction methods for robust fat and fluid suppression in several advanced clinical applications. The first topic of this thesis focuses on improving fat suppression. A frequency offset corrected inversion (FOCI) pulse based short tau inversion recovery (STIR) sequence was developed to improve the fat

suppression in brachial plexus imaging, where large  $B_1$  and  $B_0$  inhomogeneities are often encountered. However, similar to the conventional STIR, it suffers from low SNR. Then, a multi-echo Dixon based variable flip angle TSE sequence was implemented for robust fat suppression with improved SNR and blood suppression, increasing the visualization of brachial plexus. The multi-echo Dixon method was later extended to single shot TSE (SShTSE) sequence to improve the fat suppression in breathhold abdominal imaging, where the commonly used fat suppression method (SPAIR) suffers from incomplete fat suppression due to the large  $B_0$  inhomogeneities. The second topic was simultaneous fat and fluid suppression. A dual-echo 3D TSE sequence combined with multi-echo Dixon was developed to generate simultaneous fat and fluid suppressed images of the cervical spines in a single acquisition. It can also simultaneously generate the standard T2-weighted image, fluid suppressed image and myelogram, significantly reducing the total scan time compared to the current clinical protocols. Then a fast whole-body MR imaging (7 min) sequence was developed for metastatic cancer detection by combining the simultaneous fat and fluid suppression method with the SShTSE acquisition. The images generated from the proposed sequence showed good lesion conspicuity without EPI-associated geometric distortions. Finally, the multi-echo Dixon was implemented with the TSE-based diffusion-weighted imaging sequence, to generate distortion-free diffusion images with improved fat suppression and lesion conspicuity in areas with large  $B_0$  inhomogeneities, such as cervical spinal cord.

## TABLE OF CONTENTS

Chapter One Introduction .....	1
1.1 Introduction.....	1
1.2 Thesis Outline .....	4
Chapter Two Background.....	6
2.1 Overview.....	6
2.2 Basic Physics of MRI.....	6
2.3 Fat Suppression Techniques .....	8
2.3.1 Short Tau Inversion Recovery .....	8
2.3.2 Selective Fat Suppression .....	10
2.3.3 Dixon Method .....	14
2.4 Fluid Suppression Techniques .....	16
2.4.1 Fluid Attenuation Inversion Recovery.....	16
2.4.2 Subtraction based Fluid Suppression.....	17
2.4.3 Diffusion Weighted Imaging .....	20
Chapter Three Frequency Offset Corrected Inversion Pulse for $B_0$ and $B_1$ Insensitive Fat Suppression at 3T.....	22
3.1 Overview.....	22
3.2 Introduction.....	22
3.3 Material and Methods .....	24
3.3.1 Adiabatic Inversion Pulse .....	24
3.3.2 Simulations .....	26

3.3.3 Phantom Study .....	26
3.3.4 In Vivo Study .....	27
3.3.5 Image Evaluation .....	28
3.4 Results .....	29
3.4.1 Simulations .....	29
3.4.2 Phantom Results .....	30
3.4.3 In-Vivo Results .....	31
3.5 Discussion .....	35
<b>Chapter Four MR Neurography of Brachial Plexus at 3T with Robust Fat and Blood</b>	
Suppression .....	39
4.1 Overview .....	39
4.2 Introduction .....	39
4.3 Materials and Methods .....	40
4.3.1 Subjects .....	40
4.3.2 Multi-echo 3D TSE-mDixon .....	41
4.3.3 Homodyne Reconstruction with Phase Preservation .....	42
4.3.4 MRI Experiments .....	43
4.3.5 Image Evaluation .....	45
4.4 Results .....	46
4.5 Discussion .....	51
<b>Chapter Five Volumetric T2-Weighted and “FLAIR-like” Imaging with Uniform Fat</b>	
Suppression in a Single Acquisition: Application to Cervical Spine Imaging .....	54

5.1 Overview.....	54
5.2 Introduction.....	54
5.3 Materials and Methods.....	56
5.3.1 Dual-Acquisition TSE with Dual-Echo Dixon .....	56
5.3.2 Shared-Field-Map Dixon Reconstruction .....	58
5.3.3 Experimental Studies .....	60
5.3.4 Image Processing .....	61
5.3.5 Image Evaluation .....	62
5.4 Results.....	63
5.5 Discussion.....	70
5.6 Conclusion .....	74
 Chapter Six Robust Abdominal Imaging with Uniform Fat Suppression using Dixon based	
Single Shot Turbo Spin Echo.....	75
6.1 Overview.....	75
6.2 Introduction.....	75
6.3 Materials and Methods.....	77
6.3.1 Pulse Sequence.....	77
6.3.2 Image Reconstruction .....	78
6.3.3 Phantom Study.....	79
6.3.4 In Vivo Study.....	80
6.4 Results.....	81
6.5 Discussion.....	88

## Chapter Seven Whole-Body MRI for Metastatic Cancer Detection using T2-Weighted

Imaging with Fat and Fluid Suppression .....	91
7.1 Overview.....	91
7.2 Introduction.....	91
7.3 Theory.....	93
7.3.1 Imaging Sequence .....	93
7.3.2 Image Reconstruction .....	95
7.4 Methods.....	99
7.4.1 Imaging Studies .....	99
7.4.2 Abdominal Imaging .....	100
7.4.3 Whole-Body Imaging of Normal Volunteers .....	100
7.4.4 Whole-Body Imaging of Patients.....	102
7.4.5 Image Evaluation .....	103
7.5 Results.....	103
7.5.1 Simulations .....	103
7.5.2 Shared Field-Map mDixon Reconstruction .....	105
7.5.3 Complex Subtraction .....	106
7.5.4 Whole-Body Imaging of Normal Volunteers .....	108
7.5.5 Whole-Body Imaging of Patients.....	110
7.6 Discussion.....	114
7.7 Conclusion .....	119

## Chapter Eight Diffusion Weighted Imaging using a Dixon based Single Shot Turbo Spin

Echo .....	120
8.1 Overview.....	120
8.2 Introduction.....	120
8.3 Methods and Materials.....	122
8.3.1 Pulse Sequence.....	122
8.3.2 Reconstruction .....	123
8.3.3 Imaging Studies .....	125
8.4 Results.....	127
8.5 Discussion.....	134
8.6 Future .....	138
8.6.1 Hybrid DWI SShTSE Dixon.....	138
8.6.2 Preliminary Imaging Results using Hybrid DWI SShTSE Dixon.....	141
Chapter Nine Discussion and Conclusion.....	146
APPENDIX A Adiabatic Threshold of the C-FOCI Pulse .....	150
Bibliography .....	152

## PRIOR PUBLICATIONS

### Journal Papers

- [1] **Wang X**, Harrison C, Mariappan YK, Gopalakrishnan K, Chhabra A, Lenkinski RE, and Madhuranthakam AJ. MR Neurography of Brachial Plexus at 3.0 T with Robust Fat and Blood Suppression, *Radiology* 283.2 (2017): 538-546 PMID: 28005489; DOI: 10.1148/radiol.2016152842
- [2] **Wang X**, Pirasteh A, Brugarolas J, Rofsky NM, Lenkinski RE, Pedrosa I, and Madhuranthakam AJ. Whole-Body MRI for Metastatic Cancer Detection using T2-Weighted Imaging with Fat and Fluid Suppression, *Magnetic Resonance in Medicine*. 2018;00:1-14 PMID: 29446127; DOI: 10.1002/mrm.27117
- [3] **Wang X**, Greer JS, Dimitrov I, Pezeshk P, Chhabra A and Madhuranthakam AJ. B0 and B1 Insensitive Fat Suppression using Frequency Offset Corrected Inversion Pulse, *Journal of Magnetic Resonance Imaging* (2018), *In Press*.
- [4] Zhang S, Keupp J, **Wang X**, Dimitrov I, Madhuranthakam AJ, Lenkinski RE and Vinogradov E. Z-spectrum appearance and interpretation in the presence of fat: influence of acquisition parameters, *Magnetic Resonance in Medicine* (2017), PMID: 28862349; DOI: 10.1002/mrm.26900
- [5] Zhang S, Seiler S., **Wang X**, Madhuranthakam AJ, Keupp J, Lenkinski RE and Vinogradov E. CEST-Dixon for human breast lesion characterization at 3T: a preliminary study, *Magnetic Resonance in Medicine*, 79(5):2731-2737 (2018). PMID: 29322559; DOI: 10.1002/mrm.27079

## **Patents**

- [6] Madhuranthakam AJ, Wang X. Phase Sensitive Magnetic Resonance Angiography, US Patent, WO2017062470
  
- [7] Madhuranthakam AJ, Wang X, Greer J, Pedrosa I. System and Method for Robust MR Imaging with Prepared Contrast using a Cartesian Acquisition with SPrial Reordering (CASPR), US Provisional Patent Filed (No. 62/480,682)
  
- [8] Madhuranthakam AJ, Wang X, Lenkinski RE. System and Method for Fast T2-Weighted MR Imaging with Fat and Fluid Suppression, US Provisional Patent Filed (No. 62/628,046)

## LIST OF FIGURES

Figure 2-1 Net magnetization, RF pulses and flip angle. ....	7
Figure 2-2 T1 and T2 relaxation curves.....	8
Figure 2-3 STIR sequence and fat suppression.....	10
Figure 2-4 Chemical shift selective method .....	11
Figure 2-5 Spectral presaturation with inversion recovery sequence .....	12
Figure 2-6 Water excitation using the 1-1 binominal pulse.....	13
Figure 2-7 Dixon method.....	15
Figure 2-8 Fluid attenuation inversion recovery sequence .....	16
Figure 2-9 High intensity reduction sequence .....	18
Figure 2-10 Phase-based fluid attenuation.....	19
Figure 2-11 Diffusion weighted imaging.....	20
Figure 3-1 HS and C-FOCI pulse .....	30
Figure 3-2 Fat suppression with 3D-TSE-STIR using HS pulse and C-FOCI pulse.....	31
Figure 3-3 Inversion efficiencies of HS pulse and C-FOCI pulse .....	32
Figure 3-4 Healthy volunteer image acquired using 3D TSE STIR with HS pulse and C-FOCI pulse .....	33
Figure 3-5 3D T2-weighted MR neurography of brachial plexus of a patient .....	34
Figure 3-6 Qualitative assessments of the brachial plexus images acquired using 3D TSE STIR with HS pulse and C-FOCI pulse.....	35
Figure 4-1 Schematic of the multi-acquisition and multi-echo TSE-mDixon.....	42

Figure 4-2 Phantom images acquired using multi-acquisition and multi-echo 2D TSE- mDixon .....	46
Figure 4-3 TSE signal behavior with variable refocusing flip angles .....	47
Figure 4-4 Brachial plexus images of a healthy volunteer acquired with STIR, SPAIR and multi-echo mDixon .....	48
Figure 4-5 Brachial plexus images of a patient acquired with STIR and multi-echo mDixon	49
Figure 4-6 Qualitative and quantitative assessments of brachial plexus images acquired using STIR and multi-echo mDixon.....	50
Figure 5-1 Schematic diagram of the dual-acquisition 3D TSE sequence with dual-echo Dixon.....	57
Figure 5-2 Workflow of shared-field-map mDixon reconstruction.....	63
Figure 5-3 Comparison of shared-field-map mDixon and standard mDixon reconstructions	64
Figure 5-4 Cervical spine images comparing magnitude subtraction and complex subtraction .....	65
Figure 5-5 Cervical spine images acquired using the clinical 2d protocol and the proposed sequence .....	67
Figure 5-6 3D cervical spine images acquired with a larger slice coverage.....	68
Figure 5-7 Quantitative assessments of the performance of dual-acquisition 3D TSE with dual-echo Dixon sequence .....	69
Figure 6-1 Schematic diagram of the SShTSE based multi-echo Dixon sequence .....	78
Figure 6-2 Comparison between bi-directional homodyne and 1D homodyne reconstructions .....	82

Figure 6-3 Phantom images for SNR quantification.....	83
Figure 6-4 Coronal SSHTSE images of a healthy volunteer acquired with/without fat suppression and dual-echo Dixon .....	84
Figure 6-5 Axial SSHTSE images of a healthy volunteer acquired with/without fat suppression and dual-echo SSHTSE-Dixon .....	85
Figure 6-6 Axial SSHTSE images of a patient with liver tumors acquired with/without fat suppression and dual-echo SSHTSE-Dixon .....	86
Figure 7-1 Schematic of the Dual Echo T2-weighted acquisition for Enhanced Conspicuity of Tumors (DETECT) using single-shot turbo spin echo .....	94
Figure 7-2 Flowchart of the image reconstruction for DETECT.....	97
Figure 7-3 Simulated signals of DETECT sequence .....	104
Figure 7-4 Coronal images of a 47-year-old healthy female volunteer’s abdomen .....	105
Figure 7-5 Subtracted brain images comparing magnitude subtraction and complex subtraction.....	107
Figure 7-6 Whole-body MR DETECT images of a healthy volunteer .....	108
Figure 7-7 Whole-body 3D MIP reconstructions of a healthy volunteer comparing DETECT and DWIBS regarding geometric distortions.....	109
Figure 7-8 Whole-body MRI of a 58-year old female patient volunteer with advanced renal cell carcinoma and underwent radiation treatment to the left iliac bone metastatic lesion ..	112
Figure 7-9 Whole-body MRI of a 68-year old male patient volunteer with advanced renal cell carcinoma with a history of prophylactic rod placement and radiation treatment for a right femur metastatic lesion .....	113

Figure 7-10 Whole-body MRI of a 64-year old male patient volunteer with advanced renal cell carcinoma showing improved lesion localization capability of DETECT.....	114
Figure 8-1 DW-SShTSE with phase insensitive diffusion preparation and multi-echo Dixon .....	122
Figure 8-2 Reconstruction pipeline of DW SShTSE with multi-echo Dixon and shared-field-map Dixon.....	124
Figure 8-3 DW SShTSE Dixon with standard reconstruction and shared field map Dixon reconstruction.....	128
Figure 8-4 Axial brain imaging using DW SShTSE Dixon and DW EPI .....	129
Figure 8-5 Diffusion weighted images and ADC maps of sucrose phantoms .....	130
Figure 8-6 ADC measurements of sucrose phantoms.....	131
Figure 8-7 Diffusion weighted imaging of cervical spinal cord .....	132
Figure 8-8 Sagittal diffusion images of a healthy volunteer acquired with DW SShTSE Dixon .....	134
Figure 8-9 Schematic diagram of the hybrid DWI-TSE Dixon and the proposed acquisition order .....	140
Figure 8-10 Phantom results and validation of the hybrid DWI-SShTSE Dixon.....	142
Figure 8-11 Comparison between DWI-TSE Dixon and hybrid DWI-TSE Dixon.....	143
Figure 8-12 Comparison among hybrid DWI-TSE Dixon, DWI-TSE FS and DWI-EPI FS	144
Figure 8-13 High Resolution DWI of cervical spinal cord with hybrid DWI-TSE Dixon...	145

## LIST OF TABLES

Table 4-1 Parameters of the MRN pulse sequences used for the in vivo evaluation of brachial plexus .....	44
Table 4-2 Qualitative Assessment .....	45
Table 5-1 Parameters of the cervical spine pulse sequences .....	60
Table 6-1 Signal-to-noise ratio calculated in the phantom study .....	84
Table 6-2 Assessment of fat suppression: SPAIR vs. mDixon.....	87
Table 7-1 Parameters of the whole body MRI sequences.....	100
Table 7-2 Number of lesions identified on WB-MRI with DETECT compared to WB-MRI with DWIBS in patients .....	110

LIST OF APPENDICES

APPENDIX A ADIABATIC THRESHOLD OF THE C-FOCI PULSE..... 150

## LIST OF DEFINITIONS

$^1\text{H}$	Proton
2D	Two dimensional
3D	Three dimensional
$B_0$	Static magnetic field
$B_1$	Radiofrequency magnetic field
CHESS	Chemical-shift selective
CPMG	Carr-Purcell-Meiboom-Gill
CNR	Contrast-to-noise ratio
CSF	Cerebrospinal fluid
DWI	Diffusion weighted imaging
EPI	Echo planar imaging
ETL	Echo train length
FA	Flip angle
FID	Free induction decay
FLAIR	Fluid attenuation inversion recovery
FOV	Field of view
FOCI	Frequency offset corrected inversion
GM	Gray matter
HS	Hyperbolic secant
IP	In-phase
MIP	Maximum intensity projection

MRI	Magnetic resonance imaging
MRS	Magnetic resonance spectroscopy
NMR	Nuclear magnetic resonance
OP	Out-of-phase
RF	Radio frequency
ROI	Region of interest
RBW	Receiver Bandwidth
SAR	Specific absorption rate
SNR	Signal-to-noise ratio
SPAIR	Spectral presaturation with adiabatic inversion recovery
SPIR	Spectral presaturation with inversion recovery
SShTSE	Single shot turbo spin echo
STIR	Short tau inversion recovery
TE	Echo time
TI	Inversion time
TR	Repetition time
TSE	Turbo spin echo
WM	White matter

# CHAPTER ONE

## Introduction

### 1.1 INTRODUCTION

Over the past decades, various medical imaging modalities have been proposed, developed and applied for the early detection, diagnosis and treatment of diseases with either anatomical information or functional information, or both. Magnetic Resonance Imaging (MRI) is one of the most widely used medical imaging modalities, and it has many advantages over the other imaging modalities. MRI can provide information about many physiological parameters, including tissue components, metabolites concentration, blood flow, oxygen level, temperature and perfusion and diffusion of molecules (1-5). Compared to Computed Tomography (CT), Single Photon Emission Computed Tomography (SPECT) and Positron Emission Tomography (PET), MRI provides excellent and flexible soft-tissue contrasts without using ionizing radiation, which is a major concern in children and repeated follow-up imaging (6-8).

MRI relies on the Nuclear Magnetic Resonance (NMR) phenomenon. Although multiple nuclei ( $^1\text{H}$ ,  $^{13}\text{C}$ ,  $^{31}\text{P}$ ,  $^{23}\text{Na}$  etc.) have magnetic moments, clinical MRI mainly utilizes NMR signals from protons ( $^1\text{H}$ ) because of their high gyromagnetic ratio ( $\gamma$ ) as well as their abundance in the human body (9). Specifically, the MR signals are primarily from the protons of fat and water in tissues (10). Due to the differences in the chemical components, different tissues have different proton density (PD), longitudinal relaxation time (T1) and transverse relaxation time (T2) (11), resulting in MR signal differences and image contrast.

However, if the lesions and background tissues have similar T1 or T2 values, it is challenging to visualize the lesions on the corresponding MR images.

Fat and fluid are widespread in the human body, and many tissues are surrounded by them. Fat with short T1 and long T2 values (12) appears bright on both T1 weighted (T1W) and T2 weighted (T2W) images. In turbo spin echo (TSE) sequence, multiple refocusing pulses can suppress the J-coupling modulation and further increase the T2 of fat. Therefore, fat is brighter on TSE T2W images than conventional spin echo (SE) T2W images (13). Fluids, like cerebrospinal fluid (CSF) and urine etc. contain more free water and less large molecules than other tissues. Therefore, fluids have long T2 values (14) and appear bright on T2W images. The bright signal from fat and fluid can obscure lesions and reduce the conspicuity. To improve the lesion conspicuity, fat and/or fluid suppression is commonly used in clinical MRI (15-18).

Multiple fat and fluid suppression methods have been developed in the past decades. Generally, the fat suppression methods can be divided into three major categories: non-selective short tau inversion recovery (STIR), spectrally selective fat suppression and chemical-shift imaging (Dixon) methods (15,19). STIR is robust against  $B_0$  and  $B_1$  inhomogeneities, but suffers from low SNR. Spectrally selective fat suppression methods such as spectral pre-saturation with (adiabatic) inversion recovery (SPIR/SPAIR) have high SNR, but are sensitive to  $B_0$  inhomogeneities. The Dixon methods are insensitive to  $B_0$  inhomogeneities and can provide uniform fat suppression, but suffers from long scan time or large echo spacing. For fluid suppression, the most frequently used method is the fluid-attenuated inversion recovery (FLAIR) (16). It can provide uniform fluid suppression, but

suffers from long scan time and reduced SNR. The diffusion coefficient of fluid is also high (20), therefore it can be automatically suppressed in diffusion weighted imaging (DWI) at high b-values. However, DWI suffers from low SNR, long scan time and geometric distortions (21,22). Despite these limitations, these fat and fluid suppression methods have been routinely used in many clinical applications. However, novel fat and fluid suppression methods with improved performance are still desirable.

The primary goal of this thesis is to develop robust fat and fluid suppression techniques for advanced clinical applications, in which the performance of the conventional fat and fluid suppression methods are compromised. A frequency offset corrected inversion (FOCI) pulse was implemented as the inversion pulse of STIR to improve the fat suppression at 3T in 3D brachial plexus imaging, where the conventional STIR often fails to completely suppress the fat due to large  $B_1$  and  $B_0$  inhomogeneities. A variable-flip-angle TSE based multi-echo Dixon was then implemented for the 3D brachial plexus imaging to achieve robust fat suppression as well as improve SNR and blood suppression compared to 3D STIR. Then, dual-acquisition TSE was combined with the multi-echo Dixon to achieve simultaneous fat and fluid suppression as well as to generate multiple contrast images without increasing the scan time in 3D cervical spine imaging. Thereafter, the multi-echo Dixon method was extended to the single-shot TSE (SShTSE) sequence to improve the fat suppression in breathhold abdominal imaging. The simultaneous fat and fluid suppression method was also extended to whole-body MRI to improve the lesion conspicuity for metastatic cancer imaging. The multi-echo Dixon was finally implemented in TSE-based DWI to improve the fat suppression for cervical spinal cord imaging.

## 1.2 THESIS OUTLINE

Chapter 2 provides a brief overview of fundamental principles of the commonly used fat and fluid suppression methods. The origin of the artifacts is also analyzed.

Chapter 3 describes the FOCI pulse based 3D STIR sequence for 3D brachial plexus imaging. The FOCI pulse is compared with the commonly used hyperbolic secant (HS) pulse theoretically and experimentally.

Chapter 4 presents the 3D variable-flip-angle TSE based multi-echo Dixon with partial echo acquisition for 3D brachial plexus imaging. Multi-echo Dixon shows robust fat suppression as well as improved SNR compared to 3D STIR. Variable-flip-angle TSE also suppresses the signal from the blood to improve nerve visualization.

Chapter 5 describes the simultaneous fat and fluid suppression method by combining the dual-acquisition TSE and multi-echo Dixon. Shared-field-map Dixon was developed to improve the fat suppression in long TE images, in which conventional water-fat separation reconstruction method failed to separate the water and fat due to low SNR. The application of the simultaneous fat and fluid suppression method in 3D cervical spine imaging is presented.

Chapter 6 describes the SSHTSE based multi-echo Dixon for breathhold abdominal imaging. This method is compared with the commonly used SPAIR, and shows improved fat suppression.

Chapter 7 describes the SSHTSE based simultaneous fat and fluid suppression method for metastatic cancer detection using whole body MRI. This method is evaluated in patients with metastatic renal cell carcinoma and compared with whole-body DWI.

Chapter 8 describes the TSE based DWI sequence with multi-echo Dixon. This sequence can generate DW images with robust fat suppression and reduced geometric distortions. The application on the DWI of the cervical spinal cord is presented.

Chapter 9 discusses the advantages and limitations of the proposed methods, as well as the potential solutions as well as the future applications.

## CHAPTER TWO

### Background

#### 2.1 OVERVIEW

This chapter provides the basic physics of magnetic resonance imaging, as well as the previously developed fat and fluid suppression methods. The advantages and disadvantages of these methods are discussed.

#### 2.2 BASIC PHYSICS OF MRI

In the external magnetic field ( $B_0$ ), nuclei with non-zero spins ( $I \neq 0$ ) have different energy states, and a small fraction of spins favor lower-energy state at equilibrium, generating a net magnetization ( $\mathbf{M}$ ).  $\mathbf{M}$  points along the positive z-axis at equilibrium, as shown in Figure 2-1a. For the spin-1/2 system, the magnitude of the net magnetization is

$$|\mathbf{M}| = \frac{\gamma^2 \hbar^2 B_0 N}{4KT} \quad \text{Equation 2.1}$$

where  $\hbar$  is the reduced Planck's constant,  $N$  is total number of spins,  $K$  is the Boltzmann's constant and  $T$  is the absolute temperature (23,24). Equation 2.1 suggests that the magnetization is proportional to  $B_0$ . Larger magnetic field,  $B_0$ , will generate larger magnetization and higher signal to noise ratio (SNR). Besides the magnetization, the resonance frequency of a spin system also depends on the  $B_0$ ,  $\omega_0 = \gamma B_0$ . When  $B_0$  is not homogeneous or the chemical environment is different, the resonance frequency of the nucleus will have relative shifts,  $\omega = \omega_0(1 - \delta)$ .  $\delta$  is a shielding constant and usually measured in parts per million (ppm). For example, the main spectral peak for fat shifts 3.4 ppm from water peak (25,26).

To generate the MR signal, the net magnetization has to be tipped away from the longitudinal direction using a magnetic field ( $B_1$ ) orthogonal to the  $B_0$  to create a transverse component ( $M_{xy}$ ), as shown in Figure 2-1b. The flip angle ( $\theta$ ) depends on the strength of the  $B_1$  field, which is associated with the power of the radiofrequency (RF) pulse. Since the measured signal ( $S$ ) from the receiver coil is proportional to the  $M_{xy}$ , a uniform  $B_1$  field is desired to reduce the signal variation in MR images.

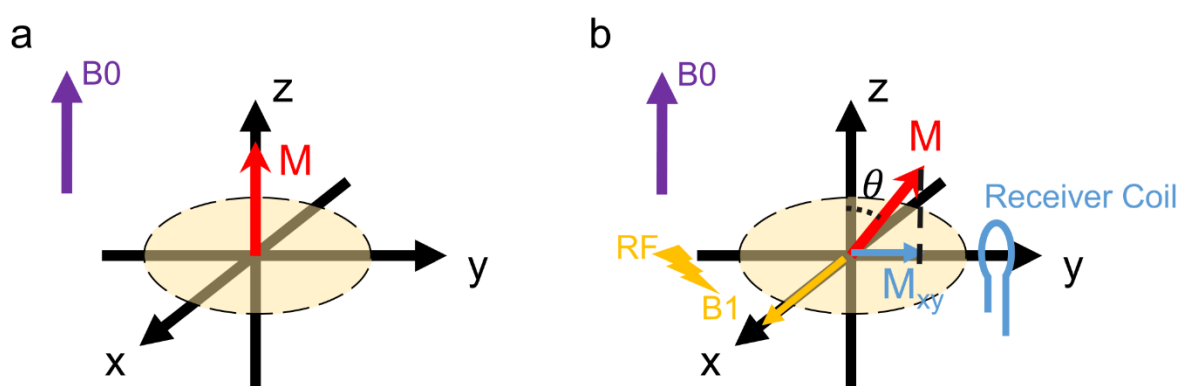


**Figure 2-1 Net magnetization, RF pulses and flip angle.**

The net magnetization at equilibrium (a) and after an excitation RF pulse with a flip angle of  $\theta$  (b).

After the perturbation,  $M$  will return to the equilibrium state by two important and independent relaxation processes, longitudinal ( $T_1$ ) relaxation and transverse ( $T_2$ ) relaxation that are modeled as exponential growth with a time constant  $T_1$  and exponential decay with a time constant  $T_2$  respectively, as shown in Figure 2-2.  $T_1$  and  $T_2$  relaxation times are the inherent tissue properties and are the source of contrasts in  $T_1$ -weighted ( $T_1W$ ) and  $T_2$ -weighted ( $T_2W$ ) MR images. For example, fat has a relatively short  $T_1$  relaxation time ( $\sim 380$  ms) and a relatively long  $T_2$  relaxation time ( $\sim 70$  ms) at 3.0 T (12,27). However, fluid, such

as CSF has a relatively long T1 relaxation time (~4100 ms) and a very long T2 relaxation time (~2000 ms) (14,28,29).

The differences in resonance frequency, T1 and T2 relaxation times not only can generate image contrasts, but also can provide a way to selectively suppress certain tissues, like fat and fluid.

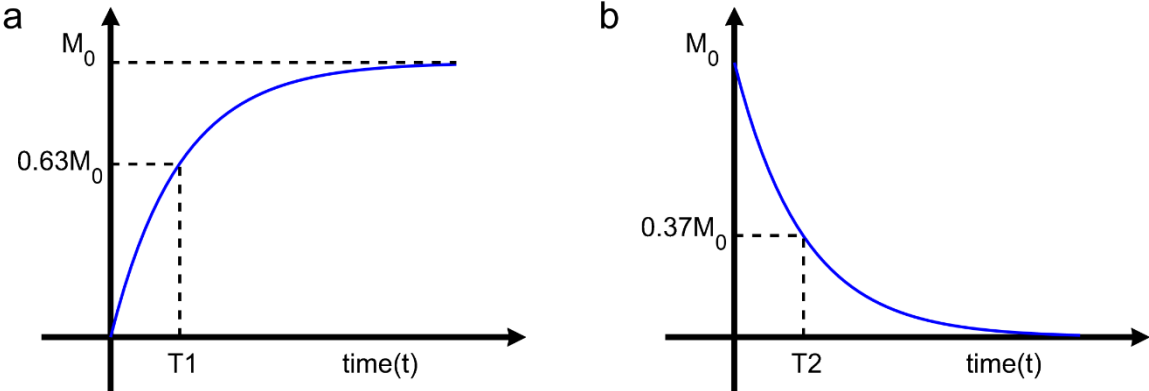


**Figure 2-2 T1 and T2 relaxation curves.**

(a) If the initial magnetization  $M_z$  is zero, the longitudinal magnetization will recover to its equilibrium value ( $M_0$ ) with a relaxation time constant  $T_1$ . (b) If the initial transverse magnetization  $M_{xy}$  equals to  $M_0$ , it will decay to zero with a relaxation time constant  $T_2$ .

### 2.3 FAT SUPPRESSION TECHNIQUES

#### 2.3.1 Short Tau Inversion Recovery

Short tau inversion recovery (STIR) is a simple and widely used fat suppression technique (5,15,19,30). The suppression of the fat signal is based on the T1 relaxation time. A TSE-based STIR sequence is shown in Figure 2-3a. A non-selective pre-inversion pulse with broad bandwidth affecting both fat and water (Fig. 2-3b) is used in front of the

acquisition. During the inversion time (TI) interval, both fat and water experience T1 relaxation to recover to their initial equilibrium state. Due to the short T1, fat recovers faster than water, and reaches the null point earlier, as shown in Figure 2-3c. TI is approximately 180 ms at 1.5T, while it is about 230 ms at 3T due to a longer T1 at 3T. If an excitation pulse is applied at the null point of fat, only the signal from water presents in the image, therefore the fat is suppressed. Since a non-selective inversion pulse is used, STIR is insensitive to B0 inhomogeneity.

If fat is fully inverted, the magnetization after the inversion pulse  $M_{inv} = -M_{init}$ , and the inversion efficiency  $f = 1$ . In reality, it is challenging to achieve uniform B<sub>1</sub> field, especially for a large field of view (FOV). B<sub>1</sub> inhomogeneities will reduce the inversion efficiency. If  $f < 1$ , fat and water will reach their null points earlier, resulting in the residual fat signal as well as nulled water signal at the point of excitation, as shown in Figure 2-3d. To address this challenge, an adiabatic inversion pulse is usually used as the pre-inversion STIR pulse because of its insensitivity to B1 inhomogeneities.

A major drawback of STIR is low SNR. As shown in Figure 2-3c, the magnitude of the magnetization of water at the null point is smaller than that at equilibrium state. Since the signal is proportional to the magnitude of the magnetization, the SNR of STIR images is lower than the SNR of the images acquired without the inversion pulse.

For T2W TSE sequence, STIR will also modify the image contrast. The inversion recovery will impart a heavy T1 weighting in addition to the T2 weighting. While, this can affect the quantification, for lesions with long T1 and long T2, STIR can further increase the contrast compared to the conventional T2W image.

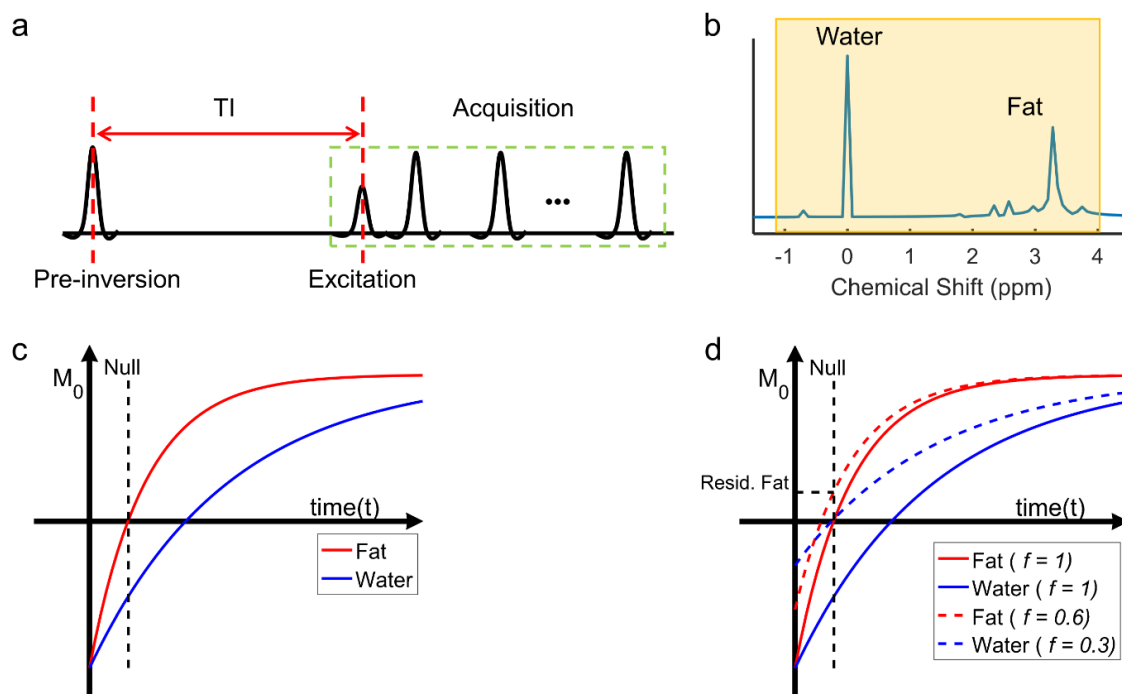


**Figure 2-3 STIR sequence and fat suppression.**

(a) A schematic diagram of a STIR pulse sequence. (b) The pre-inversion pulse has a broad bandwidth and inverts both fat and water. Illustration of  $M_z$  recovery in STIR with efficient inversion (c) and inefficient inversion (d).

Another drawback of STIR is that it does not specifically suppress the fat tissue, since STIR is solely based on the T1 relaxation time. Pathology and contrast agents can change the T1 of tissues, and thus STIR will suppress all the tissues that have similar T1 values to that of fat.

### 2.3.2 Selective Fat Suppression

To selectively suppress the fat and improve the SNR, selective fat suppression methods have been proposed based on the chemical shift of fat. These methods include

chemical shift selective (CHESS) method, spectral presaturation with inversion recovery (SPIR), spectral adiabatic inversion recovery (SPAIR) and water excitation.

### 2.2.2.1 CHESS

As shown in Figure 2-4, instead of using a non-selective inversion pulse, CHESS utilizes a narrow-band  $90^\circ$  pulse, which tips the magnetization of the fat into the transverse plane (31). Following the  $90^\circ$  pulse, a spoiler gradient is immediately applied to dephase the magnetization of fat. Then, only the magnetization of water is excited, and the signal from water is acquired.

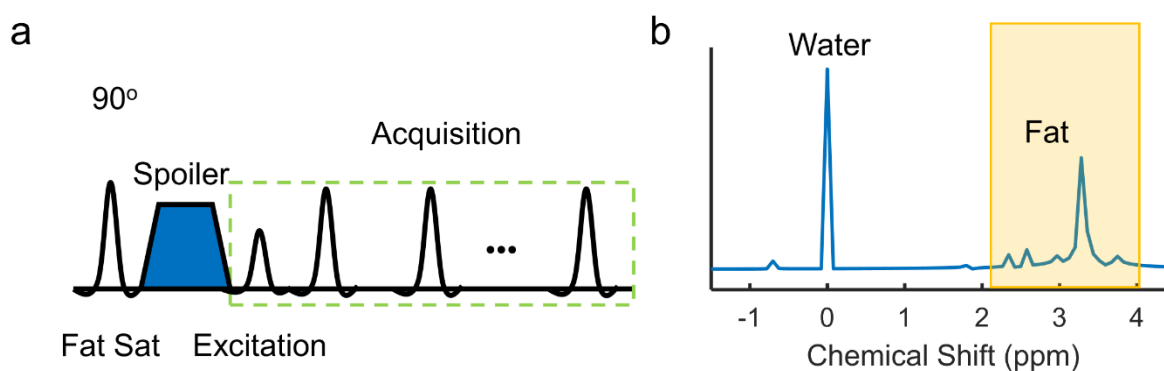


**Figure 2-4 Chemical shift selective method**

(a) A schematic diagram of a CHESS pulse sequence. (b) The saturation pulse selectively saturates the signal from fat.

The amount of fat suppression and the uniformity using CHESS depends on the efficiency of the fat suppression pulse. In practice, it is challenging to achieve a perfect  $90^\circ$ -degree rotation of fat across the entire FOV. The residual longitudinal magnetization of fat cannot be destroyed by the spoiler gradient, resulting in incomplete fat suppression.

Due to the narrow bandwidth of the saturation pulse, CHESS is sensitive to  $B_0$  inhomogeneities. In the high field or in the presence of the metal implant, the fat suppression is inadequate using CHESS.

#### 2.2.2.2 SPIR and SPAIR

Unlike CHESS using  $90^\circ$  pulse, a narrow-band inversion pulse ( $100^\circ - 180^\circ$ ) is used in SPIR (32). For the magnetization of fat, the transverse component is dephased by the spoiler gradient, and the longitudinal component is nulled by the T1 recovery during the TI interval. In most implementations, the flip angle of the inversion pulse is slightly greater than  $90^\circ$  and around  $110^\circ$ . This can help to reduce the duration of TI. Similar to CHESS, it is still sensitive to  $B_1$  and  $B_0$  inhomogeneities.

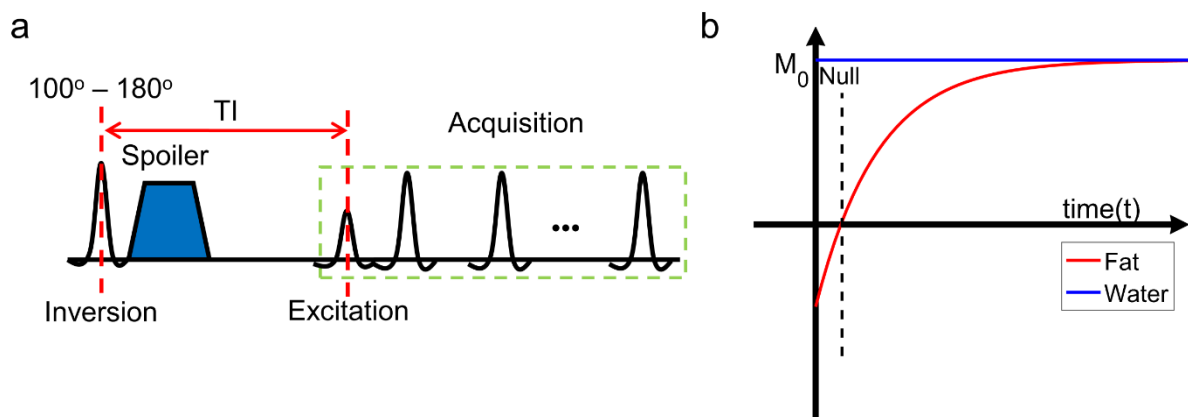


**Figure 2-5 Spectral presaturation with inversion recovery sequence**

(a) A schematic diagram of a SPIR pulse sequence. (b) The inversion pulse selectively inverts the magnetization of fat. The signal is acquired at the null point of fat.

To reduce the  $B_1$  sensitivity, SPAIR is often used. SPAIR uses a narrow-band adiabatic inversion pulse to selectively invert the magnetization of fat (33). However, the flip

angle of the adiabatic inversion pulse is  $180^\circ$ , therefore a longer TI is required. SPAIR is still sensitive to  $B_0$  inhomogeneities.

### 2.2.2.3 Water Excitation

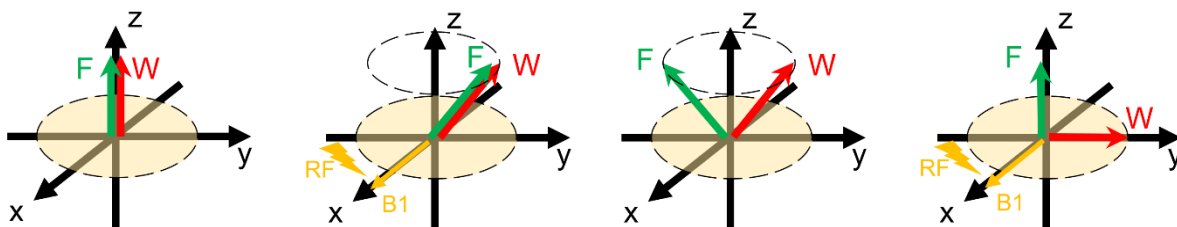


**Figure 2-6 Water excitation using the 1-1 binominal pulse**

After the first  $45^\circ$  excitation pulse, water and fat protons have the same phase. During the time interval between the two pulses, the spins of water and fat go out of phase due to the chemical shift. When they have a  $180^\circ$  phase difference, the second  $45^\circ$  excitation pulse will be applied to flip the magnetization of fat back to the z-axis and to flip the magnetization of water into transverse plane completely.

In the above selective fat suppression methods, the magnetization of fat is inverted while that of water is left alone. Water excitation selectively excites water protons and fat protons are left alone. In water excitation, composite pulses are commonly used as the spatial spectral selective pulses (34,35). As shown in Figure 2-6, the first excitation pulse of a typical 1-1 water excitation pulse will excite both fat and water protons with a flip angle of  $45^\circ$ . After a short delay, fat and water will have  $180^\circ$  phase difference due to the chemical shift. At this time point, a second  $45^\circ$  excitation pulse will be applied to tip the fat back to the longitudinal axis and tip the water into the transverse plane. Then the signal is acquired, and only the signal from water presents in the image.

Water excitation is insensitive to  $B_1$  inhomogeneity since the effective excitation at the resonance frequency of fat is 0 regardless of the exact flip angles of the excitation pulses.

(36) The  $B_1$  will only affect the signal intensity of water. However, water excitation is still sensitive to the  $B_0$  inhomogeneity since the selective excitation relies on the phase shift, which depends on the inter-pulse delay and the local  $B_0$ .

### 2.3.3 Dixon Method

Previous fat suppression methods focus on magnetization preparation and excitation, while Dixon method is based on the signal acquisition (37-41). As shown in Figure 2-7, water and fat spins have the same phase in the transverse plane immediately after the excitation. Since water and fat spins have different resonance frequencies, they will have  $180^\circ$  phase difference after time  $\tau$ , which is about 2.2 ms at 1.5T and 1.1 ms at 3T. The image acquired at this time point is known as out-of-phase (OP) image. After another time  $\tau$ , the phase difference between water and fat spins will be 0, generating the in-phase (IP) image.

The MR signal ( $S$ ) acquired at time point  $n$  can be modulated as,

$$S_n = (W + c_n F) e^{i\varphi_n} \quad \text{Equation 2.2}$$

with

$$c_n = \sum_m w_m e^{i(2\pi\Delta f_m + iR_m)\Delta t_n} \quad \text{Equation 2.3}$$

where  $W$  and  $F$  are signals from water and fat respectively,  $m$  is the index of the spectral peaks of fat with a weighting factor  $w_m$ , off-resonance frequency  $\Delta f_m$  and transverse relaxation rate  $R_m$ ,  $\Delta t_n$  is the echo time, and  $\varphi$  is the phase error due to the  $B_0$  inhomogeneity. Besides  $W$  and  $F$ , multiple unknowns ( $w_m$ ,  $\Delta f_m$ ,  $R_m$  and  $\varphi$ ) affect the

acquired signals, as shown in Equation 2.2. Therefore, signals at multiple different echo times are required to separate the  $W$  and  $F$ , and these methods are often referred to as multi-point Dixon.

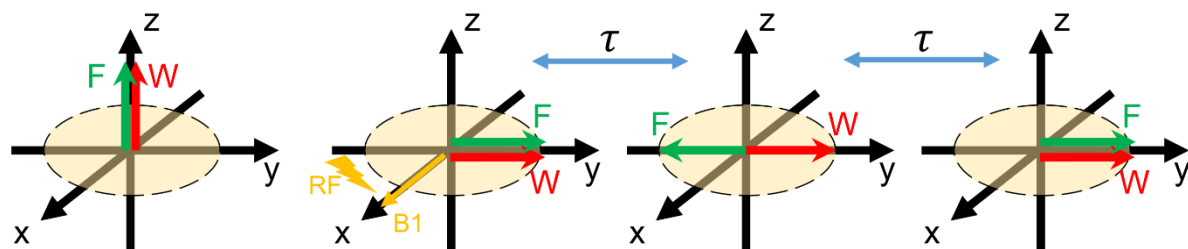


**Figure 2-7 Dixon method**

Vector diagram illustrating the principle of the basic Dixon method: water and fat have the same phase immediately after the excitation; the signal acquisitions are separated by a time  $\tau$ , during which the spins of fat and water are out-of-phase (OP) or in-phase (IP) with each other.

For fat suppression, two-point Dixon is commonly used because of short scan time. To separate fat and water based on Equation 2.2, multiple assumptions have to be made with dual-echo Dixon. First, the phase error  $\Delta\varphi = \varphi_1 - \varphi_2$  is assumed to be spatially smooth. Multiple methods, including region growing (42), graph cut (41,43) and tree-reweighted message-passing (TRW-S) (44) etc. have been proposed to estimate the  $\Delta\varphi$ . Second, it is often assumed that all fat signal comes from the dominant peak. Although fat has multiple spectral peaks, the dominant peak accounts for 63% of the total signal. However, this will result in “gray” fat due to incomplete water-fat separation. Multi-peak models are now widely used to improve the water-fat separation in two- or three-point Dixon based on the assumption that all the fat tissues have same spectra and relaxation parameters. Hence,  $w_m$ ,

$R_m$  and  $\Delta f_m$  can be pre-estimated using other methods like MR spectroscopy and assumed to be known parameters. Then,  $W$  and  $F$  can be calculated based on the measured signal  $S_n$  and the estimated phase error  $\Delta\varphi$ .

Since Dixon methods are based on acquisition, they are insensitive to  $B_1$  inhomogeneity. The phase error due to  $B_0$  inhomogeneity is estimated before water-fat separation, therefore they are also insensitive to  $B_0$  inhomogeneity. Although the assumption that the phase error is spatially smooth can be violated in certain cases, such as in the presence of the metal implant, the phase error can be treated as an unknown and be estimated correctly by using three- or seven-point Dixon methods, at the expense of increased scan time.

## 2.4 FLUID SUPPRESSION TECHNIQUES

### 2.4.1 Fluid Attenuation Inversion Recovery

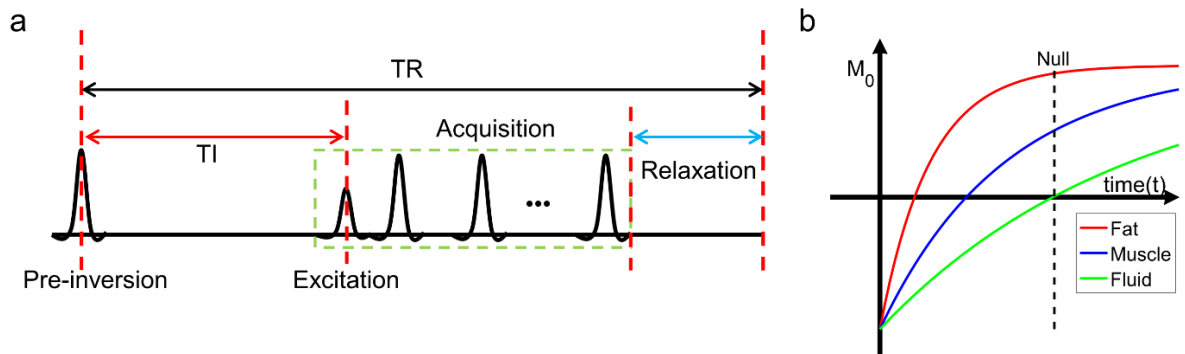


**Figure 2-8 Fluid attenuation inversion recovery sequence**

(a) A schematic diagram of a FLAIR pulse sequence. (b) The signals are acquired at the null point of the fluid.

Similar to STIR, Fluid Attenuated Inversion Recovery (FLAIR) is also based on inversion recovery, but the TI is set to null the signal from the fluid as shown in Figure 2-8. Since fluid has a very long T1, most tissues will pass their zero crossing points before fluid. FLAIR is commonly used in brain and spinal cord imaging, in which abnormalities like multiple sclerosis remain bright but CSF is dark.

Since the T1 of fluid is very long, TI is dependent on both TR and T1 (45), as shown in Equation 2.4.

$$TI = T1[\ln 2 - \ln(1 + e^{-(TR-TE_{last})/T1})] \quad \text{Equation 2.4}$$

where TR is the repetition time and  $TE_{last}$  is the time of the last echo. Usually, TI is about 800-1200 ms, and the TR is more than 2000 ms. Therefore, the total scan time of FLAIR is long. At the null point of the fluid, the tissues with long T1 are still recovering and not yet at their equilibrium state, reducing the SNR.

## 2.4.2 Subtraction based Fluid Suppression

### 2.3.2.1 High Intensity Reduction

Besides a long T1, fluid also has a very long T2, resulting in a strong signal at long TE. A subtraction based fluid suppression method, high intensity reduction (HIRE) method has been developed based on the T2 relaxation (46,47). As shown in Figure 2-9a, HIRE acquires two images at different TEs, short TE (TE1) and long TE (TE2). The signal from fluid decays slowly, while the signals from other tissues decay to zero, shown in Figure 2-9b. When the long TE image is subtracted from the short TE image, the signal from the fluid can be attenuated.

HIRE can generate standard T2W image, heavily T2W image and the fluid attenuated image. FLAIR provides T1 contrast because of the T1 recovery, while HIRE can reserve the T2 contrast. However, the direct magnitude subtraction may result in incomplete fluid suppression and subtraction artifacts as well as affecting the signal from tissue with moderate long T2, such as tumors (48).

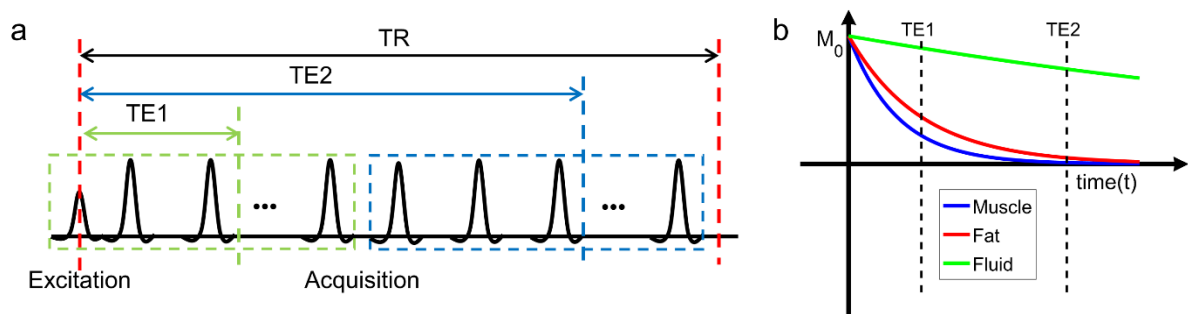


**Figure 2-9 High intensity reduction sequence**

(a) A schematic diagram of a HIRE pulse sequence. Two images are acquired at different TEs, short TE ( $TE_1$ ) and long TE ( $TE_2$ ). (b) The fluid has a long T2 and decays slower than fat and muscle. The fluid free image can be created by subtracting the long-TE image from the short-TE image.

### 2.3.2.2 Phase-based Fluid Attenuation

Phase-based fluid attenuation takes advantage of both long T1 and T2 to suppress the signal from fluid (48). As shown in Figure 2-10a, two images are acquired in the same TR, and the two acquisitions are separated by a short time delay (TD). The net magnetization vectors are shown in Figure 2-10b to explain the principle of the fluid suppression using the phase-based fluid attenuation method. During the first acquisition, all the protons have the same phase, and the transverse magnetization of non-fluid protons decays faster than that of fluid protons. After the first acquisition, a  $90^\circ$  pulse flips all the magnetization to the  $-z$ -axis.

Due to a short T1, the longitudinal magnetization of non-fluid protons recovers faster than that of fluid protons and is positive before the second excitation. After the second excitation, the transverse magnetization of fluid protons in the second acquisition will have 180° phase shift compared to that in the first acquisition, while the phase of the transverse magnetization of non-fluid protons remains the same. The fluid with long T1 and T2 can be suppressed by weighted averaging the two images, since the signal from the fluid can be “subtracted” from the first image.

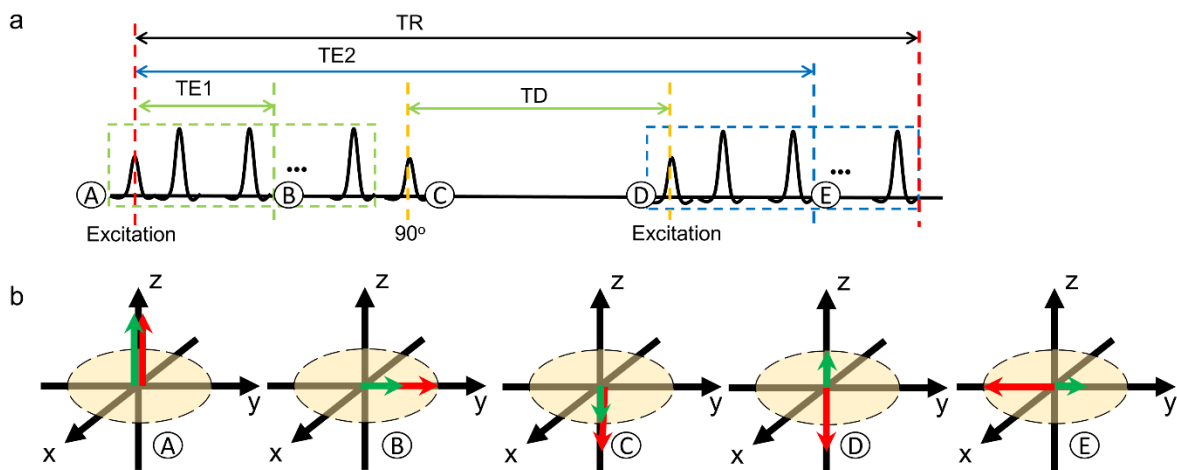


**Figure 2-10 Phase-based fluid attenuation**

(a) A schematic diagram of a phase-based fluid attenuation pulse sequence. A short time delay (TD) is inserted between the two acquisitions. (b) During the first acquisition, the spins of fluid and short-T1 tissue are in-phase. After the short time delay, the magnetization of the short-T1 tissue is directed along the positive z-axis, while the magnetization of fluid is directed along the negative z-axis because of its long T1. During the second acquisition, the spins of fluid and short-T1 tissue are out-of-phase.

The phase-based fluid attenuation method selectively suppresses the tissues that have both long T2 and T1. It also can simultaneously provide standard T2W and fluid suppressed

T2W images. However, the fluid suppression can be affected by the incoherent motions of fluid over the two data acquisitions.

### 2.4.3 Diffusion Weighted Imaging

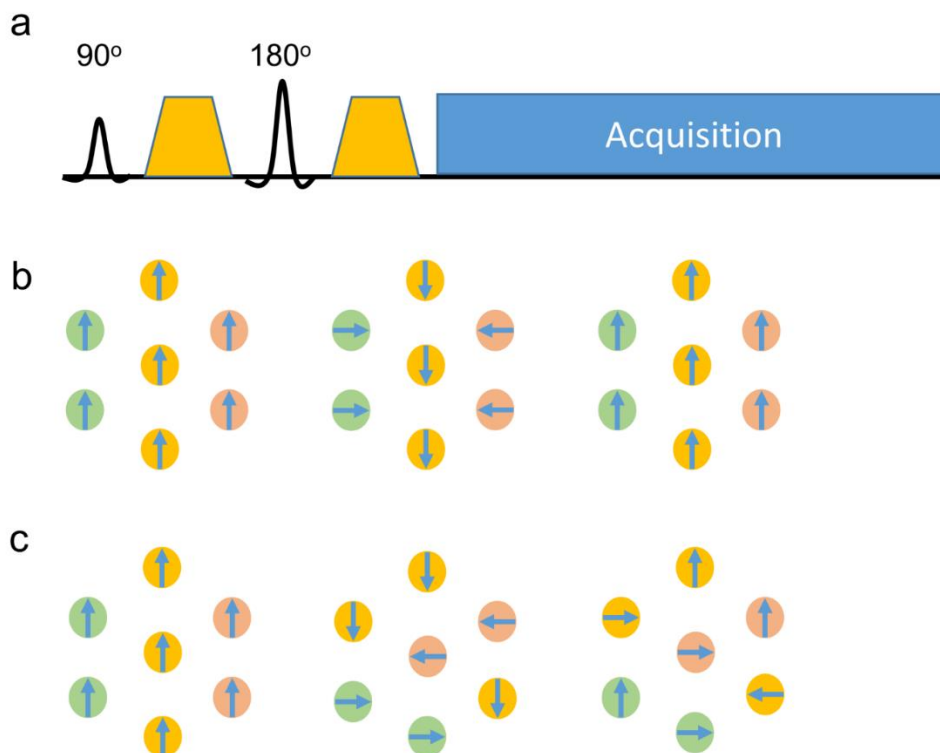


**Figure 2-11 Diffusion weighted imaging**

(a) A schematic diagram of a basic DWI pulse sequence. (b) Static spins will experience a diffusion dephasing gradient and gain phase shifts, which can be compensated by the 180° pulse and the diffusion rephasing gradient. (c) The diffusion rephasing gradient cannot rephase the moving spins due to the change of location during the diffusion preparation.

Diffusion Weighted Imaging (DWI) sequence generally contains two parts: diffusion preparation and acquisition, as shown in Figure 2-11a. In the diffusion preparation, (1) a 90°

pulse turns all the magnetization into transverse plane; (2) then the protons will experience the diffusion dephasing gradient and accumulate certain phase shifts; (3) the static protons (Figure 2-11b) will regain their original phase after the refocusing pulse and the diffusion rephasing gradient, while the moving protons will get an additional phase and will undergo signal loss. The signal loss can be modeled as

$$S = S_0 e^{-bD} \quad \text{Equation 2.5}$$

where  $D$  is the diffusion coefficient, and  $b$  is the b-value with a unit of  $\text{s}/\text{mm}^2$  and measures the degree of diffusion strength. b-value is dependent on the gyromagnetic ratio ( $\gamma$ ), gradient magnitude ( $G$ ), gradient duration ( $\delta$ ) and the interval between paired gradients ( $\Delta$ ),

$$b = \gamma^2 G^2 \delta^2 (\Delta - \delta/3) \quad \text{Equation 2.6}$$

Since  $\gamma$  is a constant for protons, the b-value can be increased by increasing the power of the gradients or/and increasing the interval between paired gradients. Fluid has a large diffusion coefficient due to a low viscosity coefficient, while the diffusion coefficients of other tissues and tumors are small because of high cell density. Therefore, fluid will experience more signal loss than other tissues at high b-values, and DWI can inherently suppress the signal from the fluid.

## **CHAPTER THREE**

### **Frequency Offset Corrected Inversion Pulse for $B_0$ and $B_1$ Insensitive Fat Suppression at 3T**

#### **3.1 OVERVIEW**

The majority of this work was accepted for publication in *Journal of Magnetic Resonance Imaging*. Portions of this work were presented at the 24<sup>th</sup> annual meeting of International Society for Magnetic Resonance in Medicine (ISMRM) in Singapore (May 2016).

#### **3.2 INTRODUCTION**

Fat suppression plays an important role in many clinical MRI applications due to its ability to enhance the conspicuity and contrast of targeted tissues or lesions (19,49). Several techniques have been developed to suppress fat. Generally, they can be divided into three major categories: spectrally selective fat suppression, chemical-shift imaging (Dixon) method, and non-selective short tau inversion recovery (STIR) (50). The spectrally selective fat suppression methods such as spectral pre-saturation with (adiabatic) inversion recovery (SPIR/SPAIR) have the advantage of higher signal to noise ratio (SNR), but are sensitive to  $B_0$  inhomogeneities (51). The Dixon methods can provide robust fat/water separation even in the presence of  $B_0$  inhomogeneities (52,53), however, they generally increase the total scan time or echo spacing due to the acquisition of multiple echoes (51,54). Alternatively, STIR provides uniform fat suppression, particularly with non-selective adiabatic inversion recovery (IR) pulses such as hyperbolic secant (HS), and are routinely used in the clinical practice (55). For example, STIR is routinely used to improve the visualization of the nerves in MR

neurography of brachial plexus. Compared to the spectrally selective fat suppression and Dixon methods, the fast/turbo spin echo (FSE/TSE) based T2-weighted STIR acquisitions suffer from reduced SNR, which can be mitigated using 3D acquisitions at higher field strengths, such as 3T (19). In addition to the improved SNR, 3D TSE-STIR also enhances the nerve visualization and lesion localization in brachial plexus imaging (49,56,57). However, the higher field strengths pose additional challenges to 3D TSE-STIR, including wider offset frequency between water and fat combined with larger  $B_0$  and  $B_1$  inhomogeneities, which reduce the reliability of fat suppression (56,58).

The crucial factors of an adiabatic IR pulse to achieve robust fat suppression in 3D TSE-STIR are a broader bandwidth for  $B_0$  insensitivity and a lower adiabatic threshold for  $B_1$  insensitivity, which are challenging to achieve simultaneously with the HS pulse (59,60). To improve the reliability of HS pulse, several alternatives including a derivative of the HS pulse, called a frequency offset corrected inversion (FOCI) pulse have been proposed (61,62). The FOCI pulse has been widely used in functional MR imaging including perfusion and spectroscopy to achieve sharper inversion profile combined with broader bandwidth (61,63), however, has not been evaluated for fat suppression. We hypothesize that, the broader bandwidth of the FOCI pulse enabled by the modulation of the HS pulse, provides increased robustness to  $B_0$  and  $B_1$  inhomogeneities simultaneously. Thus, the purpose of this work was to test and demonstrate the FOCI pulse as an efficient fat suppression STIR pulse with increased robustness to  $B_0$  and  $B_1$  inhomogeneities at 3T for brachial plexus imaging, compared to the commonly used HS pulse.

### 3.3 MATERIAL AND METHODS

The human studies were performed with institutional review board (IRB) approval and were HIPAA-compliant. All subjects provided written informed consent before participating in the study.

#### 3.3.1 Adiabatic Inversion Pulse

The amplitude,  $B_1^{HS}(t)$ , and frequency,  $\Delta\omega^{HS}(t)$ , modulation functions of the HS pulse (Figure 3-1a) are given by (64):

$$B_1^{HS}(t) = A_0 \operatorname{sech}(\beta t) \quad \text{Equation 3.1}$$

$$\Delta\omega^{HS}(t) = -\mu\beta \tanh(\beta t) \quad \text{Equation 3.2}$$

where  $A_0$  is the maximum amplitude of the  $B_1$  field,  $\beta$  is the modulation angular frequency,  $\mu$  is a dimensionless parameter.  $\beta$  and  $\mu$  determine the RF bandwidth ( $BW_{HS}$ ), and the adiabatic condition ( $A_0$ ) (60):

$$BW_{HS} = 2 \frac{\mu\beta}{\pi} \quad \text{Equation 3.3}$$

$$A_0 \gg \frac{\sqrt{\mu}\beta}{\gamma} \quad \text{Equation 3.4}$$

The FOCI pulse is a derivative of the HS pulse, modulated by a shaping function,  $C(t)$  (61):

$$B_1^{FOCI}(t) = C(t) \times A_0 \operatorname{sech}(\beta t) \quad \text{Equation 3.5}$$

$$\Delta\omega^{FOCI}(t) = -C(t) \times \mu\beta \tanh(\beta t) \quad \text{Equation 3.6}$$

Among various FOCI pulses, C-shaped FOCI (C-FOCI) (Figure 3-1a) has been widely used in perfusion MRI and MR spectroscopy due to its sharp inversion profile. The shaping function of C-FOCI is given by:

$$C(t) = \begin{cases} \cosh(\beta t) & \text{when } \cosh(\beta t) < C_{max} \\ C_{max} & \text{otherwise.} \end{cases} \quad \text{Equation 3.7}$$

where  $C_{max}$  is a dimensionless parameter, which defines the C-FOCI bandwidth ( $BW_{FOCI}$ ), as:

$$BW_{FOCI} = C_{max} \times BW_{HS} \quad \text{Equation 3.8}$$

Compared to the constant adiabatic threshold of the HS pulse (Equation 3.4), the adiabatic threshold of the C-FOCI pulse is a function of off-resonance frequency,  $\Omega$ , and can be derived as,  $A_{\Omega}$ , for isochromats at  $\Omega$  (Appendix A):

$$A_{\Omega} \gg \begin{cases} \frac{\sqrt{\mu}\beta}{\gamma} \sqrt{\cosh(\beta t_{\Omega})} & \text{when } |t_{\Omega}| < \text{arccosh}(C_{max})/\beta \\ \frac{\sqrt{\mu}\beta}{\sqrt{C_{max}} \times \gamma} & \text{otherwise.} \end{cases} \quad \text{Equation 3.9}$$

where  $t_{\Omega}$  is the time  $\Delta\omega^{FOCI}(t_{\Omega}) = \Omega$ .

The adiabatic threshold of the HS pulse (Equation 3.4) and the C-FOCI pulse (Equation 3.9), define the minimum  $B_1$  effective field required to achieve an acceptable inversion efficiency. The HS and C-FOCI pulses were implemented as preparation pulses in the 3D TSE-STIR sequence, by replacing the original inversion pulse, on a 3T MR scanner (Ingenia, software release R5.1.7, Philips Healthcare, Best, The Netherlands).

### 3.3.2 Simulations

Bloch equation simulations (60) were performed to compare the bandwidth and adiabatic threshold of the HS and C-FOCI pulses against the analytical solutions from Equations 3.4 and 3.9, respectively. Four inversion pulses were simulated: i) HS\_4\_6 ( $\tilde{\beta} = 4, \mu = 6$ ), similar to the vendor supplied HS pulse in 3D TSE-STIR (default HS pulse); ii) HS\_4\_18 ( $\tilde{\beta} = 4, \mu = 18$ ), to achieve three times the BW of the default HS pulse by increasing  $\mu$ ; iii) HS\_12\_6 ( $\tilde{\beta} = 12, \mu = 6$ ), to achieve three times the BW of the default HS pulse by increasing  $\tilde{\beta}$ ; and iv) C-FOCI ( $\tilde{\beta} = 4, \mu = 6$  and  $C_{\max} = 3$ ), to achieve three times the BW of the default HS pulse without increasing  $\tilde{\beta}$  or  $\mu$ .  $\tilde{\beta}$  was defined as  $\beta \times T_p/2$ , where  $T_p$  was the duration of the pulse, which was set to 18.3 ms. All simulations were performed in Matlab R2016b (The MathWorks, Natick, MA, USA).

### 3.3.3 Phantom Study

To evaluate the  $B_1$  sensitivity, the C-FOCI pulse was compared against the HS\_4\_18 pulse, which has the same bandwidth as C-FOCI pulse and lower adiabatic threshold than the HS\_12\_6 pulse, using a phantom consisting of a gadolinium-doped agarose gel ( $T_1/T_2 = 1680/64$  ms) and a canola oil bottle ( $T_1/T_2 = 330/49$  ms) with a 3D TSE-STIR sequence. Specifically, the maximum  $B_1$  of the IR pulse was varied at 100% (13.5  $\mu\text{T}$ ), 75% (10.1  $\mu\text{T}$ ), 50% (6.7  $\mu\text{T}$ ) and 25% (3.4  $\mu\text{T}$ ), with 13.5  $\mu\text{T}$  being the maximum RF strength of the body transmit coil. The other acquisition parameters included: FOV =  $200 \times 200 \times 20$  mm<sup>3</sup>; acquired resolution =  $1.4 \times 1.4 \times 1.4$  mm<sup>3</sup>; inversion time = 240 ms; turbo factor = 100; echo spacing = 2.7 ms; TR = 5000 ms.

After the inversion pulse, the longitudinal magnetization at the predefined inversion time (TI) can be expressed as,

$$M(TI) = fM_0e^{-\frac{TI}{T_1}} + M_0 \left(1 - e^{-\frac{TI}{T_1}}\right) \quad \text{Equation 3.10}$$

where  $f$  is the inversion efficiency, and  $M_0$  is the longitudinal magnetization at thermal equilibrium state.

The inversion efficiency,  $f$ , which ranges from +1 (no inversion) to -1 (full inversion) can be calculated as,

$$f = \frac{M(TI)}{M_0e^{-\frac{TI}{T_1}}} - \left(\frac{1}{e^{-\frac{TI}{T_1}}} - 1\right) \quad \text{Equation 3.11}$$

Given,

$$M_{norm} = \frac{M(TI)}{M_0} \quad \text{Equation 3.12}$$

$M_0$  was measured from a reference image that was acquired with the same parameters as  $M(TI)$  but without the inversion pulse. Finally, the inversion efficiency can be calculated as

$$f = 1 + \frac{M_{norm} - 1}{e^{-TI/T_1}} \quad \text{Equation 3.13}$$

### 3.3.4 In Vivo Study

The C-FOCI pulse was evaluated *in-vivo* in 3D T2-weighted MR neurography of the brachial plexus at 3T, a challenging anatomy to achieve uniform fat suppression due to large  $B_0$  and  $B_1$  inhomogeneities (57). Similar to the phantom study, the C-FOCI pulse was compared against the HS\_4\_18 pulse in a healthy volunteer using 3D TSE-STIR sequence at varying maximum  $B_1$  strengths. A  $B_1$  map was also acquired in this volunteer using a dual

flip angle 2D turbo field echo (TFE) (65) with the following parameters: FOV =  $300 \times 400$  mm<sup>2</sup>; acquired resolution =  $4 \times 4$  mm<sup>2</sup>; TE = 10 ms; TR = 5000 ms; flip angles = 60° and 120°.

Subsequently, 3D TSE-STIR with a C-FOCI pulse was compared against the commercially available 3D TSE-STIR with a HS pulse in the brachial plexus of three healthy volunteers and five patients (age range: 37 – 61 years). The images were acquired in the coronal plane with the following parameters: FOV =  $300 \times 400 \times 124$  mm<sup>3</sup>; acquired resolution =  $1.4 \times 1.4 \times 1.4$  mm<sup>3</sup>; inversion time = 240 ms; turbo factor = 130; TR = 2550 ms; TE<sub>effective</sub> = 187 ms; SENSE parallel imaging factor of 2 along the right-left phase-encoding direction and 1.4 along the anterior-posterior slice-encoding direction, and a total acquisition time of 5:15 minutes.

### **3.3.5 Image Evaluation**

The *in-vivo* brachial plexus images were qualitatively evaluated by two fellowship-trained musculoskeletal radiologists (Dr. Chhabra, with 19 years of experience; Dr. Pezeshk with 4 years of experience) independently using a four-point grading scale for fat suppression (0 – non-diagnostic and image degraded; 1 – moderate and non-uniform but some diagnostic information; 2 – good and no diagnostic information compromised; 3 – excellent), shading artifacts (0 – non-diagnostic and image degraded; 1 – obvious shading artifact but some diagnostic information; 2 – minor shading artifact and no diagnostic information compromised; 3 – no shading artifact) and visualization of the nerves (0 – poor visualization and non-diagnostic; 1 – moderate visualization but some diagnostic information; 2 – good visualization and minor diagnostic information compromised; 3 – excellent visualization).

The scores from both reviewers were averaged and statistical analysis of these qualitative scores was performed with a Wilcoxon signed-rank test. The inter-observer agreement between the two radiologists was assessed by kappa ( $\kappa$ ) statistics and categorized as, poor ( $<0.20$ ), fair ( $0.20 - 0.39$ ), moderate ( $0.40 - 0.59$ ), good ( $0.60 - 0.79$ ), or excellent ( $>0.80$ ). GraphPad Prism 7 (GraphPad, San Diego, CA) was used to perform the statistical analysis with  $P < 0.05$  considered statistically significant.

### 3.4 RESULTS

#### 3.4.1 Simulations

The bandwidth of the default HS pulse (Figure 3-1c) could be broadened (to reduce  $B_0$  sensitivity) by either increasing  $\mu$  (Figure 3-1d) or  $\beta$  (Figure 3-1e), at the expense of increased adiabatic threshold and hence  $B_1$  sensitivity, as predicted by Equation 4. However, the bandwidth of the C-FOCI pulse with the same parameters of  $\beta$  and  $\mu$  as the default HS pulse could be increased by a factor of  $C_{max}$  without increasing the adiabatic threshold at the on-resonance frequency (Figure 3-1f). A  $C_{max}$  of 3 increased the bandwidth of the default HS inversion pulse by threefold (from 833 Hz to 2.5 kHz), with minimal increase in the adiabatic threshold at the fat frequency (from 4  $\mu$ T to 5  $\mu$ T). This provided a good compromise to achieve robustness to both  $B_0$  and  $B_1$  inhomogeneities. The adiabatic threshold of the C-FOCI pulse calculated using Equation 9 matched exactly the Bloch equation simulation results (Figure 3-1f), showing the accuracy of the derived  $A_\Omega$ . The adiabatic thresholds of the HS pulse with increased  $\mu$  (HS\_4\_18) was lower than that with increased  $\beta$  (HS\_12\_6) (Figure 3-1b). Compared to the HS\_4\_18 pulse, the adiabatic threshold of the C-FOCI pulse

with the same bandwidth was 58% and 32% lower at 0 Hz (water) and -440 Hz (main fat peak at 3T) respectively.

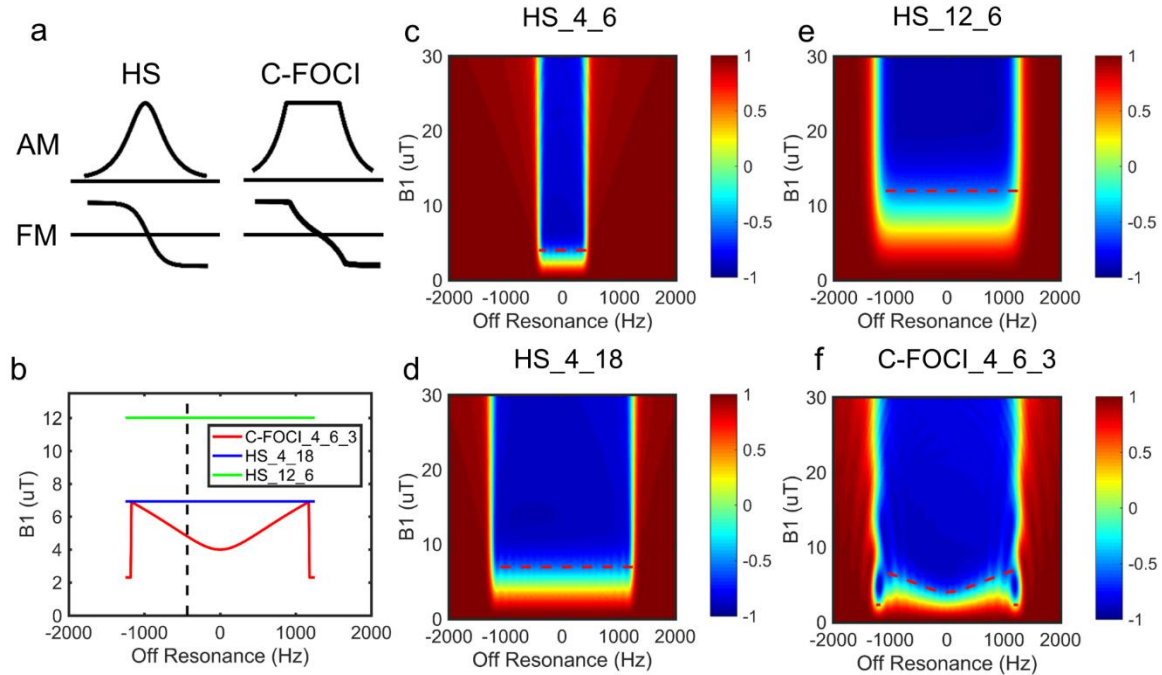


**Figure 3-1 HS and C-FOCI pulse**

(a) HS and C-FOCI RF pulse shapes including amplitude modulation (AM) and frequency modulation (FM). (c) HS ( $\beta=4, \mu=6$ ); (d) HS ( $\beta=4, \mu=18$ ); (e) HS ( $\beta=12, \mu=6$ ) and (f) C-FOCI ( $\beta=4, \mu=6$  and  $C_{\max}=3$ ) pulses were simulated with Bloch equation. The red dashed lines in (a-d) show analytically calculated adiabatic threshold at different off-resonance frequencies. (b) Compares the adiabatic thresholds of C-FOCI (red), HS ( $\beta=4, \mu=18$ , blue) and HS ( $\beta=12, \mu=6$ , green) pulses with same bandwidth, showing lower adiabatic threshold for C-FOCI pulse at all resonance frequencies. The vertical black dashed line is shown at -440 Hz, the main fat peak frequency at 3T.

### 3.4.2 Phantom Results

The phantom study demonstrating increased robustness of C-FOCI pulse to  $B_1$  and  $B_0$  inhomogeneities compared to the HS pulse with the same bandwidth (HS\_4\_18) is shown in

Figure 3-2. The inversion efficiency calculated from the signal intensities using Equation 3.13 matched the theoretical expectations at varying  $B_1$  strengths for both water and fat (Figure 3-3). The minimum  $B_1$  strengths required by the HS and C-FOCI pulses to achieve 95% of the maximum inversion efficiency for fat were 10  $\mu\text{T}$  and 6.5  $\mu\text{T}$  respectively, validating increased robustness of the C-FOCI pulse to  $B_1$  inhomogeneities.

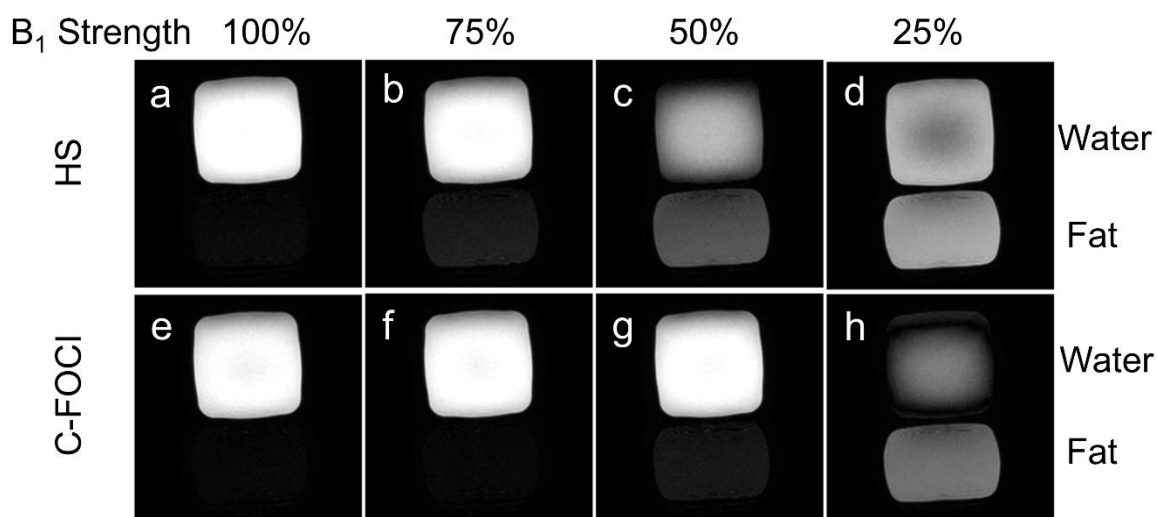


**Figure 3-2 Fat suppression with 3D-TSE-STIR using HS pulse and C-FOCI pulse**

Phantom images comparing the fat suppression with 3D-TSE-STIR sequence using HS\_4\_18 pulse (top row, a-d) and C-FOCI pulse (bottom row, e-h) against varying  $B_1$  strengths of the inversion pulses. Note the uniform fat suppression achieved with C-FOCI pulse even at the 50%  $B_1$  strength (g), while the HS pulse has some residual fat signal at 75%  $B_1$  strength (b). All images are shown at the same window and level to emphasize the signal variations.

### 3.4.3 In-Vivo Results

Figure 3-4 demonstrates similar behavior of the C-FOCI pulse in the evaluation of brachial plexus, an anatomical region known to have increased  $B_0$  and  $B_1$  inhomogeneities. Similar to phantom experiments, the fat suppression failed at 50%  $B_1$  strength with the HS

pulse (Figure 3-4c), while the C-FOCI pulse still achieved uniform fat suppression (Figure 3-4g). The increased  $B_1$  inhomogeneity (Figure 3-4i), however, leads to shading artifacts observed on the right shoulder of the volunteer, which are evident only at 50%  $B_1$  strength with the C-FOCI pulse (Figure 3-4g, arrow) compared to 75%  $B_1$  strength with the HS pulse (Figure 3-4b, arrow).

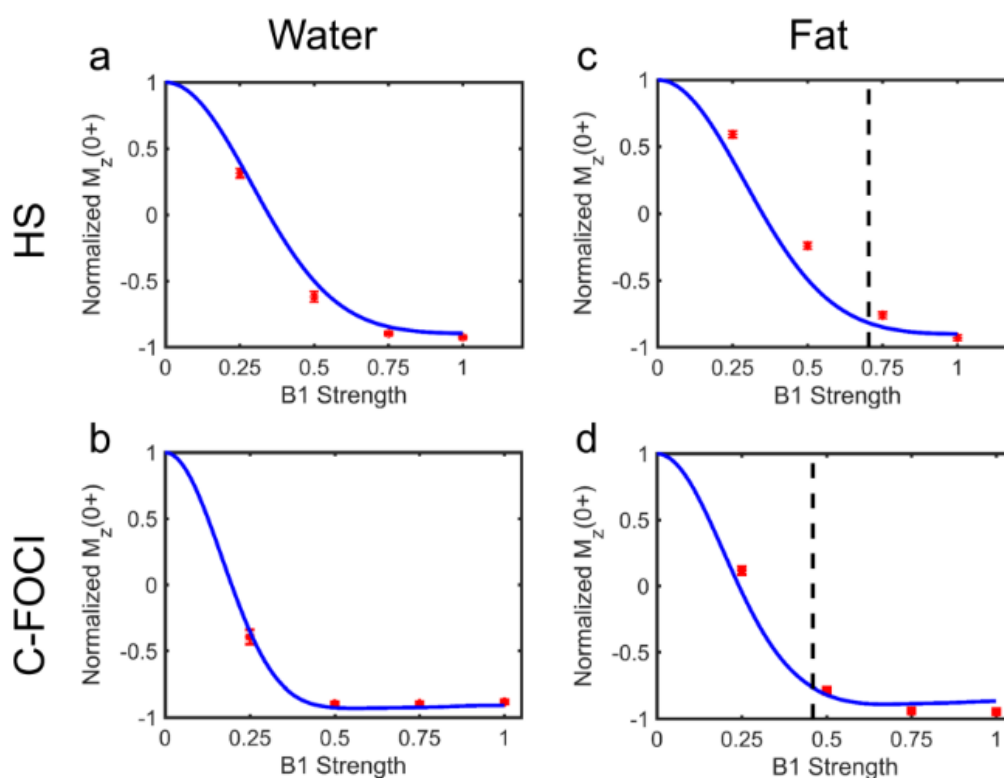


**Figure 3-3 Inversion efficiencies of HS pulse and C-FOCI pulse**

Inversion efficiencies of HS\_4\_18 pulse (top row; a, c) and C-FOCI pulse (bottom row; b, d) for water (left column; a, b) and fat (right column; c, d) signals against the normalized  $B_1$  strength. The blue lines are the normalized signals from the Bloch equation simulation results (fig. 1), and the red dots are the normalized signals from the experimental results (Figure 3-2). The x-axis represents the normalized  $B_1$  strength to the maximum  $B_1$  of the body transmit coil (13.5  $\mu$ T). The vertical dashed lines represent the minimum  $B_1$  strengths required to achieve 95% of the maximum inversion efficiency for fat.

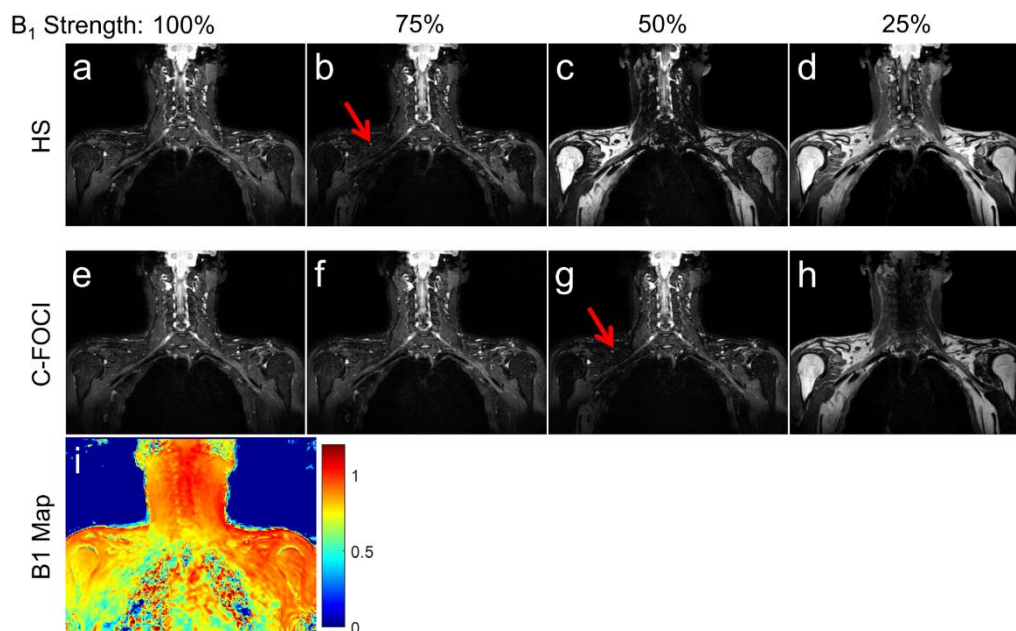


**Figure 3-4 Healthy volunteer image acquired using 3D TSE STIR with HS pulse and C-FOCI pulse**

Targeted maximum intensity projection (MIP) images of brachial plexus of a 37-years old healthy volunteer acquired using 3D TSE-STIR against varying B<sub>1</sub> strengths of the IR pulse. Top row (a-d) images used the HS pulse ( $\beta = 4$ ,  $\mu = 18$ ) with  $A_0 = 100\%$ , 75%, 50% and 25% of the maximum B<sub>1</sub> of the body transmit coil (13.5 uT). Bottom row (e-h) images used the C-FOCI pulse ( $\beta = 4$ ,  $\mu = 6$ ,  $C_{\max} = 3$ ) with the same B<sub>1</sub> strengths as HS pulse. i) B<sub>1</sub> map acquired with dual-flip angle TFE. The arrows in (b) and (g) show the shading artifacts due to the reduced B<sub>1</sub> on the right side of the shoulder, consistent with the B<sub>1</sub> map (i).

Compared to the commercially available 3D TSE-STIR sequence with the HS pulse, the C-FOCI pulse achieved uniform fat suppression without any shading artifacts in patients (Figure 3-5). The uniform fat suppression due to the increased robustness to B<sub>0</sub> inhomogeneities throughout the volume improved visualization of the nerves in the brachial plexus with the C-FOCI pulse across all volunteers and patients (Figure 3-6). There was a

good agreement for fat suppression ( $\kappa = 0.75$ ) and shading artifact ( $\kappa = 0.61$ ) between the two radiologists. The agreement for nerve visualization was moderate ( $\kappa = 0.52$ ), however, the major differences were for images acquired with HS pulse. All 3D TSE-STIR images acquired with C-FOCI pulse were rated either 2 (good visualization and minor diagnostic information compromised) or 3 (excellent visualization). Fat suppression ( $3 \pm 0$  vs.  $1.5 \pm 1.1$ ;  $P < 0.05$ ) and nerve visualization ( $2.9 \pm 0.4$  vs.  $2.1 \pm 0.9$ ;  $P < 0.05$ ) were significantly better with the C-FOCI pulse compared to the HS pulse. 3D TSE-STIR with the C-FOCI pulse also showed significantly fewer shading artifacts compared to 3D TSE-STIR with the HS pulse ( $2.9 \pm 0$  vs.  $1.8 \pm 0.5$ ;  $P < 0.01$ ).

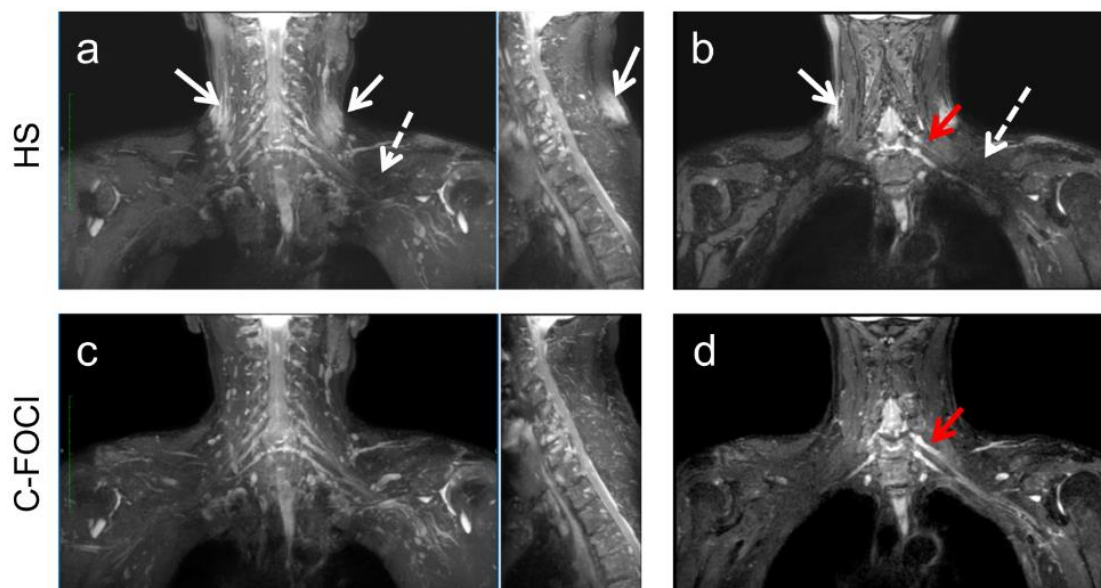


**Figure 3-5 3D T2-weighted MR neurography of brachial plexus of a patient**

3D T2-weighted MR neurography of brachial plexus of a 61-years old patient comparing 3D TSE-STIR with C-FOCI pulse (bottom row; c, d) with commercially available 3D TSE-STIR with HS pulse (top row; a, b). a) Targeted MIP images in the acquired coronal plane and the reformatted sagittal plane show incomplete fat suppression (arrows) and shading artifacts (dashed arrow) with HS pulse. b) A single slice of the image shown in (a). Corresponding

targeted MIP images (c) and a single slice (d) show uniform fat suppression without any shading artifacts with C-FOCI pulse. Mild edema within the left C8 nerve extending into the inferior trunk (red arrows) is more conspicuous on the FOCI image (d) compared to the HS image (b).

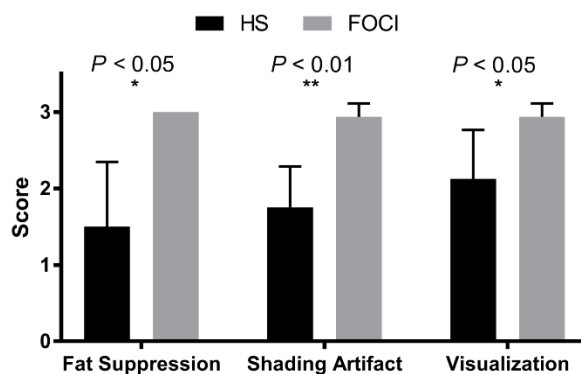


**Figure 3-6 Qualitative assessments of the brachial plexus images acquired using 3D TSE STIR with HS pulse and C-FOCI pulse**

Qualitative assessments reveal the superior performance of the C-FOCI pulse compared with the commercial HS pulse in three healthy volunteers and five patients acquired using 3D TSE-STIR. Fat suppression ( $P < 0.05$ ) and nerve visualization ( $P < 0.05$ ) were significantly better with C-FOCI pulse and also showed significantly fewer shading artifacts ( $P < 0.01$ ) compared with HS pulse.

### 3.5 DISCUSSION

In STIR sequences, non-selective adiabatic HS pulses are commonly used to achieve robust fat suppression with increased robustness to  $B_1$  inhomogeneities. At higher magnetic field strengths, e.g. 3T, the resonance frequency difference between water and fat increases, and thus the bandwidth of the HS pulse needs to be increased correspondingly to achieve non-selective inversion across a broad frequency range. However, the adiabatic threshold of

the HS pulse is directly proportional to the bandwidth and hence will also be elevated, resulting in increased sensitivity to  $B_1$  field variations (66). In this work, we have shown that the adiabatic C-FOCI pulse can achieve larger bandwidth without substantially increasing the adiabatic threshold and provide uniform fat suppression in 3D TSE-STIR with increased robustness to  $B_0$  and  $B_1$  inhomogeneities, as shown in the entire volume of brachial plexus imaging.

Several groups have used chemical-shift imaging (i.e. Dixon) based techniques to achieve robust fat suppression in brachial plexus (52,53). However, these techniques either sacrifice the spatial resolution or increase the scan times (54). Compared to Dixon based techniques, 3D TSE-STIR with C-FOCI can achieve robust fat suppression, without increasing the scan times or reducing the spatial resolution. Furthermore, the increased robustness to  $B_0$  inhomogeneities due to the larger bandwidth of the C-FOCI pulse can also achieve efficient fat suppression in the off-center imaging (e.g. shoulders).

Compared to the HS pulse, the adiabatic factor of the C-FOCI pulse has the additional dependency on resonance frequency, as observed with the Bloch equation simulations. To better understand the dependency of the adiabatic factor on RF pulse parameters and the performance of the C-FOCI pulse, an analytical expression of the adiabatic threshold against off-resonance frequency was derived in this work. It is noted that the derived adiabatic factor of the C-FOCI pulse will be the same as that of the HS pulse, when the modulation function,  $C_{\max}$ , has a constant value of 1. The derived analytical expression provides opportunities for flexible on-line optimization of various FOCI pulses (61), including C-FOCI pulse for different purposes.

The incomplete fat suppression and the shading artifacts observed in 3D TSE-STIR using the HS pulse were primarily caused by the reduced inversion efficiency, which makes the TI closer to the null point of the water signal instead of the fat signal. From the simulation results, it is evident that the inversion efficiency decreases around the edges of the profile and below the adiabatic thresholds. For the *in-vivo* study, this resulted in incomplete fat suppression and shading artifacts in the neck and shoulder areas, where the  $B_0$  and  $B_1$  field variations are often larger (67). Increasing the bandwidth of the C-FOCI pulse while maintaining the same adiabatic factor as the HS pulse at on-resonance frequency and slightly elevated adiabatic factor at fat frequency achieved successful inversion of both water and fat spins across the entire imaging volume providing uniform fat suppression and minimal shading artifacts.

The C-FOCI pulse was evaluated with 3D TSE-STIR sequence in this work; however, it can also be used with 2D TSE-STIR sequence. At 3T, this may not be necessary, since the  $B_0$  and  $B_1$  variations within a single slice of a multi-slice 2D TSE-STIR are minimal and the adiabatic HS pulse often provides uniform fat suppression with minimal shading artifacts (51). At higher field strengths such as 7T,  $B_0$  and  $B_1$  variations within a single slice can be substantial (68) and the C-FOCI pulse may provide uniform fat suppression in such instances. Compared to the HS pulse, the C-FOCI pulse increases the specific absorption rate (SAR) (69). However, the increase in SAR is not a problem in 3D TSE-STIR due to the use of a relatively long TR. For example, the SAR increased from 1.4 W/Kg with the HS pulse to 1.7 W/Kg with the C-FOCI pulse in our *in vivo* imaging protocol.

This study has several limitations. First, our work only focused on the C-FOCI pulse and its comparison with the most commonly used adiabatic HS pulse. There are several other inversion pulses (70,71), including variations of the FOCI pulse such as T-FOCI (61) that can also be potentially used for fat suppression. Nevertheless, the analytical expression derived for the C-FOCI pulse can be easily modified for other FOCI pulses and facilitates such comparisons. Second, our work included evaluation in a single anatomical location of brachial plexus imaging in very few patients and needs further evaluation in other anatomies and larger clinical populations.

In conclusion, we have demonstrated the FOCI pulse as an efficient fat suppression STIR pulse with increased robustness to  $B_0$  and  $B_1$  inhomogeneities at 3T and derived an analytical expression for the adiabatic factor of the FOCI pulse. Compared to the commonly used adiabatic HS pulse, the FOCI pulse achieves broader bandwidth with minimal increase in the adiabatic threshold enabling uniform fat suppression with minimal shading artifacts in challenging anatomies such as MR neurography of brachial plexus.

## **CHAPTER FOUR**

### **MR Neurography of Brachial Plexus at 3T with Robust Fat and Blood Suppression**

#### **4.1 OVERVIEW**

The majority of this work was published in *Radiology* 283(2): 538-546 (2017). Portions of this work were presented at the 23<sup>rd</sup> and 24<sup>th</sup> annual meeting of International Society for Magnetic Resonance in Medicine (ISMRM) in Toronto (May 2015) and Singapore (May 2016) respectively.

#### **4.2 INTRODUCTION**

The brachial plexus, which includes the network of nerves running from the cervical spine to the upper limb, can be involved in a variety of pathologies resulting in upper limb functional impairment. Magnetic Resonance Neurography (MRN), performed primarily by using fat-suppressed T2-weighted imaging, has become the preferred method to evaluate the brachial plexus because of its excellent soft tissue contrast combined with high resolution and multiplanar capabilities (72,73). Fat suppression is achieved primarily with either non-selective short tau inversion recovery (STIR) (74) or chemically-selective spectral adiabatic inversion recovery (SPAIR) (75). Both of these techniques, however, are sensitive to  $B_1$  and  $B_0$  inhomogeneities that are common in brachial plexus imaging, particularly at 3T, thereby leading to poor fat suppression and low signal to noise ratio (SNR). In the past decade, several groups have combined chemical-shift acquisitions (i.e. modified Dixon or mDixon) with turbo spin echo (TSE) techniques for high quality 2D T2W images of the brachial plexus with uniform fat suppression (53,76).

The brachial plexus has complex ramifications, and hence 2D T2W images in more than one orientation are needed for multiplanar visualization. Significant enhancements in the area of variable refocusing flip angles combined with long echo trains and parallel imaging have enabled volumetric T2W images using 3D TSE in clinically feasible scan times (77,78). However, 3D TSE combined with mDixon requires multiple echoes for fat/water separation, making the acquisition times prohibitively long to maintain patient compliance (79,80). An additional concern with MRN of the brachial plexus is the presence of blood vessels in close proximity that often confounds the nerve visualization. TSE acquisitions are sensitive to large motion and suppress the fast flowing blood signal in the major arteries, but the slower venous flow signal remains unsuppressed.

Therefore, it is necessary to develop a sequence which addresses two problems: (a) To reduce the acquisition time of 3D TSE-mDixon by using a multi-echo approach to acquire both in-phase (IP) and out-of-phase (OP) echoes required for fat/water separation in the same repetition and (b) To suppress the blood vessel signal in the slow flowing veins using low refocusing flip angle 3D TSE. Thus, the purpose of our study was to develop and evaluate MR neurography of brachial plexus with robust fat and blood suppression for increased conspicuity of nerves at 3T in clinically feasible acquisition times.

## **4.3 MATERIALS AND METHODS**

### **4.3.1 Subjects**

Our prospective human study was HIPAA-compliant and approved by the institutional review board. All subjects provided written informed consent before participating in the study.

The sequence was initially optimized on 3 healthy volunteers (1 man, age: 26 years; 2 women, age: 37 years (mean), 33-41 years (range); overall age: 33.3 years (mean), 26–41 years (range)). Subsequently, our optimized TSE-mDixon sequence was compared against clinical standard 3D TSE-STIR in 5 healthy volunteers (3 men, age: 41.3 years (mean), 40-42 years (range); 2 women, age: 45.5 years (mean), 40-51 years (range); overall age: 43 years (mean), 40-51 years (range)) and 10 patients (3 men, age: 65.3 years (mean), 61-70 years (range); 7 women, age: 50.9 years (mean), 32-64 years (range); overall age: 55.2 years (mean), 32-70 years (range)). There was no statistically significant difference in age between men and women subjects ( $p=0.64$  with Welch's t-test). Patients who were referred for the MRI evaluation of brachial plexopathy between June 2015 and June 2016 at our institution and signed a written informed consent to undergo additional MRI sequences were consecutively enrolled in our study. Patients who were contraindicated for MRI (e.g. MRI unsafe indwelling devices), pregnancy, unable to complete the MRI examination (e.g. claustrophobia) or did not provide the written informed consent were excluded.

#### **4.3.2 Multi-echo 3D TSE-mDixon**

In a two-point TSE-mDixon acquisition, the OP image is acquired by shifting the readout gradient by  $\delta t$  with respect to the spin (or Hahn) echo that generates the IP image (e.g. 1.1 ms at 3T) (81). Due to low readout bandwidths of 2D acquisitions, majority of 2D TSE-mDixon sequences acquire the IP and OP images in separate repetition times (TRs) (Figure 4-1a, multi-acquisition). When extended to 3D TSE, this doubles the total acquisition time and becomes prohibitively long (e.g. longer than 10 minutes).

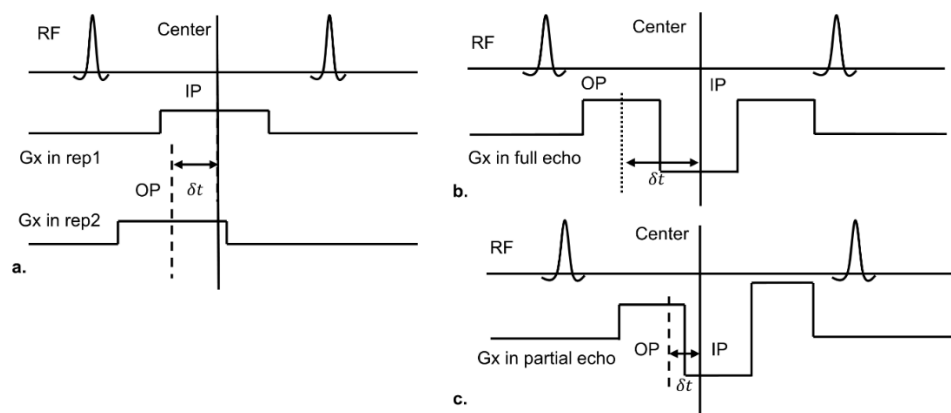


**Figure 4-1 Schematic of the multi-acquisition and multi-echo TSE-mDixon**

Schematic of the TSE-mDixon showing a pair of refocusing flip angles (RF) and the corresponding readout gradients (Gx), acquiring in-phase (IP) and out-of-phase (OP) echoes in two separate repetitions (rep1 and rep2) in a multi-acquisition TSE-mDixon (a). The current implementation acquires both IP and OP echoes with a bipolar acquisition in the same repetition, either using full echo (b) or partial echo (c), in multi-echo TSE-mDixon.  $\delta t$  is the time difference between the acquisitions of OP and IP echoes (e.g. 1.1 ms at 3T).

To reduce the total scan time, a bipolar multi-echo acquisition was implemented to acquire both IP and OP echoes in the same TR (Figure 4-1b), as previously reported at 1.5T (82). The extension of this approach to 3T, however, was challenging as the  $\delta t$  between the IP and OP echoes needed to be  $\sim 1.1$  ms for robust fat/water separation. To address this, partial echoes (Figure 4-1c) were used to maintain the IP and OP interval followed by homodyne reconstruction with phase preservation (see below) to successfully reconstruct the fat and water separated images.

### 4.3.3 Homodyne Reconstruction with Phase Preservation

The standard homodyne reconstruction, which only provides real images (83), was modified with phase preservation for proper fat/water separation (84). First, a low-pass (LP)

filtered image using the central symmetrically sampled data ( $LP = M_{LP}e^{-i\phi_{LP}}$ ) and a high-pass (HP) filtered image using the entire sampled data ( $HP = M_{HP}e^{-i\phi_{HP}}$ ) were reconstructed separately. Next, the standard homodyne image (HD) was reconstructed by taking the real part of the phase-corrected high-pass filtered image ( $HD = Re\{M_{HP}e^{-i\phi_{HP}}e^{+i\phi_{LP}}\}$ ). Subsequently, the phase information from the low-pass filtered image is concatenated back to the homodyne image to reconstruct the final complex image (i.e.) ( $HD_{complex} = HD e^{-i\phi_{LP}}$ ). This procedure was repeated separately for the IP and the OP images, before processing them through the mDixon reconstruction for fat/water separation (85).

#### 4.3.4 MRI Experiments

All of the imaging experiments were performed on a 3T Ingenia scanner (Philips Healthcare, Best, The Netherlands). A phantom study consisting of a gadolinium doped agarose gel and an oil bottle was performed to evaluate the fat/water separation using the multi-echo TSE-mDixon with partial echo acquisition and homodyne reconstruction. For comparison, high-resolution images were also acquired with multi-acquisition TSE-mDixon using full echoes in separate TRs, but at double the scan time. A flow phantom consisting of a static object surrounded by two tubes with moving water in opposite direction at 3 cm/s was imaged using 3D TSE with different minimum flip angles ( $\alpha_{min}$ ) to evaluate the sensitivity of low refocusing flip angles to motion (78). The signal intensities of the static phantom and the flowing water were measured using region of interest (ROI) to evaluate relative signal suppression.

**Table 4-1 Parameters of the MRN pulse sequences used for the in vivo evaluation of brachial plexus**

Parameter	Sequences	
	Multi-echo 3D TSE- mDixon	3D TSE STIR/SPAIR
Flip Angles ( $\alpha_{\min}$ - $\alpha_{\text{center}}$ - $\alpha_{\max}$ )	20-100-120	20-100-120
FOV (mm <sup>3</sup> )	320×420×124	320×420×124
Acquired Resolution (mm <sup>3</sup> )	1.4×1.4×1.4	1.4×1.4×1.4
Reconstructed Resolution (mm <sup>3</sup> )	0.7×0.7×0.7	0.7×0.7×0.7
TE <sub>effective</sub> / TE <sub>equivalent</sub> (ms)	294 /107	234/98
Echo Spacing (ms)	5.3	2.8
TR (ms)	2000	3000
TI (ms)	-	240 ms
SENSE Acceleration Factor	Phase: 2.4 Slice : 1	Phase: 2 Slice : 1.4
Receiver Bandwidth (Hz/Pixel)	2108	2108
Partial Echo Factor	0.8	1
Echo Train Length/Turbo Factor	100	160
Scan time (min)	6:00	6:00

All of the human imaging was performed using the embedded posterior coil, base of the head coil and an anterior torso coil for signal reception with the dual-transmit body coil for signal transmission. Brachial plexus images were acquired using the multi-echo 3D TSE-mDixon in the coronal plane using parameters listed in Table 1. A  $\delta t$  of 1.05 ms between the IP and OP echoes and a partial echo factor of 0.8 was used with a total acquisition time of 6:00 minutes. The source images were first reconstructed using the homodyne processing

with phase preservation implemented on the scanner, followed by mDixon processing for fat/water separation. All subjects were also scanned using the standard of care 3D TSE STIR for comparison. Due to the prohibitively long scan time of 12:00 minutes, multi-acquisition 3D TSE-mDixon was not performed *in vivo*. Additionally, 3D TSE SPAIR was performed on healthy volunteers, but not on subsequent patients due to incomplete fat suppression observed in the preliminary studies. The acquisition parameters used for 3D TSE STIR and SPAIR are also listed in Table 4-1.

#### 4.3.5 Image Evaluation

**Table 4-2 Qualitative Assessment**

Feature/Score	0	1	2
Fat Suppression	Poor and non-diagnostic	Moderate and non-uniform but diagnostic	Excellent and uniform
Arterial Suppression	Unsuppressed and non-diagnostic	Moderately suppressed but diagnostic	Excellent suppression
Venous Suppression	Unsuppressed and non-diagnostic	Moderately suppressed but diagnostic	Excellent suppression
Nerve Visualization	Poor visualization and non-diagnostic	Moderate visualization but diagnostic	Excellent visualization and diagnostic

The source images and the targeted maximum intensity projection (MIP) images were qualitatively evaluated by a musculoskeletal radiologist (CA) with 19 years of experience using a three-point grading scale (Table 4-2). The qualitative scores were statistically analyzed using the non-parametric Wilcoxon signed-rank test. Additionally, quantitative apparent SNR (aSNR), defined as the ratio of the signal mean to its standard deviation, was

measured on the dorsal nerve root ganglion and C6 nerve and compared using the non-parametric Friedman two-way ANOVA with fat suppression method and nerve type as factors. GraphPad Prism 6 (GraphPad, San Diego, CA) and SAS 9.4 (SAS Institute, Cary, NC) were used to perform the statistical analysis with  $p < 0.05$  considered statistically significant. Our sample size,  $N=15$ , was chosen to provide at least 85% power to measure the statistically significant difference.

#### 4.4 RESULTS

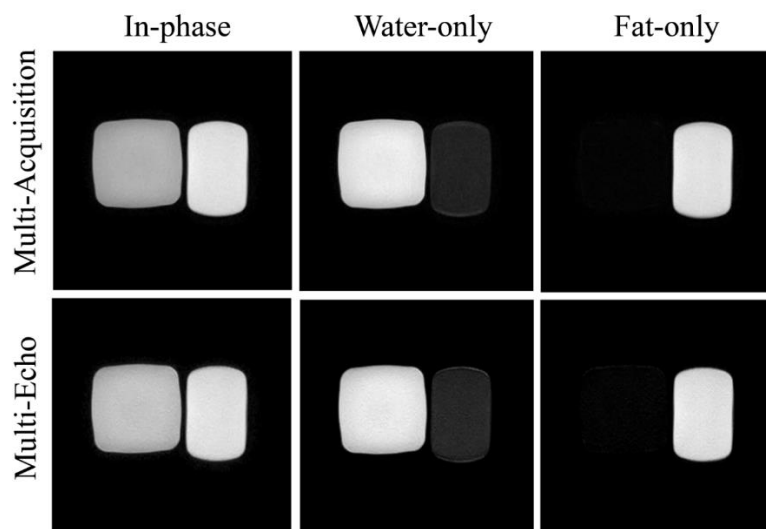


**Figure 4-2 Phantom images acquired using multi-acquisition and multi-echo 2D TSE-mDixon**

In-phase (left), water-only (middle) and fat-only (right) images acquired using multi-acquisition 2D TSE-mDixon (top row) and multi-echo 2D TSE-mDixon (bottom row) showing qualitatively equivalent fat/water separation. Multi-echo TSE-mDixon images were acquired using partial echo factor of 0.8, followed by homodyne reconstruction with phase preservation enabling  $1 \times 1 \text{ mm}^2$  in-plane spatial resolution matching multi-acquisition TSE-mDixon. Multi-echo 2D TSE-mDixon was acquired in 1:30 min, which was half the scan time of the multi-acquisition 2D TSE-mDixon (3:00 min).

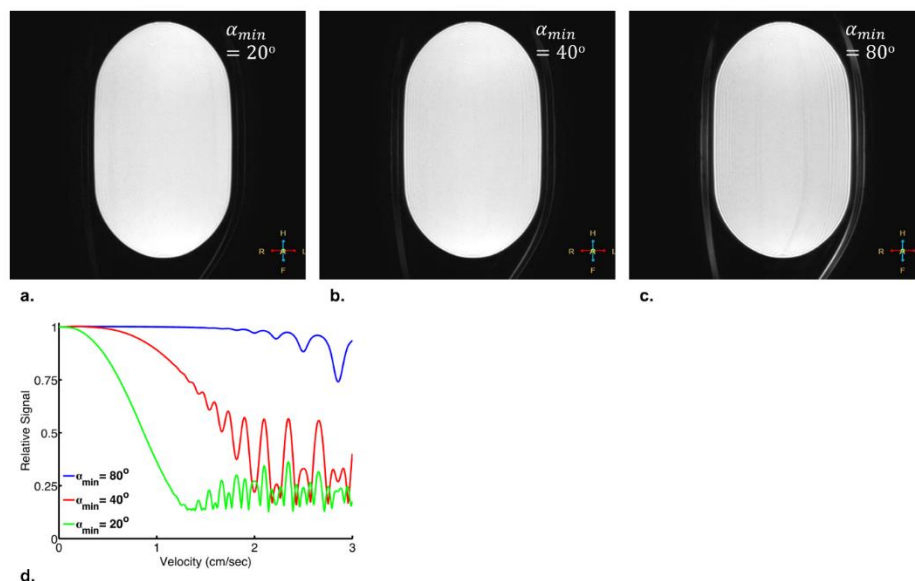


**Figure 4-3 TSE signal behavior with variable refocusing flip angles**

TSE signal behavior with variable refocusing flip angles showing increased sensitivity of lower refocusing flip angles to motion. The signal in the static phantom at the center was similar across all images (a-c) (~3000 a.u.), while the signal in the tubes carrying flowing water at 3 cm/sec is substantially decreased with  $\alpha_{min}$  of  $20^\circ$  (~60 a.u.), compared to  $\alpha_{min}$  of  $40^\circ$  (~120 a.u.) and  $\alpha_{min}$  of  $80^\circ$  (~540 a.u.), consistent with theoretical signal simulated using the extended phase graph algorithm including the phase accrual due to motion (d). Also, note the decrease in pulsatile artifacts on images with lower refocusing flip angles due to flow suppression.

Multi-echo TSE-mDixon employing partial echo acquisition and homodyne reconstruction with phase preservation successfully reconstructed the fat/water separated images that were qualitatively equivalent to multi-acquisition TSE-mDixon, but in half the scan time (Figure 4-2). The reduced refocusing flip angles of the 3D TSE acquisition increased the sensitivity to motion, suppressing the signal in the flow phantom at 3 cm/sec using a  $\alpha_{min}$  of  $20^\circ$  (Figure 4-3). The signal intensities of the flowing water to the static

phantom were: 2% ( $\alpha_{\min} = 20^\circ$ ), 4% ( $\alpha_{\min} = 40^\circ$ ) and 18% ( $\alpha_{\min} = 80^\circ$ ). Since the blood flow in major veins surrounding the brachial plexus (e.g. subclavian veins) are expected to be greater than 3 cm/sec (86),  $\alpha_{\min}$  of  $20^\circ$  was used in all human studies.

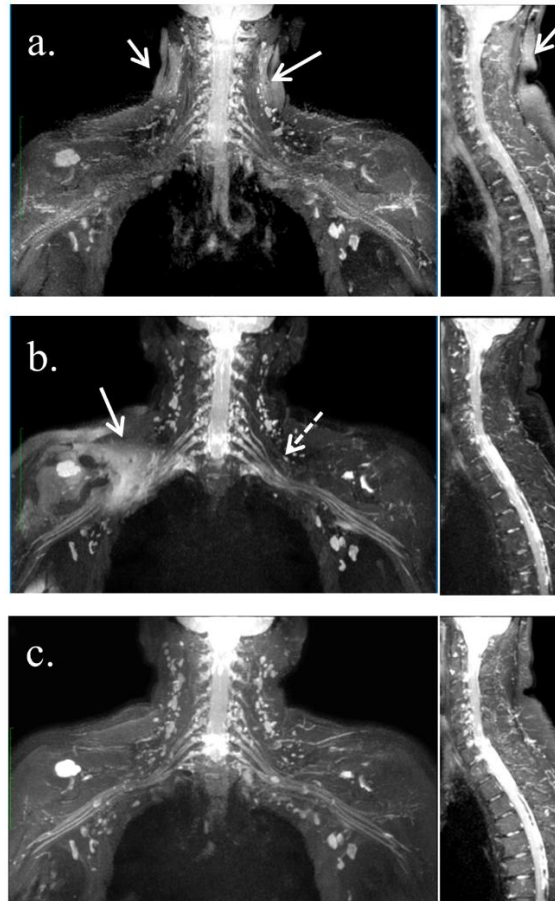


**Figure 4-4 Brachial plexus images of a healthy volunteer acquired with STIR, SPAIR and multi-echo mDixon**

Targeted MIP images of the brachial plexus acquired in coronal (left column) and reformatted to sagittal orientation (right column) of a healthy volunteer (52-year-old female) acquired with 3D TSE STIR (a), 3D TSE SPAIR (b) and multi-echo 3D TSE-mDixon (water-only images) (c), all acquired in 6:00 minute scan each. TSE-mDixon (c) shows uniform fat suppression with improved nerve delineation, while the fat suppression is non-uniform with both STIR (a) and SPAIR (b) (arrows) obscuring the nerve visualization.

The targeted MIP images of a representative healthy volunteer show uniform fat suppression with improved brachial plexus conspicuity throughout the volume using 3D TSE-mDixon (Figure 4-4). The fat suppression with 3D TSE STIR is relatively uniform in the center of the volume but suffers from poor fat suppression at the edges of the field of view (Figure 4-4a, arrow) and reduced SNR. The nerve visualization with 3D TSE SPAIR is improved in certain parts of the image (Figure 4-4b, dashed arrow), but suffers from non-uniform fat suppression (Figure 4-4b, arrow) due to increased sensitivity to  $B_0$  inhomogeneities. The arteries and veins were well suppressed on all images. Multiplanar MIP images of a different volunteer show visualization of the nerves with increased delineation throughout the volume with uniform fat, arterial and venous suppression.

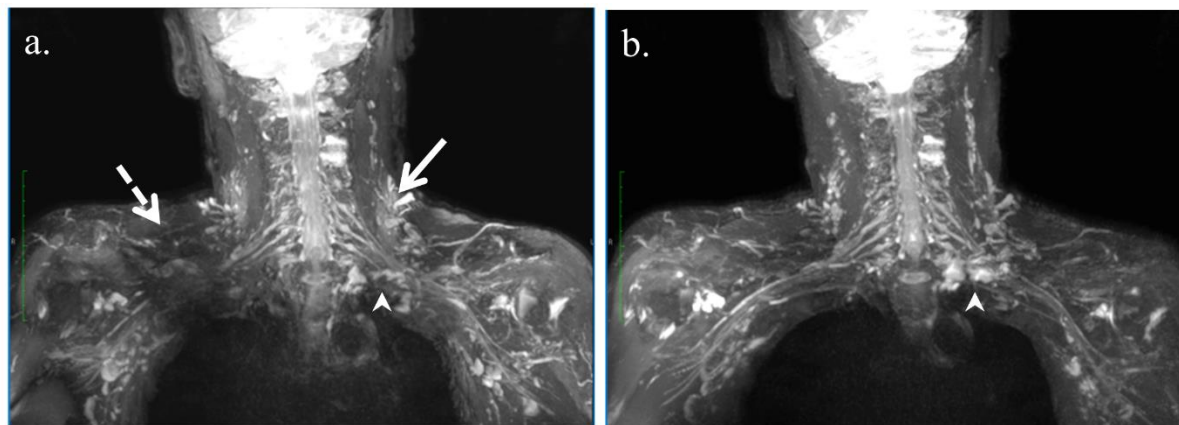


**Figure 4-5 Brachial plexus images of a patient acquired with STIR and multi-echo mDixon**

Targeted MIP images of a patient (60-year-old male) referred to evaluate upper trunk plexopathy with left arm paralysis acquired with 3D TSE STIR (a) and multi-echo 3D TSE-mDixon (b). Incomplete fat suppression on 3D TSE STIR (arrow) obscures the hyperintensity of the suprascapular and axillary nerves of the left upper trunk (arrowhead), which is conspicuous on 3D TSE-mDixon.

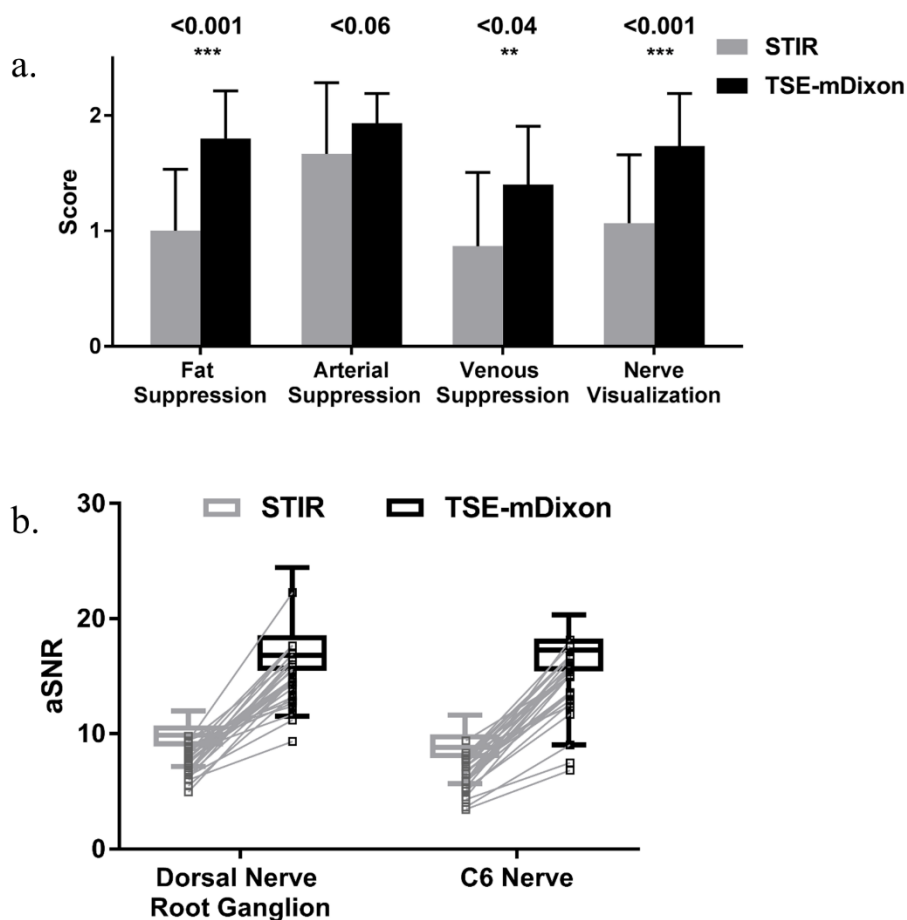


**Figure 4-6 Qualitative and quantitative assessments of brachial plexus images acquired using STIR and multi-echo mDixon**

Graphs shows results of (a) qualitative and (b) quantitative assessments and reveal the superior performance of 3D TSE-mDixon compared to 3D TSE STIR using data from 5 healthy volunteers and 10 patients. Fat suppression ( $p < 0.001$ ), venous suppression ( $p < 0.04$ ) and nerve visualization ( $p < 0.001$ ) were significantly better with 3D TSE-mDixon. Arterial suppression was better but not statistically significant ( $p < 0.06$ ). Apparent signal to noise ratio (aSNR), defined as the ratio of the signal mean to its standard deviation, of 3D TSE-mDixon increased statistically significant compared to 3D TSE STIR ( $p < 0.001$ ) in both dorsal nerve root ganglion (mean  $\pm$  std:  $17 \pm 2.4$  vs.  $9.8 \pm 1.2$ ) and C6 nerve (mean  $\pm$  std:  $16.5 \pm 2.7$  vs.  $8.7 \pm 1.5$ ).

The uniform fat suppression enhanced the visualization of the nerves and the abnormalities in patients referred for the evaluation of brachial plexopathy (Figure 4-5). In addition to non-uniform fat suppression, 3D TSE STIR also suffered from shading artifacts (Figure 4-5a, dashed arrow) in the areas of increased  $B_1$  inhomogeneities. The increased conspicuity of the nerves was observed throughout the volume across multiple patients. Fat suppression, blood suppression and nerve visualization scores across all subjects (5 healthy volunteers and 10 patients) were qualitatively higher with 3D TSE-mDixon compared to 3D TSE STIR (Figure 4-a). Fat suppression, venous suppression and nerve visualization were significantly higher ( $p < 0.05$ ), while the arterial suppression was better but not statistically significant ( $p = 0.06$ ). 3D TSE-mDixon had statistically significant aSNR increase compared to 3D TSE STIR ( $p < 0.001$ ) in both dorsal nerve root ganglion (mean  $\pm$  std:  $17 \pm 2.4$  vs.  $9.8 \pm 1.2$ ) and C6 nerve (mean  $\pm$  std:  $16.5 \pm 2.7$  vs.  $8.7 \pm 1.5$ ; Figure 4-6b). The interaction between fat suppression method and nerve type was not significant ( $p = 0.3$ ).

#### 4.5 DISCUSSION

MRN is increasingly performed at 3T due to higher SNR compared to 1.5T and the increasing availability of 3T scanners at many imaging centers (87-89). Brachial plexus MRN is challenging due to its unique anatomy that renders it sensitive to  $B_0$  and  $B_1$  inhomogeneities for uniform fat and blood suppression across the entire volume (90). While these basic problems exist at all field strengths, the artifacts are more pronounced at 3T due to increased  $B_0$  and  $B_1$  inhomogeneities. The preliminary results using low refocusing flip angle based 3D TSE combined with multi-echo mDixon provides uniform fat, arterial and

venous suppression enhancing the visualization of the brachial plexus in multiplanar orientations in clinically feasible scan times. This approach also provides volumetric brachial plexus MRN with and without fat suppression in the same acquisition, thus increasing scanning efficiency by replacing multiple 2D acquisitions.

Compared to the standard of care 3D TSE STIR, the acquisition of both echoes in the same TR with 3D TSE-mDixon increased the echo spacing from 2.8 ms to 5.3 ms. This increased RF echo spacing reduced the total number of echoes that could be acquired without significant signal decay. Specifically, the echo train length was decreased from 160 with 3D TSE STIR to 100 with 3D TSE-mDixon and correspondingly the TR was decreased from 3000 ms to 2000 ms to maintain the same scan time. Nevertheless, TSE-mDixon had superior aSNR compared to STIR due to the signal averaging afforded by the acquisition of two echoes. Additionally, the increased RF echo spacing with TSE-mDixon contributed to better arterial and venous suppression compared to TSE STIR.

Our study has a few limitations including a small number of patients (n= 10). The preliminary results from our feasibility study need further validation in a larger cohort. Second, the signal in the major veins was significantly suppressed with lower refocusing flip angles, however, the superficial smaller veins were not sufficiently suppressed. Future implementation with blood suppression strategies such as motion sensitizing driven equilibrium (91) may further suppress signal in these smaller vessels. Third, the multi-echo approach to acquire both IP and OP echoes in the same repetition at  $\delta t = 1.05$  ms, limits the spatial resolution along the readout direction. In our preliminary study, we used a partial echo factor of 0.8 to achieve 1.4 mm resolution, which can be further reduced to 0.6 to achieve 1

mm resolution. Further reduction in spatial resolution (i.e.  $< 1$  mm) along the readout direction would require multi-acquisition TSE-mDixon with the current hardware (on Philips Ingenia 3T scanner) at double the scan time.

In conclusion, multi-echo 3D TSE-mDixon provides robust fat and blood suppression resulting in increased conspicuity of the nerves in clinically feasible scan times and can be used for MR neurography of brachial plexus at 3T.

## **CHAPTER FIVE**

### **Volumetric T2-Weighted and “FLAIR-like” Imaging with Uniform Fat Suppression in a Single Acquisition: Application to Cervical Spine Imaging**

#### **5.1 OVERVIEW**

Portions of this work were presented at the 25<sup>th</sup> annual meeting of International Society for Magnetic Resonance in Medicine (ISMRM) in Honolulu (April 2017). The work will be submitted for publication.

#### **5.2 INTRODUCTION**

T2-weighted turbo spin-echo (T2w-TSE) sequences are widely used in the clinical spine and brain imaging because of their remarkable contrast and sensitivity in detecting lesions, which commonly present with hyper-signal intensity. However, these hyper-intense lesions are often adjacent to fat and cerebrospinal fluid (CSF), which also appear bright on T2w-TSE. To better delineate the tissues and lesions adjacent to the fat and/or CSF (e.g. brain, spine), fluid and/or fat suppression methods are often utilized in T2w-TSE sequences. For the imaging of tissues with the coexistence of fat and CSF (e.g. orbit), combined fat and CSF suppression offers important advantages over the other conventional methods, including high sensitivity and specificity (17,18,92). Furthermore, simultaneous fat and fluid suppression can reduce ghosting and other image artifacts from the fat due to high parallel imaging factors such as SENSE and improve image contrast (93,94).

The conventional combined fat- and fluid-suppression sequence integrates fluid-attenuated inversion recovery (FLAIR) and spectral presaturation with inversion recovery (SPIR) (17). In this hybrid sequence, FLAIR utilizes a non-selective inversion pulse to invert

the magnetizations of both CSF and other tissues, and a spectral selective saturation pulse of SPIR is applied to saturate the signal from adipose tissue at the null point of CSF, then the excitation and data collection are followed. Although this method can produce simultaneous fat and CSF suppression, it is not efficient and not robust in challenging areas with large  $B_1$  and  $B_0$  inhomogeneities, such as the spine. First, a long inversion recovery (IR) time is required for FLAIR, resulting from the long  $T_1$ -relaxation time of CSF, which significantly increases the imaging time. Second, FLAIR also can reduce the SNR as the longitudinal magnetizations of the tissues of interest do not completely return to the thermal equilibrium state at the null point of CSF signal. Third, although the spectral selective saturation pulse of SPIR does not affect the water signal, it is sensitive to  $B_1$  and  $B_0$  inhomogeneities, resulting in incomplete fat suppression (19).

Currently, several alternative fluid suppression methods have been proposed, including FLAIR with multi-slice acquisition (95), hybrid encoding (96) and subtraction based fluid suppression methods (46,48). The subtraction based fluid suppression methods showed robust fluid suppression and simultaneously generated both the conventional  $T_2w$  and FLAIR-like images without increasing the total scan time. Several alternative fat suppression methods are also developed and evaluated in the clinic, including short tau inversion recovery (STIR), spectral adiabatic inversion recovery (SPAIR) and Dixon methods (33,76,87). Although SPAIR is insensitive to  $B_1$  inhomogeneity, it is also sensitive to  $B_0$  inhomogeneity and fails to suppress the fat completely in challenging areas. STIR shows robust fat suppression, but it suffers from low SNR and long repetition time. Instead, Dixon methods have shown robust fat/water separation with better SNR (51), while the scan

time is long as multiple echoes needed. Previously, we developed the multi-echo Dixon TSE, achieving robust water/fat separation without increasing the total scan time at 3 T (Chapter 4) (97). However, the combined fat and fluid suppression using these alternative methods haven't been implemented due to the considerations of scan time and technique limitations, such as subtraction artifacts and inaccurate water/fat separation in low SNR images.

The purpose of this work was to develop a 3D multi-contrast T2-weighted imaging sequence to achieve uniform fat and fluid suppression in a single acquisition. The proposed sequence can provide multi-contrast images, including standard T2w, fat-suppressed T2w, FLAIR-like T2w, fat-suppressed FLAIR-like T2w and T2w myelogram images in a single acquisition using same acquisition time compared with conventional 2D T2-FLAIR imaging.

## **5.3 MATERIALS AND METHODS**

### **5.3.1 Dual-Acquisition TSE with Dual-Echo Dixon**

The dual-acquisition 3D TSE with dual-echo Dixon sequence is shown in Figure 5-1a. The sequence generates 4 sets of echoes, including two gradient echoes (in-phase, IP; out-of-phase, OP) at both shorter and longer TEs ( $TE_1/TE_2$ ) in a single repetition. The IP and OP echoes are generated with the bipolar acquisition. A flyback gradient is inserted after the acquisition, which has a larger gradient strength to reduce the echo spacing in case of partial echo acquisition. Partial echo acquisition is employed in dual-echo Dixon to reduce the echo spacing and to balance the receiver bandwidth and SNR without changing the optimized time interval between IP and OP echoes ( $\sim 1.1$  ms at 3 T). A pair of crusher gradients is added to spoil the free induction decay (FID) following each refocusing pulse. In addition, enhanced readout gradients with a larger strength (35.6 mT/m) and a smaller slew

rate (128.6 mT/m/ms) are used to further reduce the FID artifacts, as the gradient can further decay the FID signal prior to the data acquisition.

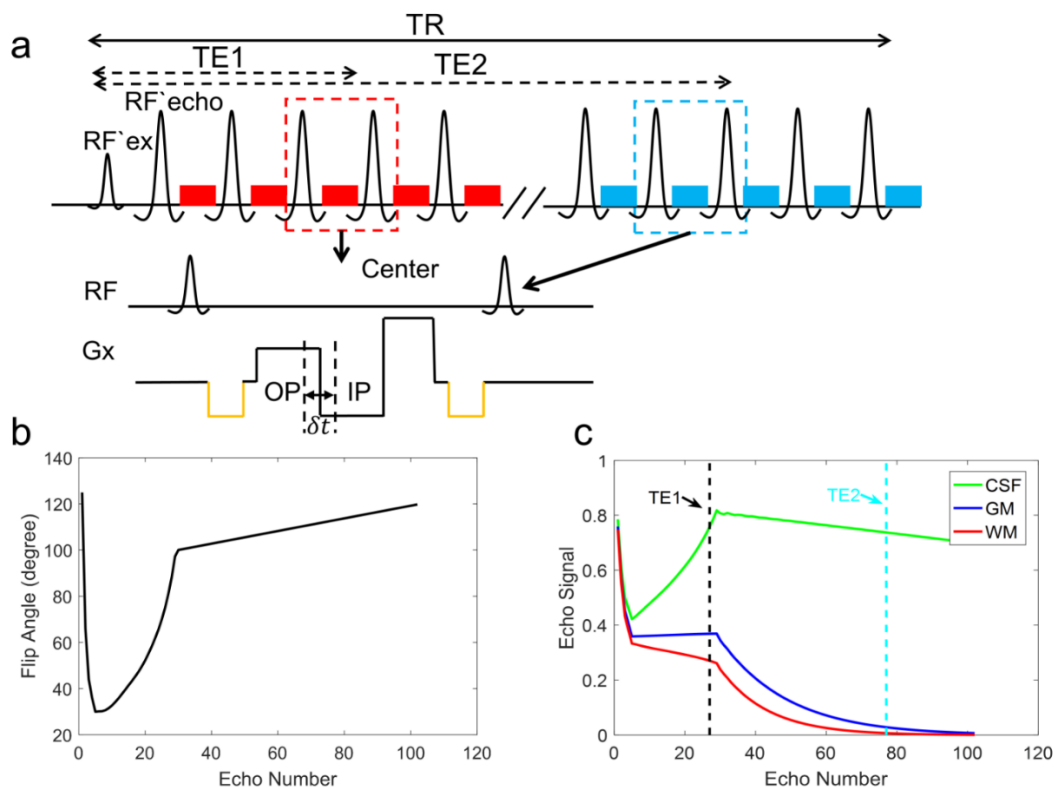


**Figure 5-1 Schematic diagram of the dual-acquisition 3D TSE sequence with dual-echo Dixon**

(a) This sequence generates 4 sets of images, including in-phase (IP) and out-of-phase (OP) images at shorter TE (TE1) and longer TE (TE2) in the same repetition. Partial echo acquisition was implemented, and flow compensation was used. (b) Variable refocusing flip angles with 30 (min) – 60 (center) – 180 (max) were used. (c) The signal evolutions of CSF, GM and WM were simulated using the extended phase graph algorithm.

Variable refocusing flip angles (Figure 5-1b) were used to reduce the specific absorption rate (SAR). It not only allows for longer echo trains to reduce the scan time, but also modulates the signal evolutions of tissues to enlarge the signal difference between CSF

and tissues of interest (e.g. gray matter, GM and white matter, WM) in long TE images.

Bloch equation simulation was performed to verify the signal evolutions with the following parameters: flip angle – 30 (min) – 60 (center) – 180 (max); echo train length – 100; echo spacing – 6.4 ms; TR – 3500 ms; T1/T2 – 4500/2200 ms for CSF, 850/56 ms for WM and 1300/71 ms for gray matter (11,14).

### 5.3.2 Shared-Field-Map Dixon Reconstruction

Since the majority of the tissue signals decay at longer TE (TE2), the overall signal to noise ratio (SNR) is poor, and tissues with long T2 are isolated, like CSF, nerves and vertebral bone marrow. Under these conditions, it is challenging to resolve error phase ambiguity for proper fat/water separation at TE2, resulting in water-fat swapping. However, IP and OP echoes at longer TE are acquired in the same repetition as those at shorter TE, which has higher SNR and robust water-fat separation. The field map estimated with shorter TE images can serve as a priori knowledge to improve the water/fat separation at longer TE.

The four complex composite signals can be modeled as:

$$S_1 = (W_{TE1} + c_1 F_{TE1})e^{i\varphi_1} \quad \text{Equation 5.1}$$

$$S_2 = (W_{TE1} + c_2 F_{TE1})e^{i\varphi_2} \quad \text{Equation 5.2}$$

$$S_3 = (W_{TE2} + c_1 F_{TE2})e^{i\varphi_3} \quad \text{Equation 5.3}$$

$$S_4 = (W_{TE2} + c_2 F_{TE2})e^{i\varphi_4} \quad \text{Equation 5.4}$$

with

$$c_n = \sum_m w_m e^{i(2\pi\Delta f_m + iR_m)\Delta t_n} \quad \text{Equation 5.5}$$

where the index  $m$  indicates spectral peaks of fat with off-resonance frequency  $\Delta f_m$  and transverse relaxation rates  $R_m$ .  $\Delta t_n$  is the echo time shift with respect to Hahn echo.  $W$  and  $F$  are considered as complex,  $W' = W e^{i\psi_1}$ ;  $F' = F e^{i\psi_1}$ . With this approach, the two echoes at shorter TE can undergo standard Dixon reconstruction using the estimated  $\Delta\phi_{TE1} = e^{i(\phi_2 - \phi_1)}$  (40,44). This generates  $W_{TE1}$  and  $F_{TE1}$  as (40):

$$\begin{pmatrix} W'_{TE1} \\ F'_{TE1} \end{pmatrix} = \frac{1}{c_2 - c_1} \begin{bmatrix} c_2 & c_1 \\ -1 & 1 \end{bmatrix} \begin{pmatrix} S_1 \\ S_2 \Delta\phi_{TE1}^* \end{pmatrix} \quad \text{Equation 5.6}$$

Assuming the B0 field changes slowly, it should remain the same between TE1 and TE2 as all echoes are acquired in the same repetition and the time difference between two TEs is around 300 ms. Hence,  $\Delta\phi_{TE2} = e^{i(\phi_4 - \phi_3)}$  is assumed to be identical to  $\Delta\phi_{TE1}$ . Using this shared B0 field map between shorter TE and longer TE,  $W'_{TE2}$  and  $F'_{TE2}$  can be directly calculated as

$$\begin{pmatrix} W'_{TE2} \\ F'_{TE2} \end{pmatrix} = \frac{1}{c_4 - c_3} \begin{bmatrix} c_4 & c_3 \\ -1 & 1 \end{bmatrix} \begin{pmatrix} S_3 \\ S_4 \Delta\phi_{TE1}^* \end{pmatrix} \quad \text{Equation 5.7}$$

In the conventional CSF reduction method (46), the fluid-attenuated images were generated using magnitude subtraction, which can result in subtraction artifacts. Using these two reconstructed complex water-only images, the fat-suppressed FLAIR-like images can be calculated using the complex subtraction to eliminate the subtraction artifacts:

$$I = \text{Real}[(W'_{TE1} - W'_{TE2})e^{-i\psi_1}] \quad \text{Equation 5.8}$$

with  $\psi_1 = \angle W'_{TE1}$ . The workflow of the shared-field-map Dixon reconstruction is shown in Figure 5-2.

### 5.3.3 Experimental Studies

The proposed sequence was implemented in a 3-T Ingenia MR Scanner (Philips Healthcare, Best, the Netherlands). 7 healthy volunteers (3 females, age: 24-61) with IRB approval and written informed consent were enrolled for the sequence and reconstruction evaluation on the cervical spine. All of the human imaging scans were performed with the head/neck/spine coil for signal reception and the dual-transmit body coil for signal transmission.

**Table 5-1 Parameters of the cervical spine pulse sequences**

Parameter	Sequences			
	2D T2	2D STIR	2D FLAIR	3D Dixon
FOV (mm <sup>3</sup> )	180×120×45	180×120×45	180×120×45	180×120×49
Acquired Resolution (mm <sup>3</sup> )	0.6×0.8×3	0.8×0.9×3	1.35×1×3	1×1×2
Reconstructed Resolution (mm <sup>3</sup> )	0.34×0.34×3	0.34×0.34×3	0.34×0.34×3	0.34×0.34×1
Flip Angles	120	100	120	30-100-120
TE <sub>equivalent</sub> (ms)	80	35	120	87/356
TR (ms)	3000	2550	6000	3000
TI (ms)	-	210	2000	-
Partial Echo Factor	1	1	1	0.8
Echo Train Length/Turbo Factor	20	18	43	100
Scan time (min)	2:30	4:15	4:12	3:36

To evaluate the performance of the proposed method, the clinical standard multi-slice 2D T2-W, 2D FLAIR, 2D STIR and the proposed dual-acquisition 3D TSE with dual-echo Dixon were included in the protocol. All the images are acquired in the sagittal plane. 2D images were acquired without SENSE, while the 3D images were acquired with a SENSE factor of 2 along the phase encoding direction. Variable refocusing flip angles with flow compensation were used in the 3D TSE sequence. Saturation band anterior to the cervical spine was applied to minimize the motion artifacts from the vessels and swallowing. The typical imaging parameters used for 2D T2-W, 2D FLAIR, 2D STIR and dual-acquisition 3D TSE with dual-echo Dixon are shown in Table 5-1.

To show the ability of the proposed method to perform multiplanar reformatting, one healthy volunteer dataset was acquired using high resolution isotropic dual-acquisition 3D TSE with dual-echo Dixon. The acquisition parameters of the high resolution 3D sequence included: sagittal orientation; FOV = 180×120×60 mm; Resolution = 1×1×1 mm; SENSE = 2; echo spacing = 7.5 ms; equivalent TE1/TE2 = 92/378 ms, TR = 3000 ms;  $\delta t = 1.1$  ms; ETL = 100; flip angle = 30 (min) – 100 (central) – 120 (max); total scan time = 8:15 minutes and partial echo factor = 0.8.

### **5.3.4 Image Processing**

To show the improvement of water/fat separation in long TE images, the water- and fat-only images were reconstructed using both the standard Dixon method (40) on the scanner and the shared-field-map Dixon reconstruction, implemented offline in Matlab. Each pair of OP and IP images went through the standard Dixon, reconstructing the water- and fat-

only images at both shorter and longer TEs. Shared-Field-map Dixon reconstruction was performed offline with the complex data using MATLAB (Mathworks, Natick, Massachusetts). The fluid suppressed images with and without fat suppression (FLAIR- and FLAIR-FS-like images) were generated using both complex (Eq. 8) and magnitude subtractions for comparison and artifacts illustration.

### **5.3.5 Image Evaluation**

For the initial evaluation of image quality, quantitative comparisons were performed between conventional 2D images and the corresponding 3D images. The 3D images were reformatted into the sagittal plane with a slice thickness of 3mm to match 2D slice thickness for comparison. Apparent signal to noise ratio (aSNR), defined as the ratio of the signal mean to its standard deviation, was measured on vertebral body, disc, spinal cord and muscle in 2D T2-W and 3D IP images at shorter TE for comparison. The regions of interest (ROIs) were positioned in normal-appearing tissues, avoiding motion artifacts, dehydrated disc, areas with large signal variation in the vertebral body etc. The size and position of these ROIs were identical in the compared images. To evaluate the sensitivity of detecting bone marrow lesions with 2D STIR and 3D water-only images at shorter TE, the contrast ratio (CR) between the spinal cord and the vertebral body was estimated by taking the ratio of the signal intensity of spinal cord to that of the vertebral body. To compare the CSF suppression efficiency, the CR between spinal cord and CSF was measured in 2D FLAIR and 3D FLAIR-like images. GraphPad Prism6 (GraphPad, San Diego, CA) was used to perform the Paired Student's t-tests with  $p < 0.05$  considered statistically significant.

## 5.4 RESULTS

Bloch equation simulation results are shown in Figure 5-1c. The GM and WM signals are heavily decayed at second TE, while the CSF signal is largely preserved between two TEs. The signal difference between CSF and gray/white matter is also enlarged at longer TE. Hence, the subtraction can null the signals from CSF without significantly affecting the contrast between GM and WM.

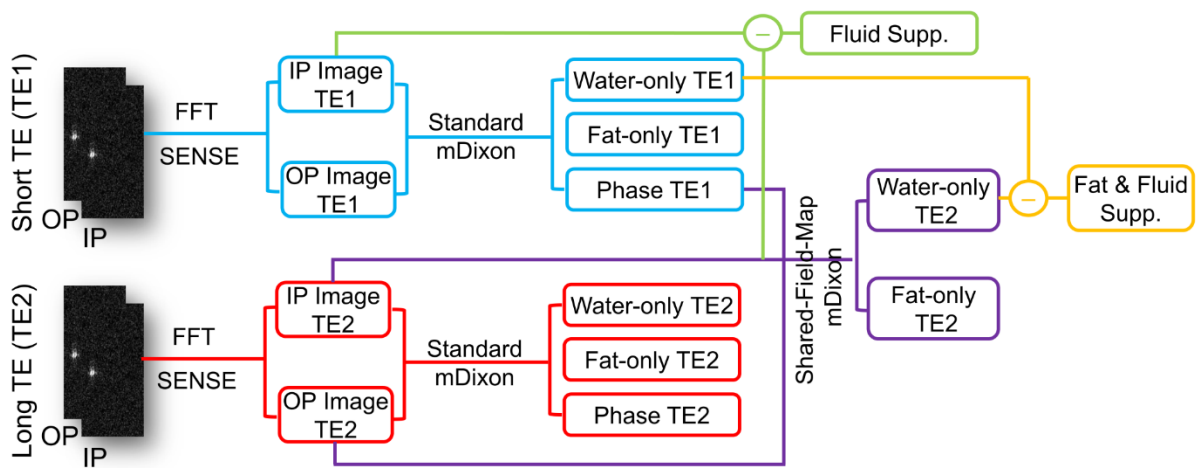


**Figure 5-2 Workflow of shared-field-map mDixon reconstruction**

In standard mDixon reconstruction, images acquired at short TE (TE1) and long TE (TE2) are reconstructed separately (blue and red sections). Due to the low SNR, it is very challenging to estimate an accurate phase map (Phase TE2) from long TE images. Shared-field-map mDixon reuses the phase map estimated from short TE images (Phase TE1) and reconstructs the water- and fat-only images with the IP and OP images at long TE (purple section) to improve the water-fat separation. Then the fluid suppressed (Fluid Supp.) and fat-fluid suppressed (Fat & Fluid Supp.) images can be generated by subtracting the long-TE IP and water-only images from the short-TE IP and water-only images respectively.

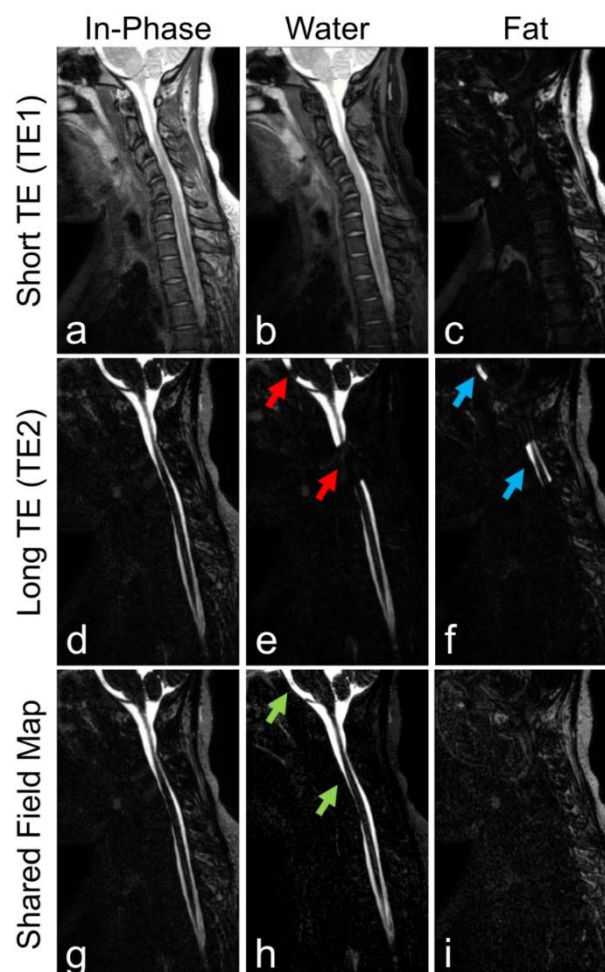


**Figure 5-3 Comparison of shared-field-map mDixon and standard mDixon reconstructions**

Standard mDixon reconstruction provides complete fat/water separation on the short-TE images (a-c), while it fails with the long-TE images (d-f) because of low SNR. Shared-field-map mDixon reconstruction successfully eliminates the water-fat swaps (g-i) by reusing the phase map estimated from short-TE images and achieves uniform fat/water separation.

Figure 5-3 shows the selected volunteer images acquired with the proposed sequence and reconstructed with standard Dixon and shared-field-map Dixon reconstructions. The standard Dixon method provides robust fat/water separation (Figure 5-3b, 3c) from IP and

OP images acquired at shorter TE (TE1) with high SNR. However, it fails to completely separate water and fat from IP and OP images acquired at longer TE (TE2) due to the significantly reduced SNR and tissue isolation, resulting in fat/water swaps (Figure 5-3e, 3f). Using a shared-field-map between TE1 and TE2 images, robust fat/water separation (Figure 5-3h, 3i) was successfully achieved in TE2 images.

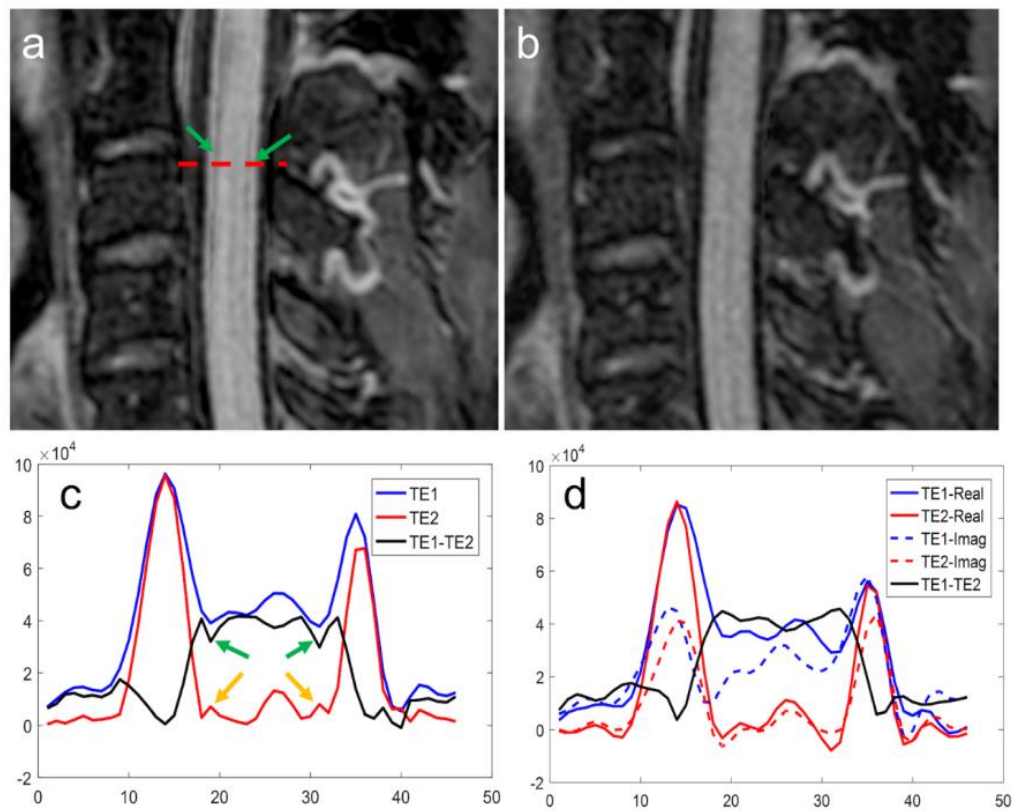


**Figure 5-4 Cervical spine images comparing magnitude subtraction and complex subtraction**

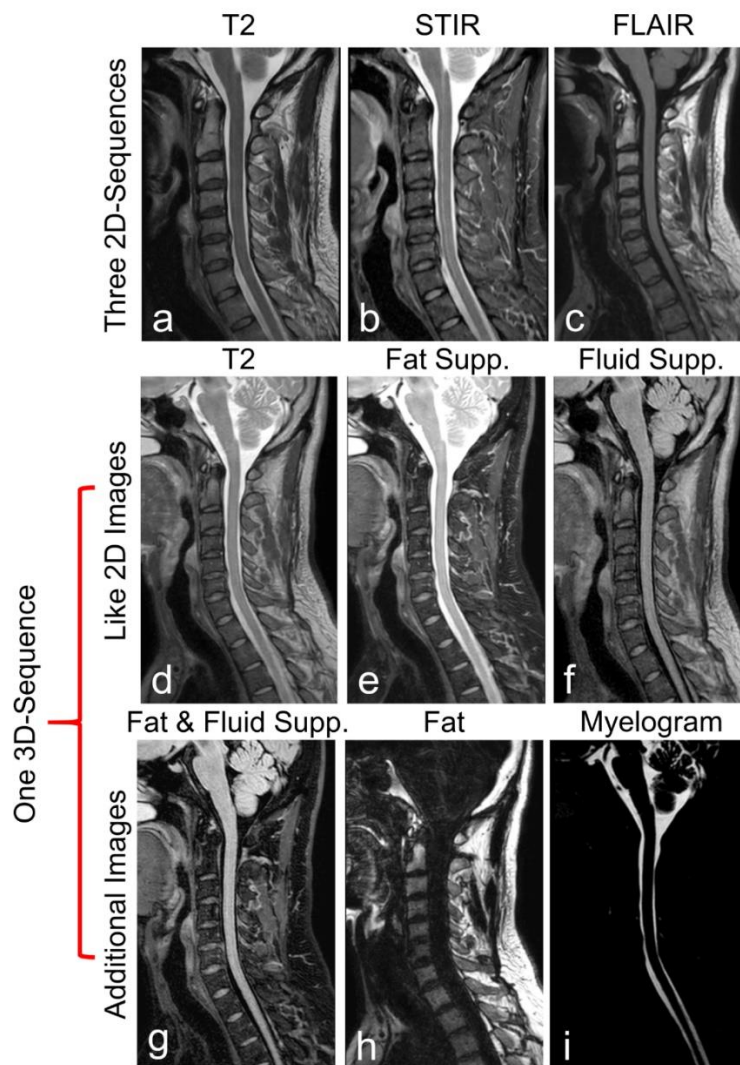
The subtracted images using magnitude subtraction (a) and complex subtraction with phase preservation (b). The “dark-rim” artifacts (green arrows, a) are caused by magnitude subtraction (c). Complex subtraction eliminates the artifacts and results in a smooth profile (d).

Figure 5-4 compared magnitude (Figure 5-4a) and complex subtraction (Figure 5-4b) between the water-only images at TE1 and TE2. The dark-rim artifacts in Figure 5-4a mimic the appearance of Gibbs ringing and motion artifacts resulting from magnitude subtraction. Due to the magnetization modulation and loss of phase information, negative values create local maxima in magnitude images in long TE images (Figure 5-4c, orange arrows), but not in short TE images. The subtraction operation converts these local maxima into local minima (Figure 5-4c, green arrows) and generates these dark lines (Figure 5-4a, green arrows) in the subtracted images. In the shared-field-map Dixon reconstruction, the water and fat signals are complex, and the phase is preserved. The real and imaginary profiles are shown in Figure 5-4d. Using complex subtraction, these subtraction artifacts were eliminated (Figure 5-4b).

The capability of time-efficient multi-contrast 3D imaging using the proposed sequence is shown in Figure 5-5. The clinical 2D sequences, including T2-W (2:30 min), STIR (4:15 min) and FLAIR (4:12 min) were acquired in a total scan time of about 11 minutes with a slice thickness of 3 mm (Figure 5-5a – c). However, Multi-contrast 3D images (T2-W, Fat suppressed T2-W, FLAIR-like, FLAIR-like with fat suppression, Fat-only and Myelogram etc., Figure 5-5d – 5i) were generated using the proposed sequence and reconstruction method in 3:36 min with an acquisition slice thickness of 2 mm and reconstruction slice thickness of 1mm. The fat suppressed T2-W (Figure 5-5e) and fat-only (Figure 5-5h) images are the water-only and fat-only images at shorter TE respectively. FLAIR-like images (Figure 5-5f) were generated by subtracting IP images at longer TE from those at shorter TE, while the fat-suppressed FLAIR-like images (Figure 5-5g) were

generated by subtracting water-only images at longer TE from those at shorter TE.

Myelogram image (Figure 5-5i) is the water-only image at longer TE.



**Figure 5-5 Cervical spine images acquired using the clinical 2d protocol and the proposed sequence**

Images acquired with standard 2D T2-weighted (a, 2:30 mins), 2D T2-STIR (b, 4:15 mins) and 2D T2-FLAIR (c, 4:12 mins). The total scan time is about 11 mins. Using the proposed acquisition and reconstruction method, 3D T2-weighted (d), 3D T2-STIR (e), 3D T2-FLAIR (f), 3D T2-FLAIR with fat suppression (g), 3D Fat-only (h) and 3D Myelogram (i) images are generated in a single acquisition with a total scan time of 3:36 mins.

The ability of the proposed method to perform multiplanar reformatting is shown in Figure 5-6. The conventional 2D cervical spine protocol commonly acquires images with same contrast in multiple orientations (e.g. sagittal and axial planes) to improve the localization of pathology. Although the proposed sequence increased the scan time from 3:36 mins to 8:15 mins for a larger slice coverage, the 3D images acquired in sagittal plane can be reformatted into arbitrary orientations (e.g. axial plane (Figure 5-6f – 6j)), eliminating the necessity of acquiring images in multiple planes and thus reducing the total scan time.

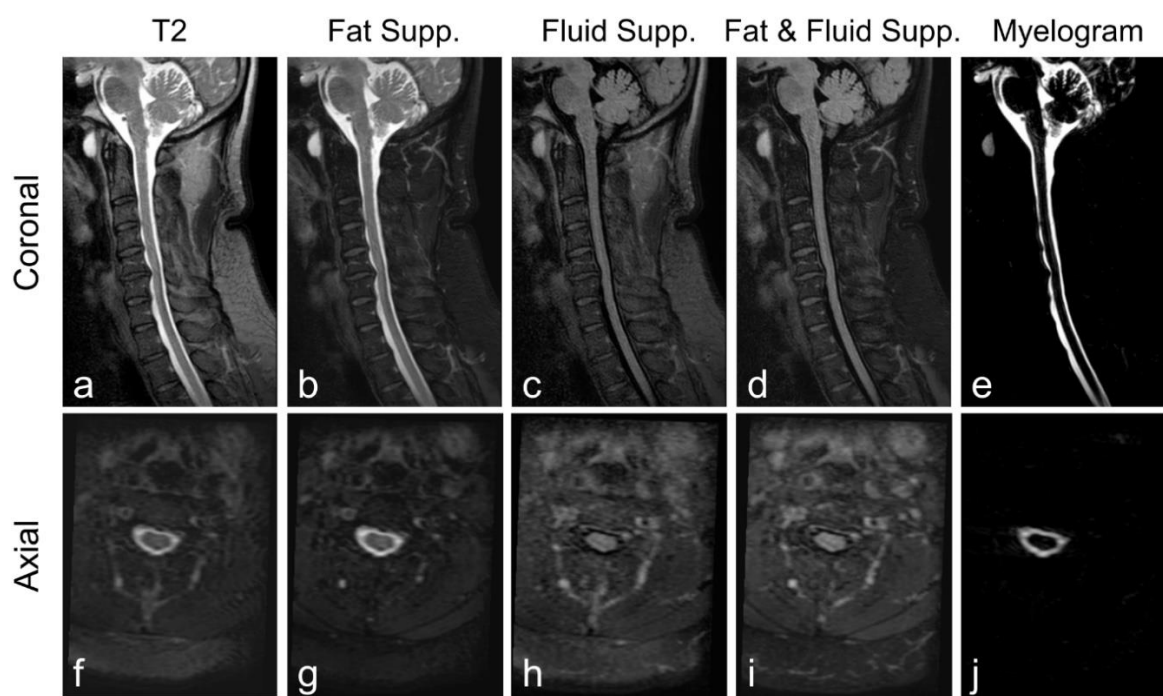


**Figure 5-6 3D cervical spine images acquired with a larger slice coverage**

The 3D reformatted images of T2W (a, f), fat suppressed T2W (b, g), fluid suppressed T2W (c, h), fat & fluid suppressed T2W (d, i) and myelogram (e, j) in both sagittal and axial planes of a normal volunteer using proposed sequence in an acquisition time of 8 mins. The fat & fluid suppressed images (d, i) show homogeneous fat suppression and high conspicuity of nerves and spinal cord.

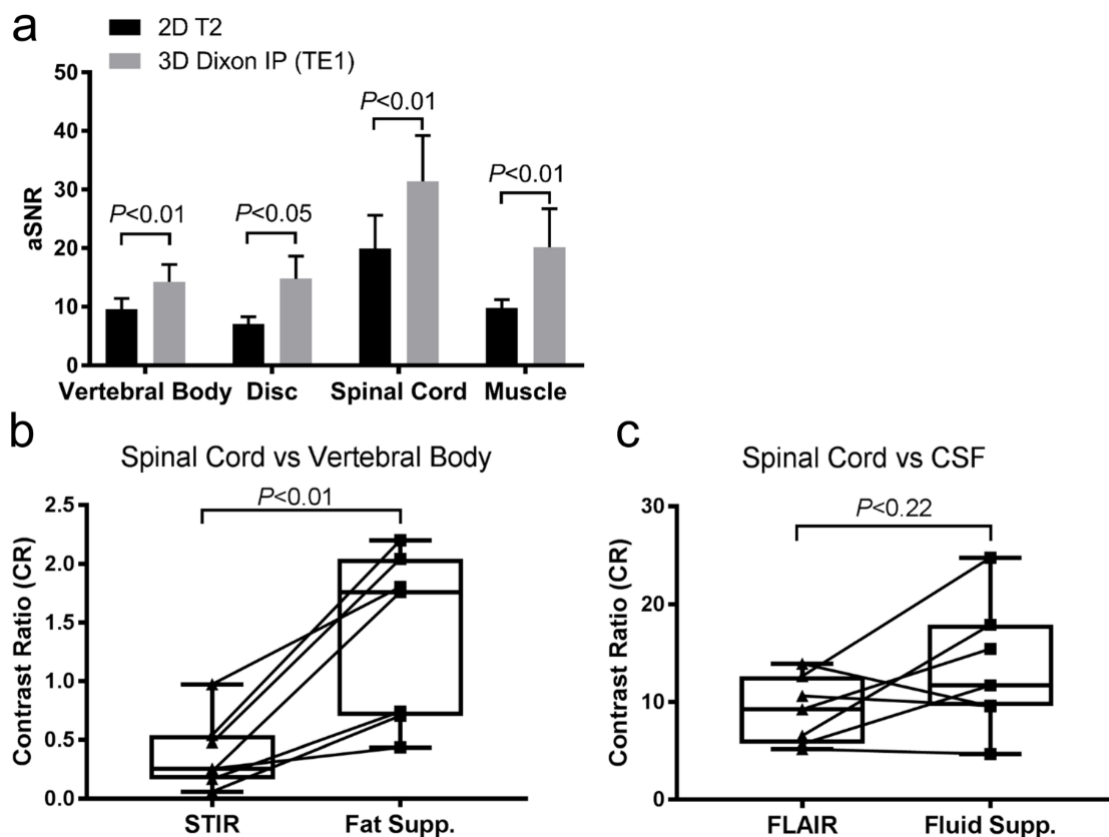


**Figure 5-7 Quantitative assessments of the performance of dual-acquisition 3D TSE with dual-echo Dixon sequence**

Seven healthy volunteers were scanned. Compared to 2D T2W, the IP images at shorter TE had significantly higher aSNR in vertebral body ( $p < 0.01$ ), disc ( $p < 0.05$ ), spinal cord ( $p < 0.01$ ) and muscle ( $p < 0.01$ ). The contrast ratio between the spinal cord and vertebral body is significantly higher in the water-only image at shorter TE than 2D STIR ( $p < 0.01$ ). FLAIR-like images tend to provide higher contrast ratio between the spinal cord and CSF than 2D FLAIR, but is not statistically significant ( $p < 0.22$ ).

The results of the quantitative analysis are shown in Figure 5-7. Compared to 2D T2W, the IP images at shorter TE have statistically significant aSNR increase in vertebral body (mean  $\pm$  std:  $14 \pm 3$  vs.  $9.6 \pm 1.8$ ;  $p < 0.01$ ), disc (mean  $\pm$  std:  $15 \pm 3.9$  vs.  $7.1 \pm 1.2$ ;  $p < 0.05$ ), spinal

cord (mean  $\pm$  std:  $31\pm 7.8$  vs.  $20\pm 5.7$ ;  $p<0.01$ ) and muscle (mean  $\pm$  std:  $20\pm 6.6$  vs.  $9.8\pm 1.4$ ;  $p<0.01$ ). The CR between the spinal cord and vertebral body is significantly higher in the water-only images at shorter TE (mean  $\pm$  std:  $14\pm 0.73$ ) compared to 2D STIR (mean  $\pm$  std:  $0.39\pm 0.31$ ,  $p<0.01$ ). FLAIR-like images tend to provide higher CR between the spinal cord and CSF than 2D FLAIR, but is not statistically significant (mean  $\pm$  std:  $13\pm 6.6$  vs.  $9.1\pm 3.5$ ;  $p=0.22$ ).

## 5.5 DISCUSSION

A dual-acquisition 3D TSE sequence with dual-echo Dixon and shared-field-map reconstruction was introduced for simultaneous fat and fluid suppression as well as multi-contrast imaging, including 3D T2-W, FLAIR-like, fat-suppressed T2-W, fat-suppressed FLAIR-like T2-W and Myelogram in a single acquisition at 3 T. Since IP and OP echoes at two TEs were acquired in the same repetition, the scan time of this sequence was maintained the same as the conventional FLAIR. With dual-echo Dixon and shared-field-map reconstruction, uniform fluid suppression such as CSF and water/fat separation were achieved in cervical spine due to the insensitivity to B1 and B0 inhomogeneities.

Conventional FLAIR exploits the difference in T1 relaxation times between CSF and other tissues, while the subtraction based fluid-attenuation methods mainly rely on the difference in T2 relaxation times. Besides the T1, CSF has a much longer T2 ( $\sim 2000$  ms) (98) than the other soft tissues, including muscle, grey and white matter. Without using the inversion pulse and delay, the subtraction based fluid-attenuation methods can largely preserve T2-weighted contrast.

Although the current available Dixon methods are insensitive to the  $B_1$  and  $B_0$  inhomogeneities, it is prone to fat/water swaps in images with low SNR. For dual-echo Dixon, low SNR can increase the uncertainty in the estimation of phase values, especially in regions with mixed fat and water, like bone marrow. The uncertainty could be reduced by increasing the echo number, but it will also increase the echo spacing or receiver bandwidth to maintain image resolution. Due to the large signal decay of tissues with short  $T_2$  in long TE images, the number of isolated pixels also increase, introducing additional uncertainty. For example, the vertebral bone in longer TE images shows segmental appearance due to the presence of intervertebral discs. Combined with the rapid field change, it is challenging to eliminate fat/water swaps in long TE images using the currently available methods, including region-growing and graph-cut based Dixon methods. The shared-field-map reconstruction reuses the  $B_0$  map estimate from the short TE images and bypasses the problematic field map estimation for fat/water separation at long TE. The time difference between these two echoes is around 300 ms, thus the assumption that  $B_0$  map doesn't change between two TEs is valid. Another advantage of the shared-field-map reconstruction is that it also saves the total reconstruction time by half as only one field map is required, which is the most time-consuming part for fat/water separation. It should be noticed that the shared-field-map reconstruction not only can be used for multi-echo acquisition, but also can be used in dynamic imaging, T2-prepared imaging and T2 mapping etc.

In previous subtraction-based fluid attenuation method (46), magnitude subtraction was used to suppress the CSF signal, however it was prone to subtraction artifacts. In long TE images, the signals of tissues surrounding the CSF are heavily attenuated, and the

background signals are close to 0. Due to the large signal drop and signal truncation, the Fourier transform creates negative peaks in the real and imaginary images at the edges of CSF. The magnitude operation turns these negative peaks into local maxima in long TE images, resulting in subtraction artifacts. With the complex signal model of water and fat, subtraction artifacts were successfully removed using complex subtraction.

With robust fat/water separation at long TE and complex subtraction, multiple contrast images were produced in a single acquisition. There are several advantages of the multi-contrast capability. First, the total scan time is reduced. Compared to multiple scans, including FLAIR, STIR and T2-W, the proposed sequence reduces the total scan time from 11 mins to 3:30 mins with additional contrasts, including Myelogram, fat-only and simultaneous fat and fluid suppressed images. Second, additional information is provided for the complete evaluation of the spine including detection of spinal metastases, causes of back pain and radicular symptoms etc. With fat and CSF suppression, T2-W images can improve the conspicuity of lesions as well as the nerves. Myelogram images can be used to detect CSF leak and evaluate CSF volume (98,99). Bone marrow pathologies can be evaluated in the fat-suppressed T2 (100). Fat-only and water-only images are useful in the evaluation of the tissue component, differentiating marrow replacing lesions as well as the evaluation of treatment (101). Multiple clinical examinations can probably benefit from the proposed sequence. Future clinical studies will evaluate the performance of this sequence. Third, the multi-contrast images are perfectly co-registered, since all the images are generated from a single acquisition.

Compared to the 2D acquisition, the 3D acquisition has the intrinsic ability for multiplanar reformation. The images can be reformatted into axial and coronal orientations without additional acquisition. Although the scan time increases from 3:30 minutes to 8 minutes for wider left-right coverage, it still significantly reduces the total scan time. This is because the 2D scans need to be repeated to acquire the axial or/and coronal images, increasing the total scan time to 22 or 33 minutes. Besides saving scan time, the 3D acquisition also provides thinner slice thickness, better localization and delineation of anatomic details.

The 3D T2-W images show comparable image qualities compared to 2D T2-W images. The improvement of aSNR in 3D T2-W images is mainly due to the 3D coverage and larger in-plane voxel size. Compared to 2D STIR, the improved contrast ratio in 3D fat-suppressed T2-W images results from homogeneous fat suppression using Dixon method and enhanced contrast using variable refocusing flip angles. Reduced sharpness is also observed in 3D T2-W and fat suppressed images compared to the corresponding 2D images. This is because 1) the in-plane resolution of 2D T2 and 2D STIR is higher than 3D acquisition; 2) long echo train length is used in the 3D acquisition. The sharpness can be improved by optimizing the variable refocusing flip angles or increasing the in-plane resolution with balancing contrast and SNR (102).

Although similar fluid suppression is achieved using the subtraction method compared to 2D FLAIR, the subtraction based fluid attenuation method has its own limitations. It also reduces the signal intensity of tissues with longer T2 than most normal tissues instead of suppressing tissues with longer T1 in FLAIR. To address this issue,

protocol parameters, including TR, TE and variable flip angles can be optimized to minimize the undesired tissue suppression. As multi-contrast images are generated, the long T2 tissues are preserved in T2-W images with/without fat suppression. Complete information can be provided if these images are combined. Although we mentioned that the optimization of the variable refocusing flip angles can improve the sharpness and adjust the contrast, it should be noted that it also can mix the T1 and T2 contrast. For example, the vertebral discs show higher signal intensity in 3D TSE with variable refocusing flip angles, compared to the conventional 2D T2-W. Therefore, the future optimization should also take the image contrast into consideration. However, on the other hand, the enhancement of tissue with shorter T1 also can improve the contrast (103). To evaluate the impacts on diagnosis, more patient studies need to be performed in the future.

## 5.6 CONCLUSION

We have demonstrated that the proposed sequence is effective in simultaneous fat and fluid suppression as well as in multi-contrast imaging. The proposed shared-field-map reconstruction achieved robust fat/water separation in spite of low SNR, with reduced reconstruction time compared to the standard Dixon method. The subtraction artifacts are identified and eliminated using complex subtraction. As compared to 2D FLAIR, the proposed method shows the ability to attain high-resolution isotropic multi-contrast images in clinically feasible scan times.

## **CHAPTER SIX**

### **Robust Abdominal Imaging with Uniform Fat Suppression using Dixon based Single Shot Turbo Spin Echo**

#### **6.1 OVERVIEW**

Portions of this work were presented at the 24<sup>th</sup> annual meeting of International Society for Magnetic Resonance in Medicine (ISMRM) in Singapore (May 2016). The work will be submitted for publication.

#### **6.2 INTRODUCTION**

Single-Shot Turbo Spin Echo (SShTSE) sequence is widely used in T2-weighted (T2W) body magnetic resonance imaging (MRI) protocols because of its sub-second acquisition time and robustness to  $B_0$  inhomogeneity (33,104-108). However, fat appears bright in T2W images due to a relatively long T2. In addition, the rapid refocusing pulses in SShTSE interrupts the J-coupling (13), and further increases the signal intensity of fat. The high signal intensity of fat reduces the image contrast and conspicuity of lesions in body imaging, especially in abdominal and pelvic imaging (33,109,110).

To increase the lesion conspicuity, fat suppression methods are commonly included in the SShTSE sequence. Among various fat suppression methods, short tau inversion recovery (STIR) is well known for homogenous fat suppression, but it suffers from low SNR in body imaging (111). Compared to STIR, spectral selective fat suppression methods, such as spectral presaturation with inversion recovery (SPIR) and spectral adiabatic inversion recovery (SPAIR) have the advantage of high SNR. Specifically, SPAIR is also insensitive to  $B_1$  inhomogeneity compared to SPIR. However, both SPIR and SPAIR are sensitive to  $B_0$

inhomogeneity, resulting in incomplete fat suppression (5). To achieve robust fat suppression without sacrificing SNR, TSE-based Dixon sequences have been developed (39,54,112).

In TSE-based Dixon sequences, multiple echoes should be acquired at different echo-shifting times with respect to “Hahn” echo to separate water and fat. To acquire these echoes, there are two major acquisition strategies: multi-acquisition Dixon and multi-echo Dixon. In multi-acquisition Dixon, In-Phase (IP) and Out-of-Phase (OP) echoes are acquired in separate repetitions, which can maximize the receiver bandwidth but significantly increase the total scan times. Multi-echo acquisition acquires both IP and OP echoes in the same repetition and therefore reduces the total scan times. However, both multi-acquisition Dixon and multi-echo Dixon have not been combined with SSHTSE for abdominal imaging because of their own limitations. Multi-acquisition Dixon suffers from long scan times and possible additional phase introduced by motion between the two separate repetitions. Although multi-echo Dixon can reduce the scan times, it is very challenging to balance the echo spacing, in-plane resolution and SNR in SSHTSE. Therefore, multi-echo Dixon was only combined with multi-shot TSE for breath-hold abdominal imaging at 1.5T (113), sacrificing the speed and slice thickness.

Previously, we demonstrated a multi-shot TSE sequence with multi-echo Dixon and partial echo acquisition for 3D brachial plexus imaging at 3T (Chapter 4) (57), with improved fat suppression without sacrificing the speed. The optimal time interval between IP and OP echoes for robust fat-water separation is about 1.1 ms at 3T compared to 2.2 ms at 1.5T, reducing the need for increased echo spacing with multi-echo Dixon. In addition, the partial echo acquisition can further reduce the echo spacing as well as improve the in-plane

resolution. However, combining partial echo acquisition with SSHTSE would further reduce the k-space coverage since partial phase encoding is also used in SSHTSE. The commonly used reconstruction method (114) combining 1D homodyne reconstruction and zero-padding could introduce zero-padding artifacts in frequency encoding direction.

In this work, I implemented an SSHTSE sequence with multi-echo Dixon and partial echo acquisition at 3T and demonstrated its ability to improve fat suppression without sacrificing the speed in breath-hold abdominal imaging. A phase preserved homodyne reconstruction with bi-directional homodyne filters was also implemented for robust fat/water separation as well as reducing the zero-padding artifacts.

## 6.3 MATERIALS AND METHODS

### 6.3.1 Pulse Sequence

A SSHTSE based multi-echo Dixon sequence (SSHTSE-mDixon) was implemented on a 3T Ingenia scanner (Philips Healthcare, Best, The Netherlands) for breath-hold abdominal imaging, as shown in Figure 6-1. In the SSHTSE-mDixon, IP and OP images are acquired using bipolar readout gradients after each excitation. The typical echo time shift ( $\delta t$ ) between IP and OP echoes is about 1.1 ms at 3T (57), in contrast to 2.2 ms at 1.5T, and therefore reduces the increase of echo spacing compared to 1.5T. However, given the image resolution and receiver bandwidth, the minimum achievable  $\delta t$  is limited by the gradient slew rate. In order to achieve a shorter  $\delta t$  ( $\sim 1.1$  ms) without sacrificing the image spatial resolution at 3T, the partial-echo acquisition was combined with the partial-phase encoding acquisition, allowing over a quarter of the k-space to be directly acquired (Figure 6-2c, blue section).

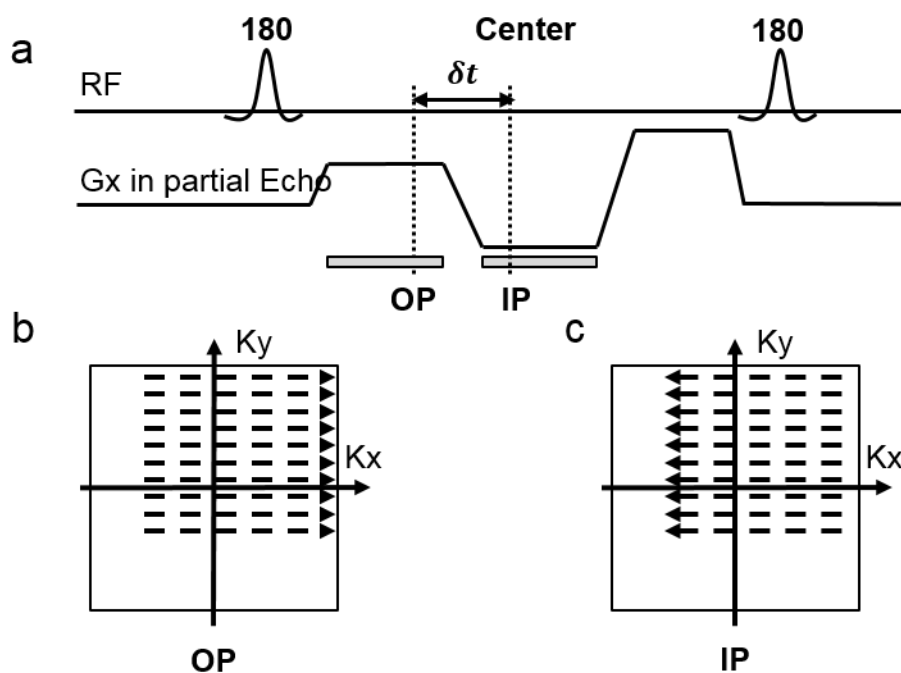


**Figure 6-1 Schematic diagram of the SShTSE based multi-echo Dixon sequence**

(a) pulse sequence diagram: single shot TSE sequence with dual-echo Dixon acquiring IP and OP images in single repetition with partial echo acquisition to maintain the in-plane resolution and optimized IP and OP interval; (b) and (c) are the exemplary k-spaces of the OP and IP images respectively.

### 6.3.2 Image Reconstruction

One-dimensional (1D) homodyne filters are commonly used in SShTSE to compensate the missing k-space in the phase-encoding direction, rather than zero-filling, that are known to cause ringing artifacts. However, the 1D homodyne filters only compensate the missing data in one direction. To handle the two-dimensional partial coverage of k-space, a hybrid homodyne reconstruction method (114), that applies the 1D homodyne filters along the phase-encoding direction and zero-filling along the frequency-encoding direction are typically used. However, the ringing artifacts are notable with this approach, when the partial

echo factors are small ( $< 0.8$ ), limiting the minimum applicable partial echo factor and in-plane resolution.

To address this issue, a phase-preserved bi-directional homodyne reconstruction was developed to minimize the ringing artifacts along both the phase and frequency encoding directions. The bi-directional homodyne filters are an extension of the conventional 1D homodyne filters:

$$L(k_x, k_y) = L(k_x)L(k_y) \quad \text{Equation 6.1}$$

$$H(k_x, k_y) = H(k_x)H(k_y) \quad \text{Equation 6.2}$$

where  $L_y(k)$  and  $H_y(k)$  are the 1D low pass ( $L_y(k)$ ) and high pass ( $H_y(k)$ ) homodyne filters respectively (60). In addition to the compensation in the phase-encoding direction (Fig. 2c, green section), the bi-directional homodyne filters also compensate the central k-space in the frequency-encoding direction (Fig. 2c, orange section), thus reducing the ringing artifacts.

The phase is estimated from the low-resolution image, which is reconstructed from the central symmetrically sampled data. Subsequently, the phase estimated from this low-pass filtered image is concatenated back to the images reconstructed through bi-directional homodyne reconstruction to generate the final complex images. The phase-preserved bi-directional homodyne reconstruction was repeated separately for the IP and OP images, before processing them through the Dixon reconstruction for fat-water separation.

### 6.3.3 Phantom Study

To compare the bi-directional homodyne reconstruction and the hybrid homodyne reconstruction, a phantom study was carried out with a standard MR calibration phantom

(synthetic oil-filled cylinder) provided by Philips Healthcare and a 16-channel head coil. The images were acquired using the proposed sequence with both full-echo and partial-echo acquisitions (partial echo factor = 0.7).

To quantify the signal-to-noise ratio (SNR) of the images acquired using SShTSE, SShTSE-SPAIR and SShTSE-mDixon, a dual acquisition method (115) was used with a phantom consisting of 3 agarose gel samples with the T2 values (80 ms, 63 ms, and 41 ms) close to those of kidney, spleen and liver (12) respectively, and a vial of peanut oil representing subcutaneous fat. The SNR was calculated as  $SNR = \sqrt{2} \frac{SI_{avg}}{SD_{sub}}$ , where  $SI_{avg}$  and  $SD_{sub}$  are the signal intensity and the standard deviation of a ROI over the averaged image and the subtracted image respectively. The entire scan was repeated for 5 times to determine the mean and variation of measured SNRs. The acquisition parameters were identical to those used in the in vivo study.

#### **6.3.4 In Vivo Study**

In total, 5 normal volunteers and 5 patients were enrolled for the sequence evaluation with institutional review board approval and written informed consents. Volunteers and patients were scanned using SShTSE, SShTSE-SPAIR and SShTSE-mDixon sequences with a 16-channel phased-array anterior coil along with a 12-channel phased-array posterior torso coil, embedded in the table. The acquisition parameters of SShTSE and SShTSE-SPAIR included: FOV = 320×420 mm<sup>2</sup>, acquisition resolution = 1.3×1.6 mm<sup>2</sup>, slice thickness = 5 mm, TE<sub>eff</sub> = 80 ms, TR = 1250 ms, refocusing flip angle = 120°, SENSE factor = 3, echo spacing = 5.1 ms, partial phase-encoding factor = 0.69 and receiver bandwidth = 440 Hz/Pixel. The inversion delay and frequency offset of SPAIR were 200 ms and 220 Hz

respectively. The SShtTSE-mDixon used the same acquisition parameters, except echo spacing = 6.7 ms,  $TE_{\text{eff}} = 75$  ms, partial echo factor = 0.8, partial phase-encoding factor = 0.64 and receiver bandwidth = 870 Hz/Pixel. Volunteer images were acquired in the axial and coronal planes. The patient images were only acquired in the axial plane to match the current clinical protocol at our institution. Approximately 48 slices were acquired in 3 breath-hold acquisitions of 15-17 seconds each.

Because of the motion and scan time, the apparent SNR (aSNR) (57) was measured in the liver and spleen instead of measuring the conventional SNR using the dual acquisition method. The contrast ratio (CR) was calculated as the ratio between the signal intensity of the spleen and the signal intensity of the liver. Vessels, lesions, and the edge of organs were avoided when placing ROIs. The aSNR and CR were measured in the axial and coronal volunteer images and were analyzed using the Wilcoxon signed rank test. To evaluate the performance of fat suppression, the number of failed subcutaneous fat and visceral fat suppression cases in both volunteer and patient studies were summarized and were statistically analyzed using the McNemar test. All measurements are presented as mean  $\pm$  standard deviation. GraphPad Prism 6 (GraphPad, San Diego, CA) was used to perform the statistical analysis with  $P < 0.05$  considered statistically significant.

## 6.4 RESULTS

Figure 6-2 shows the phantom images reconstructed using the hybrid homodyne and the bi-directional homodyne reconstructions. The image acquired only with half scan and reconstructed with 1D homodyne filters (fig. 6-2a) serves as a reference. Using the hybrid homodyne reconstruction, the ringing artifacts were noticeable (fig. 6-2b) due to the k-space

truncation in the frequency encoding direction. However, bi-directional homodyne reconstruction compensated the asymmetry k-space at low frequencies (fig. 6-2c) and minimized the ringing artifacts (fig. 6-2d).

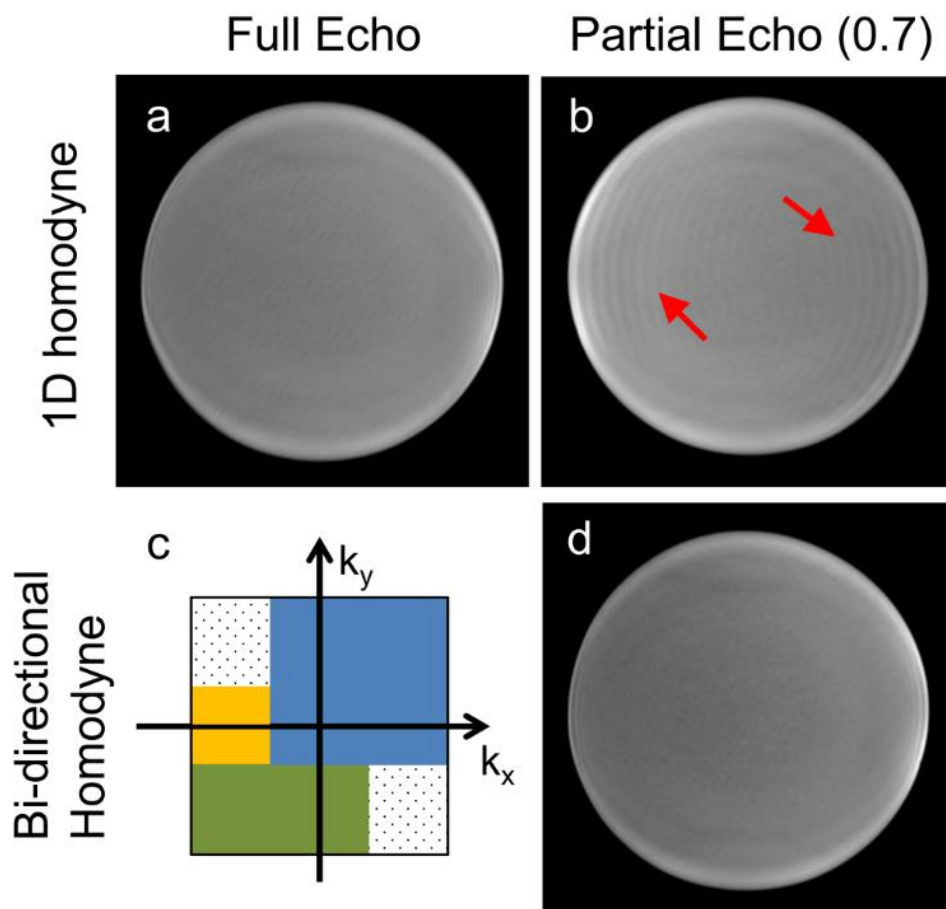


**Figure 6-2 Comparison between bi-directional homodyne and 1D homodyne reconstructions**

(a-b) were acquired with an echo factor of 1 and 0.8 respectively. 1D homodyne reconstruction was applied along phase encoding direction and zero-filling was applied along frequency encoding direction. 1D homodyne reconstruction removes the zero-filling artifact along the phase encoding direction. However, the zero-filling artifacts along the frequency encoding direction (red arrows, b) are more obvious while reducing the partial echo factor. (c) is an exemplary k-space, in which the blue, green and orange sections, respectively, are

directly acquired data, 1D homodyne compensated data and additional compensated data using bi-directional homodyne. (d) was acquired with the same partial echo factor as (b), but was reconstructed using bi-directional homodyne filters, which successfully eliminated the ringing artifacts due to zero-filling along the frequency encoding direction.

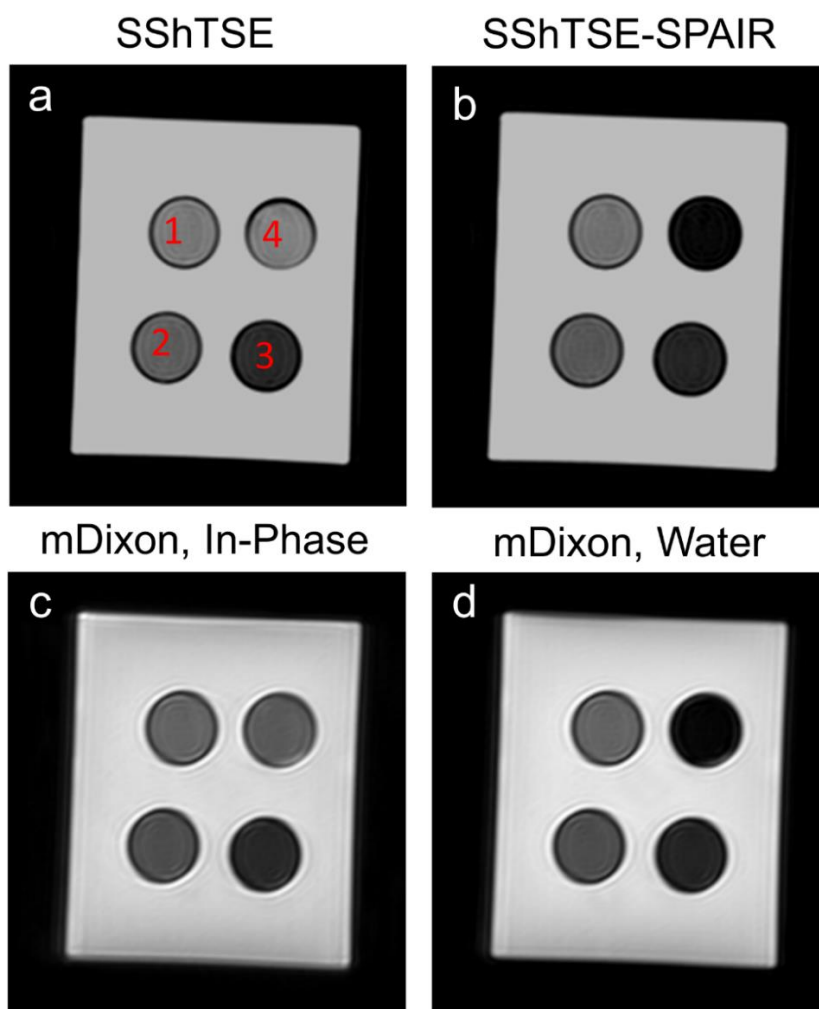


**Figure 6-3 Phantom images for SNR quantification**

SShTSE (a), SShTSE-SPAIR (b) and SShTSE-mDixon (c, d) images of the phantoms used for SNR quantification. Phantom 1, 2 and 3 are agarose gel samples with the T2 values of 85 ms, 67 ms, and 41 ms respectively, which were measured using multi-echo TSE. Phantom 4 is peanut oil. All the phantoms were placed in a water bath.

The SNR measured in the phantoms (Figure 6-3) are shown in Table 6-1. Compared to the standard SSHTSE and SSHTSE-SPAIR images, the IP and water-only images generated from the SSHTSE-mDixon, respectively, showed comparable SNR across all the phantoms.

**Table 6-1 Signal-to-noise ratio calculated in the phantom study**

	Agarose (T2, 80 ms)	Agarose (T2, 63 ms)	Agarose (T2, 41 ms)
SSHTSE	100.3±6.6	78.0±2.8	44.0±1.0
SSHTSE-SPAIR	105.9±8.9	75.8±6.8	36.9±4.2
SSHTSE-mDixon, In-Phase	97.4±10.6	73.9±7.5	46.2±7.4
SSHTSE-mDixon, Water	126.6±13.8	96.8±9.9	53.2±5.9

\* mean ± standard deviation of 5 measurements

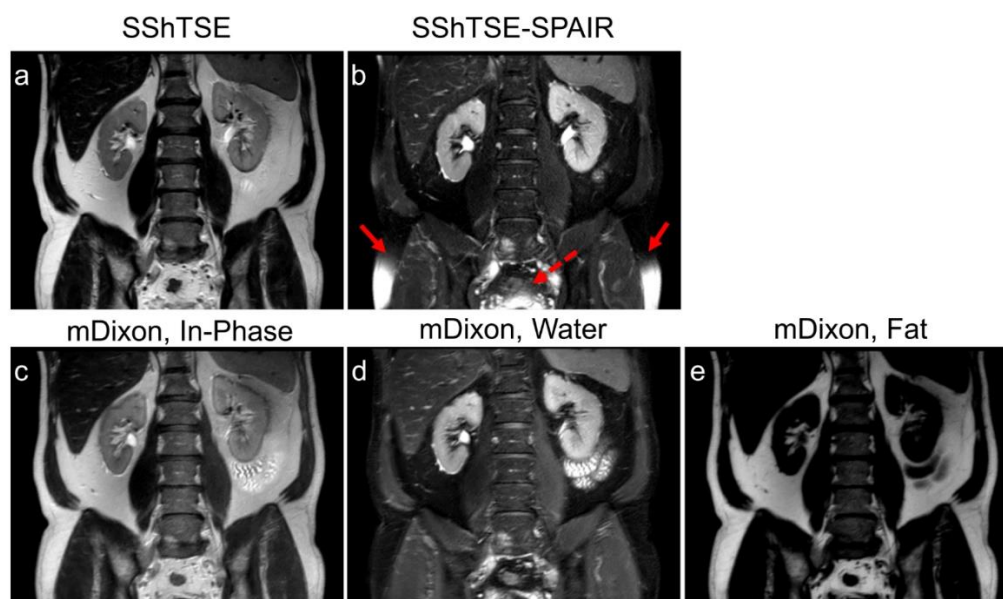


**Figure 6-4 Coronal SSHTSE images of a healthy volunteer acquired with/without fat suppression and dual-echo Dixon**

SSHTSE images of a healthy volunteer acquired without (a) and with SPAIR (b). IP (c) image of the same location acquired using SSHTSE with dual-echo Dixon, and the reconstructed water-only (d) and fat-only (e) images. Red solid arrows show incomplete subcutaneous fat suppression. Red dashed arrow shows the visceral fat that was not completely suppressed using SPAIR and affect the visualization of the organs.

Figure 6-4 shows the coronal images of a healthy volunteer obtained using SShTSE, SShTSE-SPAIR and SShTSE-mDixon. In the SShTSE-SPAIR image, incomplete fat suppression was often observed, especially at the edges of the FOV (Figure 6-4b, red arrows), because of the large B0 inhomogeneities. SPAIR also failed to suppress the visceral fat (Figure 6-4b, red dashed arrow), confounding the underlying anatomy. However, SShTSE-mDixon achieved robust fat-water separation (Figure 6-4c – 4e). Although the acquisition time of the SShTSE-mDixon was as same as the SShTSE-SPAIR, the SShTSE-mDixon generated the standard T2-W (Figure 6-4c) and fat-suppressed T2-W (Figure 6-4d) images simultaneously, therefore reducing the total scan time by half.

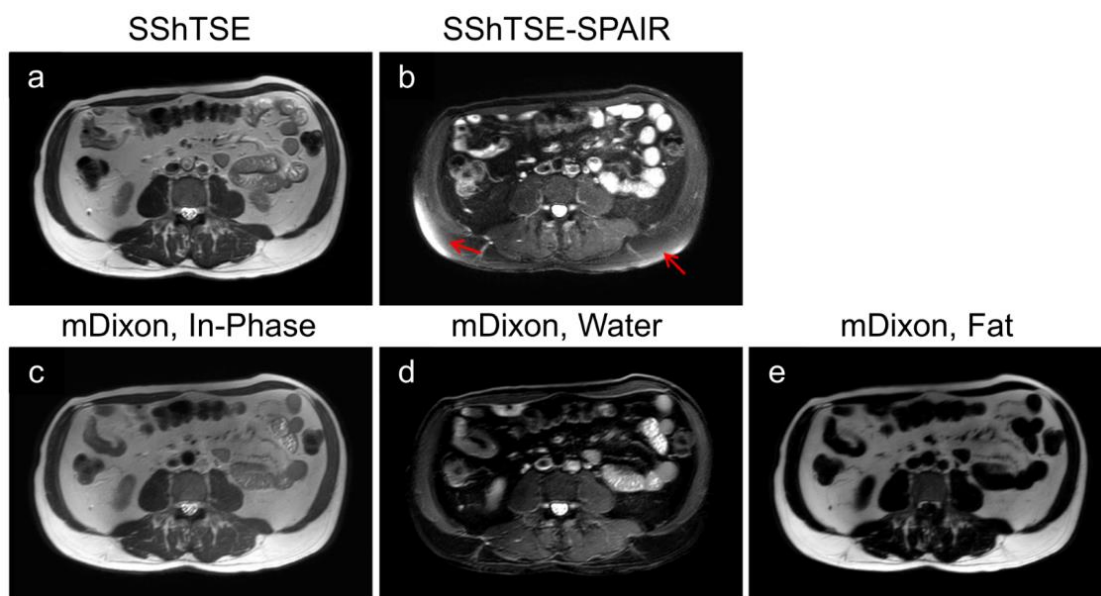


**Figure 6-5 Axial SShTSE images of a healthy volunteer acquired with/without fat suppression and dual-echo SShTSE-Dixon**

SShTSE images of a healthy volunteer acquired without (a) and with SPAIR (b). IP (c) image of the same location acquired using SShTSE with dual-echo Dixon, and the reconstructed water-only (d) and fat-only (e) images. Red arrows show incomplete fat suppression at the outside of the abdomen using SPAIR.

Figure 6-5 shows the axial images of another healthy volunteer acquired using SShTSE, SShTSE-SPAIR and SShTSE-mDixon. The subcutaneous fat was not completely suppressed using SPAIR especially in the slices close to the edges of FOV due to the B0 inhomogeneity (Figure 6-5b), while SShTSE-mDixon showed homogeneous fat-water separation (Figure 6-5c – 5e). SShTSE-mDixon achieved better subcutaneous and visceral fat suppression than SShTSE-SPAIR across all slices.

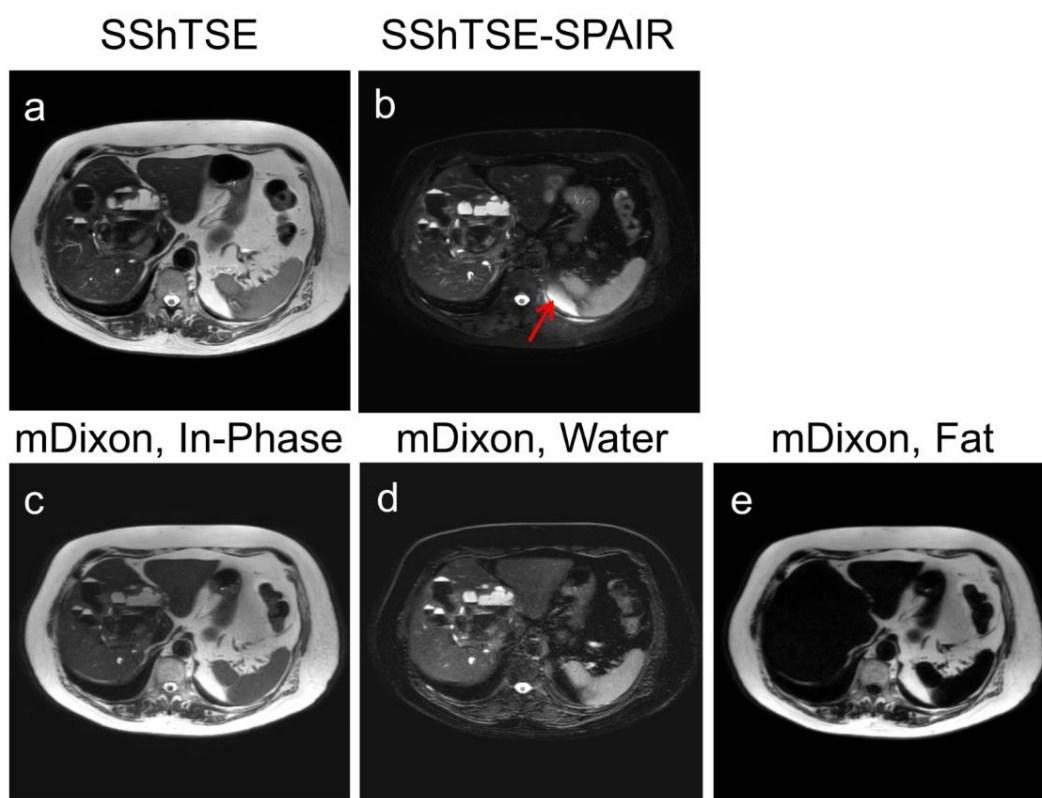


**Figure 6-6 Axial SShTSE images of a patient with liver tumors acquired with/without fat suppression and dual-echo SShTSE-Dixon**

SShTSE images of a patient acquired without (a) and with SPAIR (b). IP (c) image of the same location acquired using SShTSE with dual-echo Dixon, and the reconstructed water-only (d) and fat-only (e) images. Red arrows show incomplete fat suppression in the intra-abdominal cavity using SPAIR.

Figure 6-6 shows the SSHTSE, SSHTSE-SPAIR and SSHTSE-mDixon images of a patient with liver cancer. Unsuppressed visceral fat was observed in the SSHTSE-SPAIR image (Figure 6-6b). The unsuppressed visceral fat surrounding the spleen (Figure 6-6b, red arrow), mimicks the appearance of fluid. The SSHTSE-mDixon achieved homogeneous fat suppression (Figure 6-6d) and eliminated the confounding effect of unsuppressed fat.

**Table 6-2 Assessment of fat suppression: SPAIR vs. mDixon**

Category	Subcutaneous Fat	Visceral Fat
SPAIR (axial)	10/10	6/10
mDixon (axial)	1/10	0/10
SPAIR (coronal)	5/5	4/5
mDixon (coronal)	0/5	0/5

Numbers represent the number of cases in which the fat was not completely suppressed out of the total number of cases.

Table 6-2 summarizes the number of cases in which the fat was not completely suppressed. For the axial SSHTSE-SPAIR, the unsuppressed subcutaneous fat was primarily located in the slices close to the edge of FOV, and the unsuppressed visceral fat was around the spleen (3 cases), liver (2 cases) or stomach (1 case). Compared to SSHTSE-SPAIR, the axial SSHTSE-mDixon achieved significant improvement in the suppression of both subcutaneous and visceral fat ( $P = 0.004$  and  $P = 0.03$  respectively). The coronal SSHTSE-mDixon also showed better subcutaneous fat suppression than SSHTSE-SPAIR ( $P = 0.03$ ). The coronal SSHTSE-mDixon tend to provide better visceral fat suppression, but not statistically significant ( $P = 0.06$ ). There were no significant differences in CR between

water-only images and SShTSE-SPAIR images ( $P = 0.92$ ,  $2.6 \pm 0.4$  vs  $2.5 \pm 0.5$ ), as well as between IP images and SShTSE images ( $P = 0.84$ ,  $2.3 \pm 0.6$  vs  $2.2 \pm 0.4$ ). There were also no significant differences in the aSNRs of the liver and spleen between water-only and SShTSE-SPAIR images (Liver:  $P = 0.76$ ,  $12.2 \pm 4.9$  vs  $11.7 \pm 5.2$ ; Spleen:  $P = 0.14$ ,  $25.9 \pm 11.6$  vs  $23.7 \pm 9.7$ ), as well as between IP and SShTSE images (Liver:  $P = 0.60$ ,  $14.4 \pm 5.7$  vs  $13.4 \pm 5.0$ ; Spleen:  $P = 0.56$ ,  $26.5 \pm 10.1$  vs  $25.7 \pm 8.5$ ).

## 6.5 DISCUSSION

Fat-suppressed SShTSE is widely utilized in body MRI to improve the lesion conspicuity. SPAIR is the most commonly used fat suppression method in SShTSE because of high SNR, but it is sensitive to the  $B_0$  inhomogeneity and often suffers from incomplete fat suppression in areas with large  $B_0$  inhomogeneity (33). In this work, we have shown that the SShTSE sequence with multi-echo Dixon can improve fat suppression without increasing the scan time compared to SPAIR in breath-hold abdominal imaging at 3T, and the bi-directional homodyne reconstruction can reduce the zero-filling artifacts.

Multi-echo Dixon method based T2W sequences have been previously proposed to improve the fat suppression in abdominal imaging at 1.5T (54,112,113). Due to the large echo shift ( $\sim 2.2$  ms) at 1.5T, multi-echo Dixon increases the echo spacing as well as the echo time, resulting in blurring and low SNR. To counteract the large echo spacing, multi-shot TSE were used instead of SShTSE at the expense of long scan times and/or low spatial resolution. The echo shift of multi-echo Dixon is shorter ( $\sim 1.1$  ms) at 3T and reduces the echo spacing compared to 1.5T, making the SShTSE acquisition possible. However, the acquisition time will be limited by the short echo shift at 3T because of the limited receiver

bandwidth and slew rate. Although dual-echo Dixon imaging methods with flexible echo times have been proposed (40,42,44), a larger echo shift will increase the echo spacing and result in blurring. By contrast, partial echo acquisition can efficiently reduce the acquisition time to achieve a short echo shift by reducing the number of sampling points. The zero-filling artifacts along phase- and frequency-encoding directions were simultaneously reduced with the bi-directional homodyne reconstruction. Other reconstruction methods (116,117) can also be used to reduce the zero-filling artifacts, but the comparison and the evaluation of the effect on water-fat separation are beyond the scope of this study.

Multi-echo Dixon used higher receiver bandwidth compared to SPAIR, but the dual echo combination compensated the signal loss due to higher receiver bandwidth (118). In addition to the half scan, the partial echo acquisition also reduced the SNR slightly. Since the SNR is proportional to  $\sqrt{N}$ , a partial echo factor of 0.8 results in <10% signal loss. However, the acquisition of IP and OP echoes slightly compensated and probably provided higher SNR or reduced noise variation measured in water-only images. Furthermore, this can also probably be attributed to the smooth filters applied in water-fat separation.

SShTSE images are often acquired both with and without fat suppression in clinical protocols for complete evaluation. SShTSE with multi-echo Dixon can simultaneously generate co-registered fat-suppressed and non-fat-suppressed T2W images, eliminating the necessity of a separate T2W SShTSE scan and reducing the scan time. Compared to the standard SShTSE, multi-echo Dixon at 3T still increases the echo spacing resulting in minor blurring (e.g. Fig. 6-6d). SShTSE with variable refocusing flip angles (119) can be incorporated to reduce this blurring in future studies.

There are several limitations to this study. First, the subject number is small, and the clinical impact is not assessed. Second, aSNR was used to assess the in-vivo SNR instead of the direct SNR measurement because of SENSE. The signal variation of background tissues may bias the aSNR measurement. Third, the image quality was only assessed for fat suppression, SNR and CR. The sharpness of the image, motion-related artifacts and lesion detection are not evaluated, which can be done in the future clinical study with a large patient population.

In conclusion, we implemented a multi-echo Dixon based SSHTSE sequence for breath hold abdominal imaging at 3 T. It has been demonstrated that this approach significantly improves the fat suppression without increasing the scan time.

## CHAPTER SEVEN

### Whole-Body MRI for Metastatic Cancer Detection using T2-Weighted Imaging with Fat and Fluid Suppression

#### 7.1 OVERVIEW

The majority of this work was published in *Magnetic Resonance in Medicine* (2018). Portions of this work were presented at the joint annual meeting ISMRM-ESMRMB in Paris (June 2018).

#### 7.2 INTRODUCTION

Whole-body imaging using conventional techniques such as positron emission tomography combined with computed tomography (PET/CT) is routinely used clinically for whole-body cancer detection (120). A major concern with these techniques is the exposure to ionizing radiation (121-123), particularly in younger patients who need repeated exposures during long follow-up periods and staging in patients during post-treatment. Additionally, the spatial resolution of PET is limited and some tumors do not demonstrate uptake consistently with conventional radiotracers resulting in very low sensitivities reported for a variety of tumors, particularly when lesions are of smaller size (<1 cm) (124,125). Moreover, while these limitations may be partially compensated with contrast-enhanced computed tomography (CT) examinations, this leads to additional radiation exposure. Furthermore, repeated administrations of nephrotoxic iodinated contrast agents with CT is undesirable in patients with impaired renal function (126), a common occurrence in patients with metastatic disease.

In the past decade, whole-body magnetic resonance imaging (WB-MRI) has become a valuable alternative technique due to its excellent soft tissue contrast combined with high

spatial resolution and the lack of ionizing radiation (127). WB-MRI, particularly using echo-planar based diffusion-weighted imaging (DW-EPI), and diffusion weighted imaging with background suppression (DWIBS) have shown improved sensitivity and specificity for metastatic cancer detection at 1.5 T (128). DWI offers increased conspicuity for lesions with restricted diffusion (e.g. high cellularity) by suppressing the confounding tissue signals such as fat and fluid (129,130). However, DWI techniques that rely on EPI sequences suffer from geometric distortions due to large  $B_0$  inhomogeneities, particularly using large field-of-view (FOV). Moreover, DWI is inherently signal-to-noise ratio (SNR) limited. Consequently, DWI acquisitions require reduced spatial resolution, multiple signal averages, or both, which results in an increase of the total scan time (129). While the inherent low SNR can be partly mitigated by performing WB-MRI at 3T, larger  $B_0$  inhomogeneities at 3T compared to 1.5T lead to worse geometric distortions (21). Alternatively, WB-MRI using short tau inversion recovery (STIR) has been shown to provide increased tumor conspicuity with limited image distortion (131,132). However, STIR also suffers from reduced SNR due to non-selective inversion and requires multiple signal averages resulting in increased total scan times (19).

Most metastatic lesions tend to have longer T2 relaxivity compared to their surrounding non-neoplastic tissues and therefore appear brighter on T2-weighted (T2W) images. However, fat has relatively long T2 relaxivity and fluid has very long T2 relaxivity and therefore, both also appear bright on most clinical T2W images and need to be suppressed to improve lesion conspicuity (133,134). T2W images with fat suppression, either using STIR or chemically selective suppression such as spectral pre-saturation using (adiabatic) inversion recovery (SPIR/SPAIR) (33), can generate fat-suppressed T2W images,

but still carry fluid signal such as in cysts that often mimic lesions. Furthermore, STIR suffers from poor SNR, while SPIR/SPAIR suffers from inhomogeneous fat suppression particularly at 3T due to increased  $B_0$  inhomogeneities (19,21).

Thus, the purpose of this work was to develop a whole-body MRI technique at 3T with improved lesion conspicuity for metastatic cancer detection using fast, high-resolution and high SNR T2-weighted imaging with simultaneous fat and fluid suppression.

## **7.3 THEORY**

### **7.3.1 Imaging Sequence**

The proposed imaging strategy is based on a single shot turbo spin echo (SShTSE), which is a routinely used T2W imaging sequence in the body due to its robustness, favorable SNR and minimal image distortion. SShTSE is often performed with fat suppression for improved lesion conspicuity, commonly using SPIR/SPAIR, due to its increased SNR compared to STIR. However, SPIR/SPAIR suffers from fat-suppression failures in areas with increased  $B_0$  inhomogeneities, particularly relevant at 3T. Moreover, when applied for whole-body imaging, the thoracic region is prone to fat-suppression failure due to increased  $B_0$  inhomogeneities. To overcome these challenges, we used a modified Dixon (mDixon) based SShTSE acquisition, which provided robust fat/water separation in the abdomen in a single acquisition (135). We combined this SShTSE-mDixon with a dual-echo acquisition to achieve fluid suppression. This sequence acquires two sets of images – one at a short echo time (TE) and the other at a long TE, following the same excitation. The non-neoplastic tissues with short T2 and the metastatic lesions with moderately prolonged T2 preferentially appear on the short TE image, while the fluids with very long T2 appear on both short and

long TE images. Thus, subtraction of the long TE from the short TE preferentially suppresses fluid signal (46) and improves tumor conspicuity (136). We refer to this technique as, **Dual Echo T2-weighted acquisition for Enhanced Conspicuity of Tumors (DETECT)**.

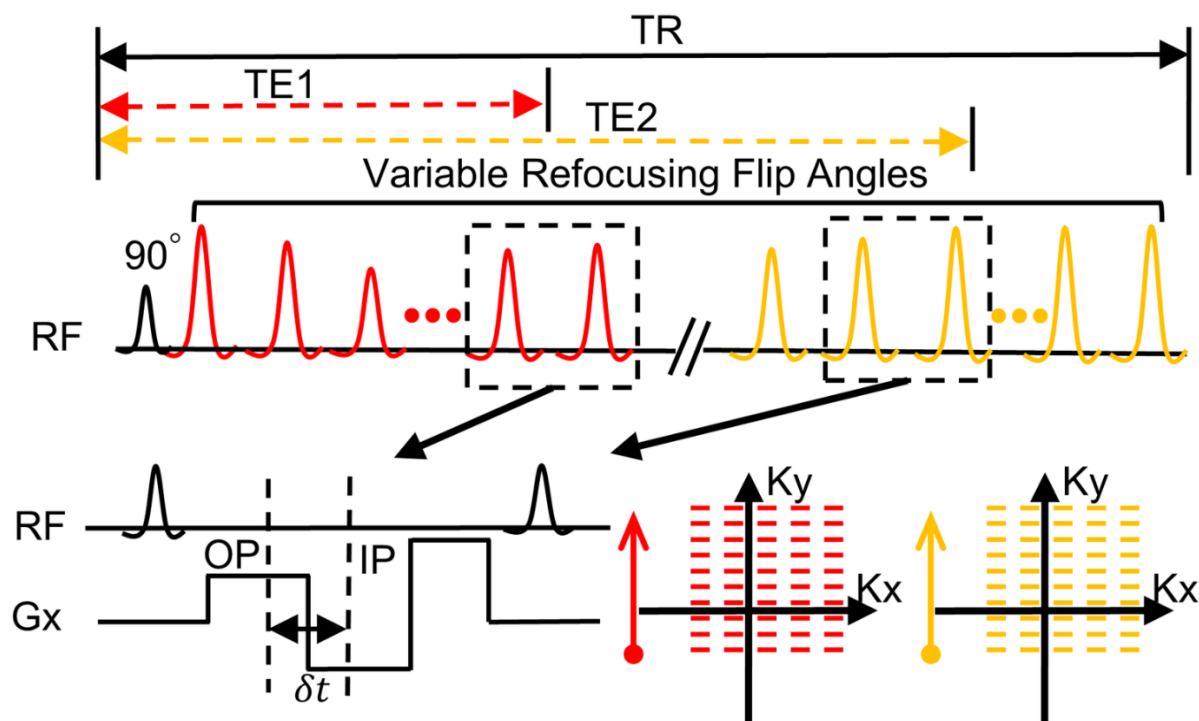


**Figure 7-1 Schematic of the Dual Echo T2-weighted acquisition for Enhanced Conspicuity of Tumors (DETECT) using single-shot turbo spin echo**

In each repetition, four images are acquired with variable refocusing flip angles, including out-of-phase (OP) and in-phase (IP) images at both short TE (TE1) and long TE (TE2). The IP and OP echoes are acquired using the bipolar readout gradients (Gx) with partial echo acquisitions between each pair of refocusing pulses, and at all refocusing pulses. After the readout gradients, arewinder gradient with large gradient strength is used to minimize the echo spacing.  $\delta t$  is the time difference between the OP and IP acquisitions (e.g. 1.1 ms at 3T). For both TEs, a linear view-ordering with partial phase encoding is used to sample the k-space.

Figure 7-1 illustrates a schematic of the DETECT imaging sequence. Following a single  $90^\circ$  excitation pulse, short TE (TE1, ~60-80 ms) images and long TE (TE2, ~400 ms) images are acquired in the same repetition using variable refocusing flip angles (119) and partial phase-encoding acquisitions using a SShTSE. Between each pair of refocusing pulses, in-phase (IP) and out-of-phase (OP) echoes are acquired for both TEs, at all refocusing pulses, using a bipolar readout for mDixon reconstruction. Partial-echo readouts are implemented to balance the in-plane resolution and receiver bandwidth (RBW), while maintaining the optimal time interval ( $\delta t$ ) of ~1.1 ms at 3T between IP and OP echoes for robust fat/water separation (57,135). An echo train length (ETL) of ~130 was used for both TEs, with 65 k-space lines for each TE. The RBW of the DETECT sequence was doubled to ~870 Hz/pixel, compared to ~440 Hz/pixel for the standard SShTSE. However, the reconstruction of water-only images using signal averaging of both IP/OP echoes generated comparable images to the standard SShTSE (135). Overall, four images are acquired with both partial phase-encoding and partial readout in a single repetition, including IP and OP images at both short and long TEs using DETECT.

### **7.3.2 Image Reconstruction**

#### *7.3.2.1 Fat suppression*

A phase-preserved homodyne reconstruction was used to reconstruct the IP and OP images at both TEs, with zero-filling along the frequency-encoding direction and homodyne filtering along the phase-encoding direction (57,135). This facilitated the reconstruction of complex IP and OP images, which allowed standard mDixon reconstruction for fat/water separation (40). While this approach provided robust fat/water separated images at short TE,

the fat/water separation failed at long TE due to the reduced SNR. To overcome this problem, a shared-field-map mDixon reconstruction was used, in which the  $B_0$  map estimated at the short TE was used for fat/water separation at the long TE. Considering that the  $B_0$  map changes slowly and all images are acquired within the same repetition, this shared-field-map mDixon reconstruction generates robust fat/water separation at the long TE (137). The standard mDixon reconstruction for the short TE images was performed on the scanner including the generation of the low-pass filtered  $B_0$  map. The shared-field-map mDixon reconstruction using this low-pass filtered  $B_0$  map for the long TE images was implemented in Matlab (Mathworks, Natick, MA).

### 7.3.2.2 Fluid Attenuation

The water-only images reconstructed at the short TE ( $W_{TE1}$ ) and the long TE ( $W_{TE2}$ ) represent T2-weighted and heavily T2-weighted images respectively, with uniform fat suppression. Given that the tissues with very long T2 (e.g. CSF and gallbladder) appear hyperintense on both short and long TE images, a subtraction between these two images was performed to achieve fluid attenuation. Specifically, a complex subtraction, enabled by the phase-preserved homodyne reconstruction, including a scaling factor ( $f$ ) was used to perform fluid attenuation (Equation 7.1).

$$W_{sub} = \text{Real}[(W_{TE1} - f \times W_{TE2})e^{-i\psi_1}] \quad \text{Equation 7.1}$$

where  $\psi_1$  is the phase of the  $W_{TE1}$  image and  $W_{sub}$  is the final subtracted water-only image with fat and fluid suppression. The scaling factor,  $f$ , was calculated using the following steps: First, the pixels that had signal intensities greater than 80% of the maximum signal intensity on the  $W_{TE2}$  image were selected. Next, the same pixels on the  $W_{TE1}$  image were identified.

Finally,  $f$  was calculated as the mean value of the ratio of these pixels, i.e.  $f = \text{mean}(I_1/I_2)$ , where  $I_1$  and  $I_2$  are the signal intensities of the reference pixels in  $W_{TE1}$  and  $W_{TE2}$  respectively. This scaling factor compensated the T2 decay of tissues with long T2; however, it overcompensated for tissues with very long T2 (e.g. when  $\text{abs}(f \times W_{TE2}) > \text{abs}(W_{TE1})$ ). Thus, the demodulation of the phase,  $\psi_1$ , and the final real operation in equation 1 preserved the sign after the complex subtraction and rectified this overcompensation by resetting those pixel values to zero. The complex subtraction including the scaling factor calculation and phase demodulation was implemented in Matlab. A flowchart showing the DETECT reconstruction including fat and fluid suppression is shown in Figure 7-2.

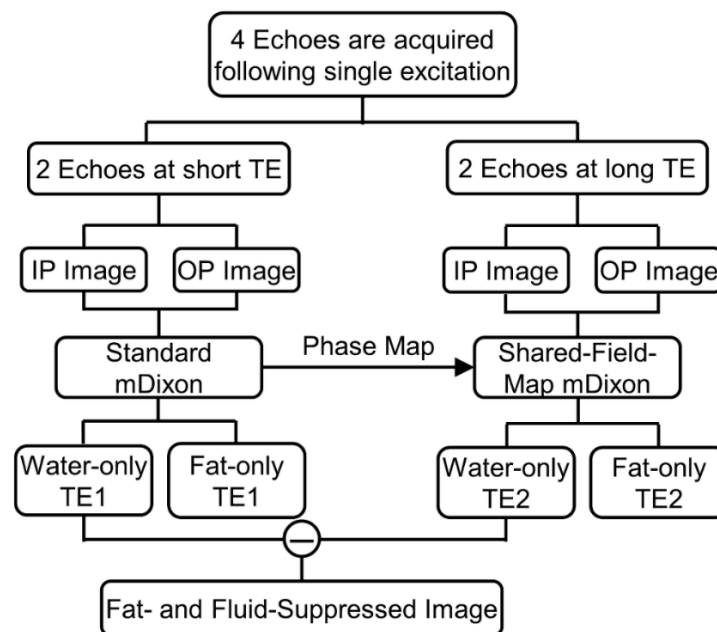


**Figure 7-2 Flowchart of the image reconstruction for DETECT**

The phase map, which is estimated using the standard mDixon with OP and IP images at short TE (TE1), is reused for fat/water separation at long TE (TE2) using the proposed shared-filed-map mDixon reconstruction. The water-only images at TE1 and TE2 are then subtracted to generate the final fat- and fluid-suppressed image.

### 7.3.2.3 Simulations

The choice of the TEs determines the signal difference that can be achieved on the  $W_{\text{sub}}$  image to enhance the conspicuity of the tumors, while simultaneously suppressing the fluids. Several factors of a SShTSE acquisition determine the TE, including view-ordering, echo spacing, FOV, partial phase-encoding factor and refocusing flip angle scheme. In this study, we chose linear view-ordering and variable refocusing flip angle schemes (119) for both TEs, to match clinically used SShTSE acquisitions at short TE (i.e. TE1=60-80 ms) for T2-weighted imaging of the abdomen, while also reducing the total SAR. The variable refocusing flip angle scheme was defined by the minimum, and maximum refocusing flip angles ( $\alpha_{\text{min}}$ ,  $\alpha_{\text{max}}$ ), used to sample the beginning and end of the echo train respectively, along with the middle refocusing flip angle ( $\alpha_{\text{mid}}$ ) used to sample the center of the k-space for short TE (138). The  $\delta t$  of about 1.1 ms, combined with receiver bandwidth and in-plane resolution forced the minimum echo spacing to be about 6.6 ms. Thus, the effective echo time ( $TE_{\text{eff}}$ ), defined as the TE when the center of k-space was sampled, and the equivalent echo time ( $TE_{\text{equiv}}$ ), defined as the TE that generates similar contrast as standard T2W image, were determined by the variable refocusing flip angle scheme in combination with the partial phase-encoding factor.

Bloch equation simulations were performed to investigate the influence of variable refocusing flip angle scheme and the partial phase-encoding factor on the signal difference to determine the optimal TEs. First, the partial phase-encoding factor was fixed at 0.6, similar to the standard clinical SShTSE acquisition, along with  $\alpha_{\text{min}}$  at  $90^\circ$  and  $\alpha_{\text{max}}$  at  $180^\circ$ , while the  $\alpha_{\text{mid}}$  was varied from  $100^\circ$  to  $160^\circ$  at  $20^\circ$  increments. This achieved the following TE values:

TE1 = 60 ms and TE2 = 450 ms. Next, the partial phase-encoding factor was varied between 0.6 and 0.7 (which also varied the TE1 and TE2 times), with the  $\alpha_{\min}$ ,  $\alpha_{\text{mid}}$ , and  $\alpha_{\max}$  fixed at 90°, 100°, and 120° respectively. These flip angles were chosen to achieve clinically equivalent TE, while reducing the total SAR (139) and sensitivity to motion (57). The other simulations parameters were: FOV = 520 mm (phase-encoding direction), voxel size = 1.8 mm, SENSE = 3, echo spacing = 6.6 ms. Signal evolution was calculated for a variety of tissues with the following T<sub>1</sub> and T<sub>2</sub> values at 3T (11,12,27,140): gray matter, T<sub>1</sub>/T<sub>2</sub> = 1820/99 ms; white matter, T<sub>1</sub>/T<sub>2</sub> = 1084/69 ms; liver, T<sub>1</sub>/T<sub>2</sub> = 812/42 ms; kidney, T<sub>1</sub>/T<sub>2</sub> = 1194/56 ms; fat, T<sub>1</sub>/T<sub>2</sub> = 371/133 ms; synovial fluid, T<sub>1</sub>/T<sub>2</sub> = 3620/767 ms; CSF, T<sub>1</sub>/T<sub>2</sub> = 4500/2500 ms; and a generic tumor model with T<sub>1</sub>/T<sub>2</sub> = 1000/150 ms. The signal differences between the two TEs were plotted against a range of T<sub>2</sub> values.

## 7.4 METHODS

### 7.4.1 Imaging Studies

All imaging was performed on a 3T MR scanner (Ingenia, Philips Healthcare, Best, The Netherlands). The DETECT was evaluated in 6 healthy volunteers, first in a dedicated abdominal imaging session of a healthy volunteer, followed by whole-body imaging protocol in 5 healthy volunteers. Subsequently, 5 patients with known metastatic renal cell carcinoma (mRCC) were enrolled for whole-body imaging evaluation of the DETECT sequence. The study protocol was approved by the institutional review board (IRB), Health Insurance Portability and Accountability Act (HIPAA)-compliant and all subjects provided written informed consent prior to their participation in the study.

### 7.4.2 Abdominal Imaging

To evaluate the shared-field-map mDixon reconstruction, one 40-year old healthy female volunteer was enrolled for abdominal imaging. The acquisition parameters for the DETECT sequence were: coronal orientation; FOV =  $400 \times 400 \text{ mm}^2$ ; slice thickness/slice gap = 4 mm/0 mm; voxel size =  $1.5 \times 2 \text{ mm}^2$ ; SENSE = 3; echo spacing = 6.2 ms;  $TE1_{\text{eff}}/TE2_{\text{eff}} = 69/340 \text{ ms}$ ;  $TE_{\text{equiv}1}/TE_{\text{equiv}2} = 62/297 \text{ ms}$ ; TR = 1250 ms;  $\delta t = 1.1 \text{ ms}$ ; ETL = 130 for both TEs with 65 k-space lines for each TE; RBW =  $\sim 870 \text{ Hz/pixel}$ ; partial phase-encoding factor = 0.65 and partial readout factor = 0.7. A total of 42 slices were acquired with 14 slices each in a 16-second breathhold acquisition. A 16-channel phased-array anterior coil along with the 12-channel phased-array posterior coil, embedded in the table, was used for signal reception.

### 7.4.3 Whole-Body Imaging of Normal Volunteers

**Table 7-1 Parameters of the whole body MRI sequences**

Sequence	Parameter		TR/TE (ms)	Scan Time (min/ station)	Total Scan Time <sup>a</sup> (min)
	FOV (cm <sup>2</sup> ) Read-Phase	Voxel Size (mm <sup>3</sup> ) Read-Phase-Slice			
DETECT (Coronal)	30×30 (head) 32×52 (body)	1.2×1.2×5 (head) 1.3×1.8×5 (body)	1250/ 70 (TE1), 450 (TE2)	1:01	7:00
DWIBS (Coronal)	30×30 (head) 32×52 (body)	3.5×3.5×5	12000/70	3:09 (head) 3:20 (body)	16:29
DWIBS (Axial)	30×30 (head) 32×52 (body)	3.5×3.5×5	12000/70	3:09 (head) 5:15 (body)	24:09

<sup>a</sup>Included breathhold instructions for thoracic and abdomen scans for DETECT, STIR, SPAIR and SShTSE.

Five healthy volunteers (3 females, 2 males, age range: 24 – 61 years), including 2 volunteers for optimization and 3 volunteers for evaluation of whole-body DETECT imaging were enrolled. The three healthy volunteers were scanned in 5 stations (head, thorax, abdomen, pelvis, and thighs) to cover the whole body from the head to the knees. All images were acquired in the coronal plane at an acquisition time of about 1 minute per station for approximately 50 slices. The thoracic and abdominal regions were acquired in four, 15-second breathheld acquisitions each, which increased the scan time to about 2 minutes for each of these stations, including the breathhold instructions. A SENSE acceleration factor of 3, partial phase-encoding factor of 0.6, partial readout factor of 0.85, ETL of 130 for both TEs with 65 k-space lines for each TE, RBW of 870 Hz/pixel and  $\delta t$  of 1.1 ms were used. All images were acquired contiguous with no slice gap. The remaining acquisition parameters are listed in Table 7-1. The total scan time of whole-body DETECT imaging was approximately 7 minutes including the breathhold instructions.

For the most time-efficient imaging of larger FOV, coronal plane acquisitions are often preferred. However, DWIBS images are prone to increased image distortion due to gradient non-linearities in the coronal plane compared to the axial plane. Hence, DWIBS images are commonly acquired in the axial plane to minimize image distortions, but at the expense of increased acquisition times. To evaluate the image quality and acquisition efficiency, one healthy volunteer was scanned with whole-body DWIBS in both axial and coronal planes, compared to whole-body DETECT in the coronal plane. The scan parameters are listed in Table 7-1.

#### 7.4.4 Whole-Body Imaging of Patients

Five patients (1 female, age: 58 years; and 4 males, age: 52 – 68 years) with known mRCC on prior clinical imaging, were scanned to evaluate the performance of DETECT for metastatic cancer detection. The whole-body MRI protocol included DETECT compared against DWIBS using 5 stations in the coronal plane. The acquisition parameters were similar to the above volunteer studies, except for the FOV along the anterior-posterior direction which varied among subjects between 300-400 mm for complete coverage of the body. To improve the visualization of the metastatic lesions and suppress the signals from complex fluids in the abdomen and bowel, an effective T2 map was generated using the two TE images (Equation 7.2), with a threshold of 300 ms. This map effectively suppressed the signals from the complex fluid with moderate T2 values (~300 ms), which were longer than that of the metastatic lesions (~160 ms), but were not long enough to be visible on the long TE image ( $TE2_{equiv} = \sim 400$  ms) and therefore, were not suppressed on the DETECT image. Subsequently, a T2map-weighted subtracted image (Equation 7.3) was generated to improve the conspicuity and localization of the lesions.

$$T2_{eff} = (TE2_{eff} - TE1_{eff}) / \log\left(\frac{W_{TE1}}{W_{TE2}}\right) \quad \text{Equation 7.2}$$

$$I_{T2w} = T2_{eff} \times W_{sub} \quad \text{Equation 7.3}$$

where  $TE1_{eff}$  and  $TE2_{eff}$  are the effective TEs.

### 7.4.5 Image Evaluation

In all 8 whole-body subjects, including 3 healthy volunteers and 5 mRCC patients, the signal reduction of long T2 tissues such as fluids on the DETECT sequence was measured compared to the short TE image, as described before (136). Additionally, the number of lesions identified on the proposed DETECT sequence compared to DWIBS was assessed in consensus by three board-certified radiologists with different levels of expertise in body MRI (A.P, fellow; N.M.R, 25 years and I.P, 16 years).

## 7.5 RESULTS

### 7.5.1 Simulations

Figure 7-3 shows the simulated signal differences between the two TEs of the DETECT with varying refocusing flip angles (Figure 7-3a) and partial phase-encoding factors (Figure 7-3b). The signal difference for tissues of interest with T2 less than ~160 ms increases with larger  $\alpha_{\text{mid}}$  (Figure 7-3a), but at the expense of increased SAR. The increasing partial phase-encoding factor also increases the relative signal difference for tissues with longer T2 (e.g. 200 ms vs. 150 ms) since it prolongs the  $\text{TE}_{\text{eff}}$  for both TEs (Figure 7-3b), but at the expense of reduced SNR.

The majority of the tissues in the body (except for fat and fluid) have T2 less than 100 ms at 3T (11), while the tumors tend to have moderately prolonged T2 but still typically less than 200 ms (141). Thus, an  $\alpha_{\text{mid}}$  of  $100^\circ$  and partial phase-encoding factor of 0.6 were chosen to retain the T2 contrast of the normal tissues with T2 less than 100 ms on the subtracted DETECT, while maximizing the signal difference for tissues with targeted T2 values around 150 ms (Figure 7-3c). This combination, along with  $\alpha_{\text{min}}$  of  $90^\circ$  and  $\alpha_{\text{max}}$  of

120°, provided a  $TE_{\text{eff}}$  of 70 ms for the first TE, matching the clinical whole-body T2W imaging protocol and a  $TE_{\text{eff}}$  of 450 ms for the second TE, with low SAR ( $\sim 2.2$  W/kg) and reduced sensitivity to motion (119). The simulated signal evolutions of the tissues of interest are shown in Figure 7-3d. As expected, the fat and fluid appear bright on T2-weighted images and when suppressed using the DETECT, improve the visualization and conspicuity of the tumors.

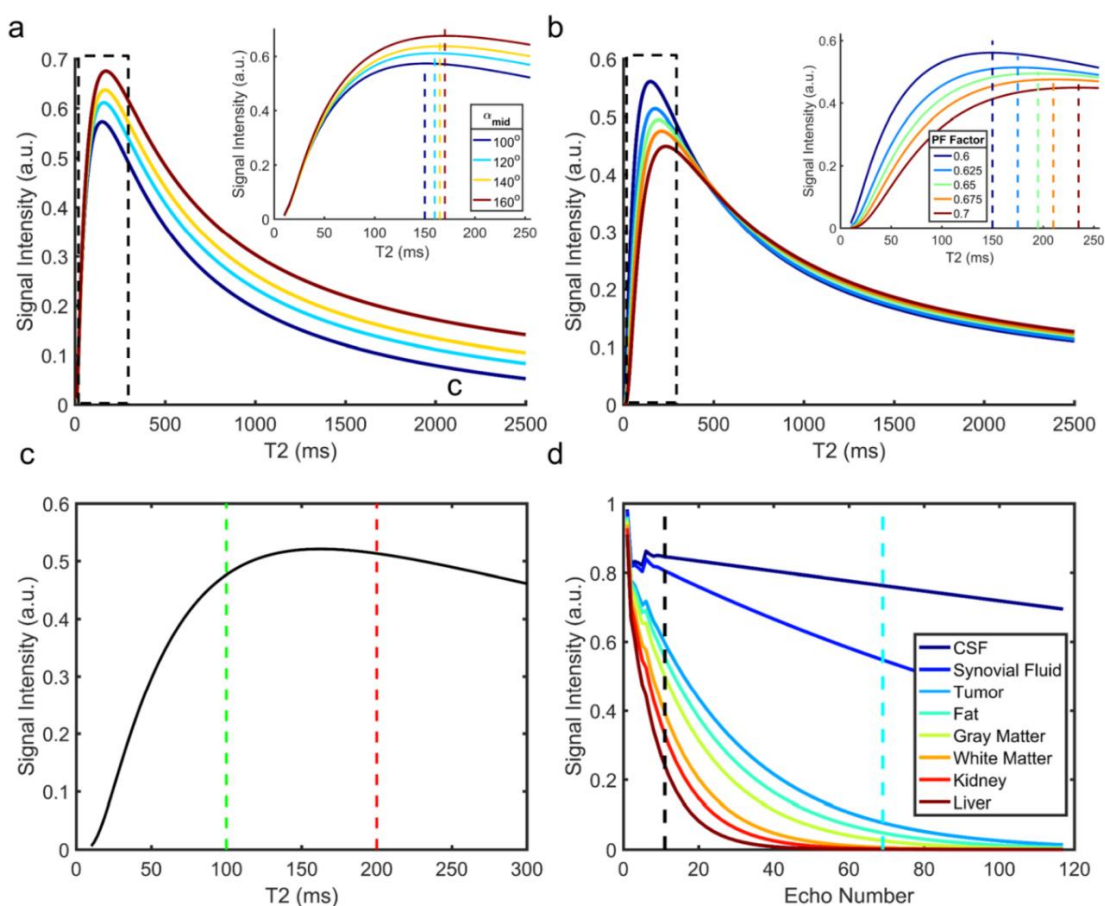


**Figure 7-3 Simulated signals of DETECT sequence**

Simulated signal differences between the two different TEs against varying T2 for different refocusing flip angle schemes (a) and partial phase encoding factors (b). The simulation parameters are described in Theory. The maximum signal differences (dashed vertical color

lines in insets) shift to longer T2 with the increase of either  $\alpha_{\text{mid}}$  (a) or partial phase encoding factor (b). A refocusing flip angle train of  $90^\circ$  ( $\alpha_{\text{min}}$ ) –  $100^\circ$  ( $\alpha_{\text{mid}}$ ) –  $120^\circ$  ( $\alpha_{\text{max}}$ ) shows maximum signal difference for tissues with T2 values between 100 and 200 ms (c). The signal behavior with this scheme shows that the signals from tissues with very long T2 (e.g. CSF and synovial fluid) along with fat appear bright compared to tumor, and need to be suppressed to improve lesion conspicuity (d).

### 7.5.2 Shared Field-Map mDixon Reconstruction

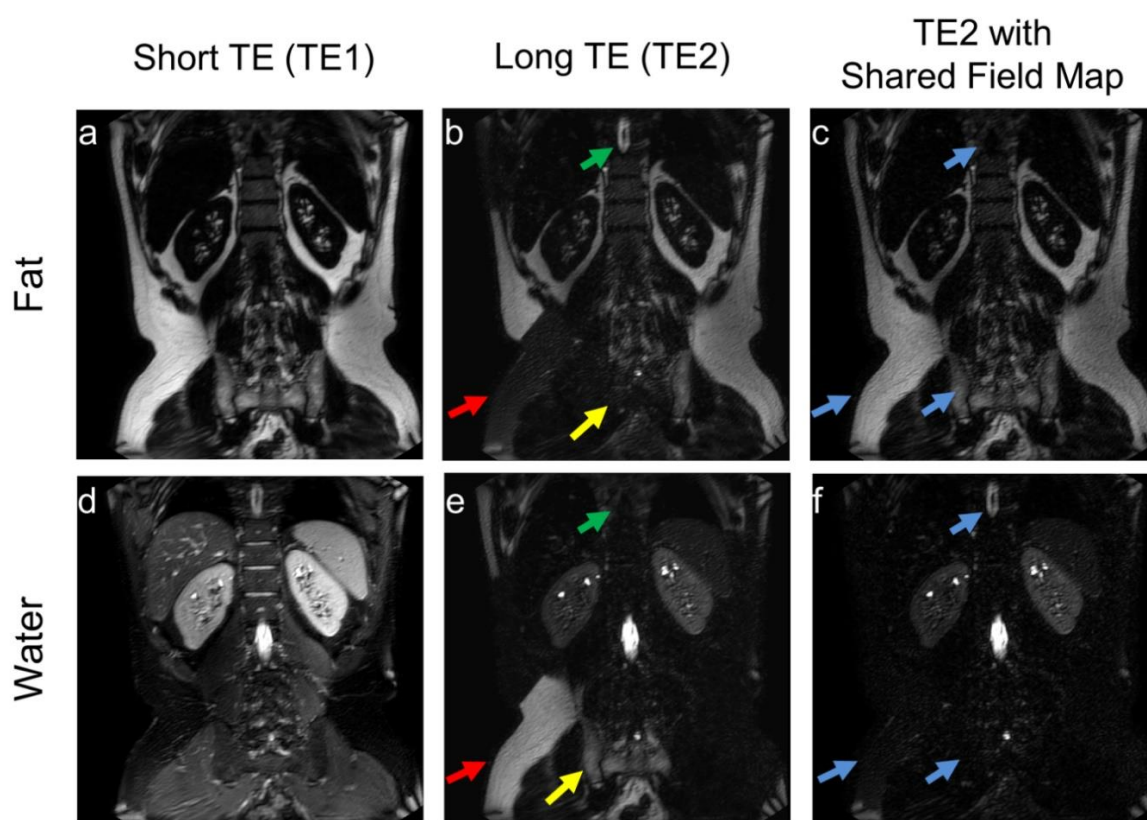


**Figure 7-4 Coronal images of a 47-year-old healthy female volunteer's abdomen**

Coronal images of a 47-year-old healthy female volunteer's abdomen showing robust fat/water separation using the standard mDixon reconstruction at the short TE (TE1, a, d), and failed fat/water separation at the long TE (TE2, b, e) involving multiple locations (e.g. the subcutaneous fat (red arrows), CSF (green arrow) and bone marrow (yellow arrow)). The

shared-field-map mDixon reconstruction (c, f) using the  $B_0$  field map from TE1 achieved successful fat/water separation at TE2, even with reduced SNR (blue arrows). Some residual FID artifacts were observed on the fat images due to stimulated echoes, which were subsequently minimized in the whole-body images using stronger crusher gradients.

Figure 7-4 shows the improved fat/water separation in the abdominal images of a 47-year old healthy female volunteer using the shared-field-map mDixon reconstruction. At the short TE (TE1), the standard mDixon reconstruction achieved robust fat/water separation throughout the imaging FOV, with minimum fat/water swaps at the edges of the large FOV (Figure 7-4a, 4d). However, the fat/water separation failed significantly with the standard mDixon reconstruction at the long TE (TE2, Figure 7-4b, 4e) due to the reduced SNR. The proposed shared-field-map mDixon reconstruction using the  $B_0$  map from the short TE achieved robust fat/water separation in the long TE images (Figure 7-4c, 4f).

### **7.5.3 Complex Subtraction**

The results of fluid attenuation, reconstructed with both the magnitude and complex subtraction are shown in Figure 7-5. The “dark-rim” artifacts, that are often observed around the edges of the tissues with relatively long T2 on magnitude subtraction, are the result of the modulation of the point spread function. Since the phase of the water signal is preserved with our phase-preserved homodyne and shared-field-map mDixon reconstruction, the complex subtraction eliminated these “dark-rim” artifacts and resulted in much smoother profiles.

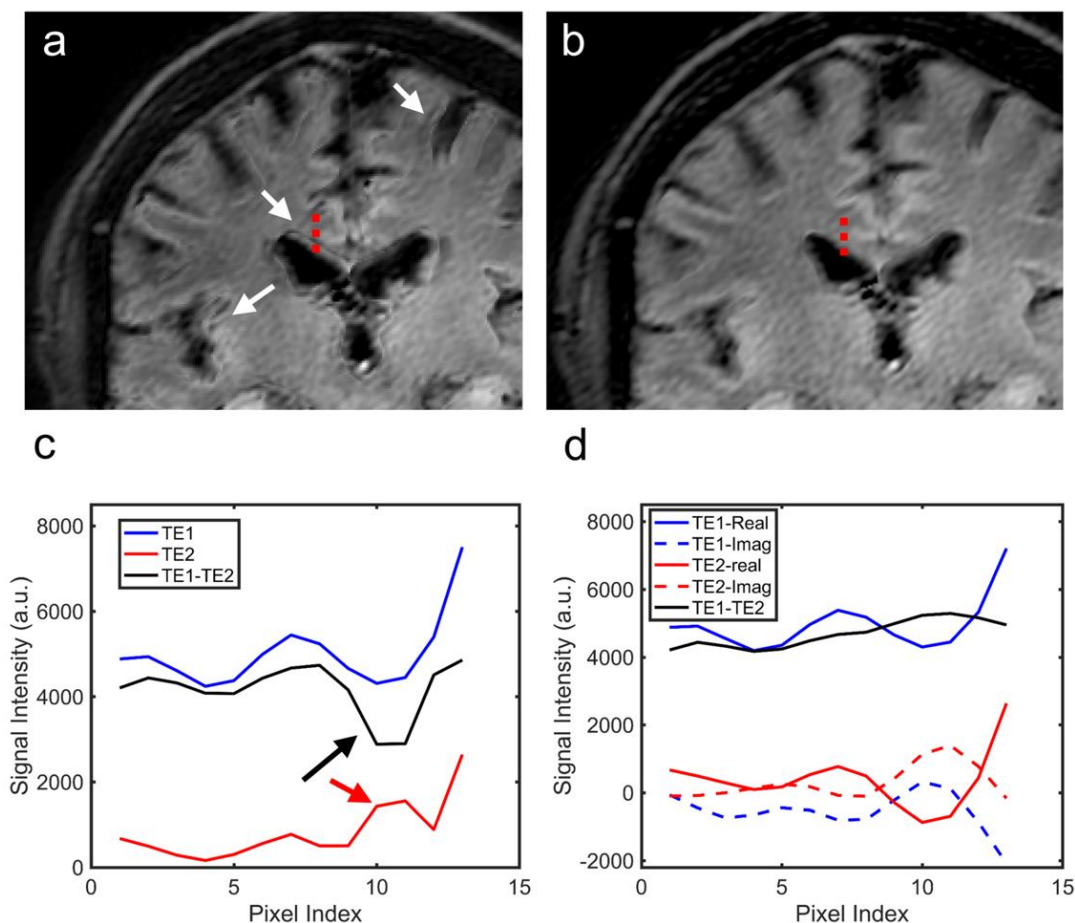


**Figure 7-5 Subtracted brain images comparing magnitude subtraction and complex subtraction**

Subtracted brain images of a 62-year-old healthy male volunteer showing “dark-rim” artifacts with magnitude subtraction (a, white arrows), which are eliminated with complex subtraction (b). In long TE images, the first side lobes of the point spread function of hyperintense tissues are often negative due to the heavy signal decay of the surrounding tissues. The magnitude operation converts these negative local minima into positive local maxima (red arrows, c), which manifest as local minima on magnitude-subtracted images (black arrow, c) and create “dark-rim” artifacts (white arrows, a). The signal profiles (c, d) corresponding to the dashed red lines in (a, b) show the local maxima of the magnitude profile on TE2 image (red arrow, c), that create the local minima on the magnitude subtracted profile (black arrow, c), and are rectified in complex subtraction (d).

### 7.5.4 Whole-Body Imaging of Normal Volunteers

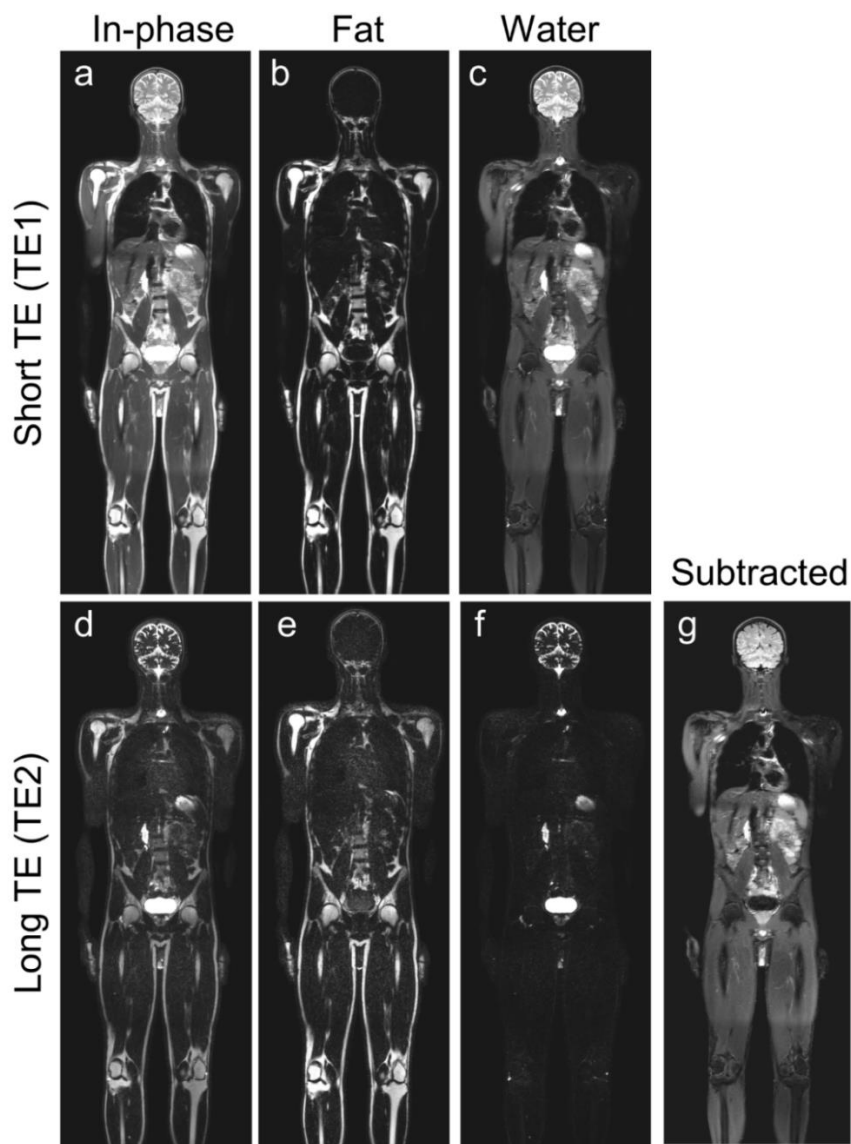


**Figure 7-6 Whole-body MR DETECT images of a healthy volunteer**

Whole-body MR DETECT images of a 28-year-old healthy male volunteer acquired in five stations in 7 minutes. The standard mDixon reconstruction demonstrates robust fat/water separation across the entire volume at the short TE (a-c), while the shared-field map mDixon reconstruction achieved uniform fat/water separation at long TE (d-f). The subtracted image (g) shows uniform fat and fluid suppression over the entire imaging volume and across all slices

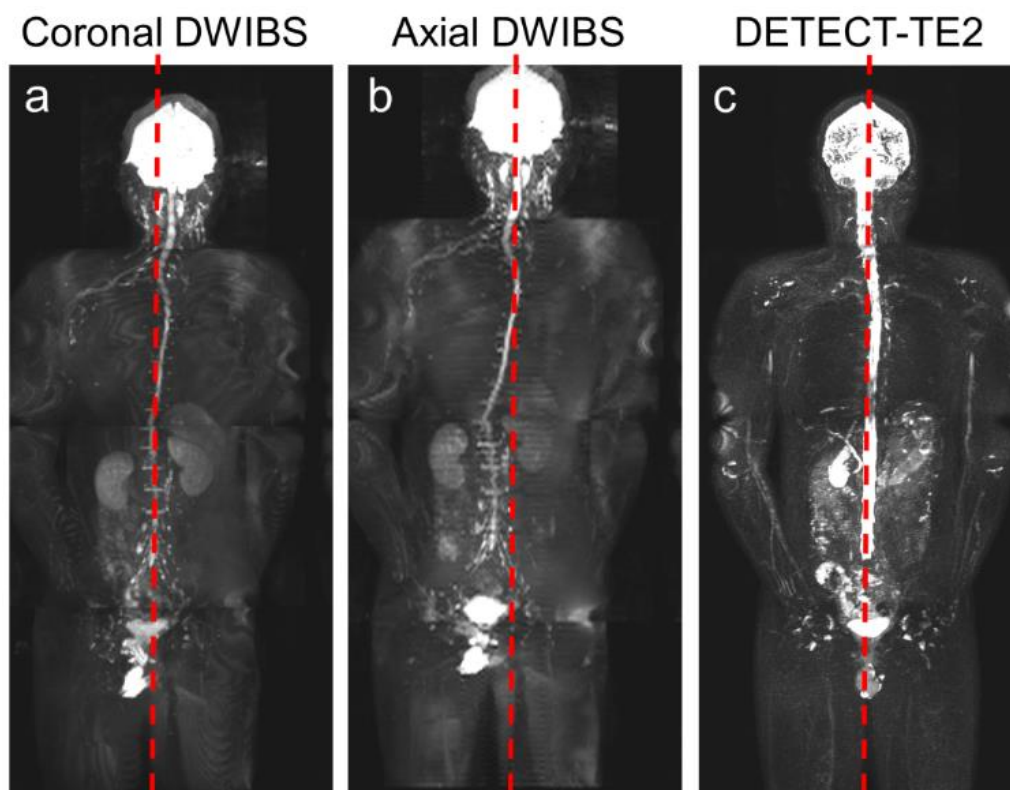


**Figure 7-7 Whole-body 3D MIP reconstructions of a healthy volunteer comparing DETECT and DWIBS regarding geometric distortions**

Whole-body 3D MIP reconstructions of a 34-year-old healthy male volunteer demonstrating increased robustness of DETECT to geometric distortions, compared to DWIBS. 3D MIP from coronal DWIBS at  $b = 800 \text{ s/mm}^2$  (a) and the coronal reformat from the axial acquisition of DWIBS at  $b=800 \text{ s/mm}^2$  (b) show distorted spinal cord from the midline of the image (red dashed line). 3D MIP of the long TE image from DETECT shows straight spinal canal compared to the midline (c).

The shared-field-map mDixon reconstruction and the complex subtraction achieved uniform fat and fluid suppression throughout the body (Figure 7-6) and across all slices. The whole-body images, acquired with DWIBS in both coronal and axial orientations and with DETECT in coronal orientation are shown in Figure 7-7. DWIBS images in the coronal

orientation suffer from large geometric distortions (Figure 7-7a). Although the coronal DWIBS images reformatted from the axial acquisitions (Figure 7-7b) also suffer from geometric distortions, the originally acquired axial images show less in-plane distortions (not shown). However, the scan times for axial DWIBS acquisitions are generally longer compared to the coronal acquisitions. In our example, the total scan time for the axial DWIBS acquisitions was 19 minutes compared to the 13 minutes for coronal DWIBS acquisitions for 4-station WB-MRI. Alternatively, the images acquired using DETECT exhibited minimal geometric distortions (Figure 7-7c) in a 6:00 minute coronal plane acquisition for 4-station WB-MRI, including breathhold instructions. DETECT images showed better quality with uniform fat and fluid suppression compared to DWIBS without geometric distortions and artifacts in the coronal plane over the entire volume.

### 7.5.5 Whole-Body Imaging of Patients

**Table 7-2 Number of lesions identified on WB-MRI with DETECT compared to WB-MRI with DWIBS in patients**

Patient No.	WB-MRI with DETECT Total (per station)	WB-MRI with DWIBS Total (per station)
1	1 (0/0/0/1/0)	1 (0/0/0/1/0)
2	8 (0/1/2/3/2)	7 (0/1/2/3/1)
3	3 (0/0/3/0/0)	2 (0/0/2/0/0)
4	40 (5/22/5/7/1)	27 (2/17/3/5/0)
5	3 (0/2/1/0/0)	- *

\*Unable to complete WB-MRI DWIBS in patient 5, due to significantly long scan time (~50 minutes)

The total number of lesions identified, including lesions per station, on the WB-MRI with DETECT compared to WB-MRI with DWIBS is summarized in Table 7-2. Overall, the

DETECT identified all metastatic lesions known on prior clinical imaging and several additional new lesions, that were not identified on DWIBS due to artifacts associated with severe geometric distortions. For example, both DETECT and DWIBS showed clear delineation of an RCC metastatic lesion in the left iliac bone (Figure 7-8), for which the patient was receiving radiation treatment. However, the localization of the lesion with respect to the background anatomy was challenging on the DWIBS image due to the geometric distortions. The subtracted DETECT image, however, retained the lesion signal while suppressing the signals from fat and fluids with long T2 (Figure 7-8b). The effective T2-map weighted image, generated with T2 values less than 300 ms, further increased the lesion conspicuity (Figure 7-8c). In another mRCC patient with multiple metastatic lesions and right femoral metal implant, DETECT showed improved visualization of the lesions, while the visualization was significantly compromised on the DWIBS images (Figure 7-9). Large metastases in the left lung are seen on both DWIBS and DETECT images (red, green arrows, Figure 7-9), while DWIBS images suffer from geometric distortions and poor lesion localization. However, the metastatic lesion in the right femur is not visualized on the DWIBS image (yellow circle, Figure 7-9a), while it is clearly identified on the DETECT images (yellow arrow, Figure 7-9b, 9c). The metastatic lesion was confirmed with clinical CT (Figure 7-9d) and bone scan (Figure 7-9e). Similar behavior was observed throughout the entire volume in this patient as well as in other patients (Table 2). Furthermore, the availability of other image contrasts including fat-only image and in-phase image, all acquired in the same sequence and perfectly co-registered, improved the localization of the lesions on DETECT (Figure 7-10).

Additionally, across all 8 whole-body subjects, including 3 healthy volunteers and 5 mRCC patients, the signal of long T2 tissues including, CSF, bile and urine were suppressed by  $98 \pm 2 \%$ ,  $89 \pm 11 \%$  and  $86 \pm 21 \%$  respectively.

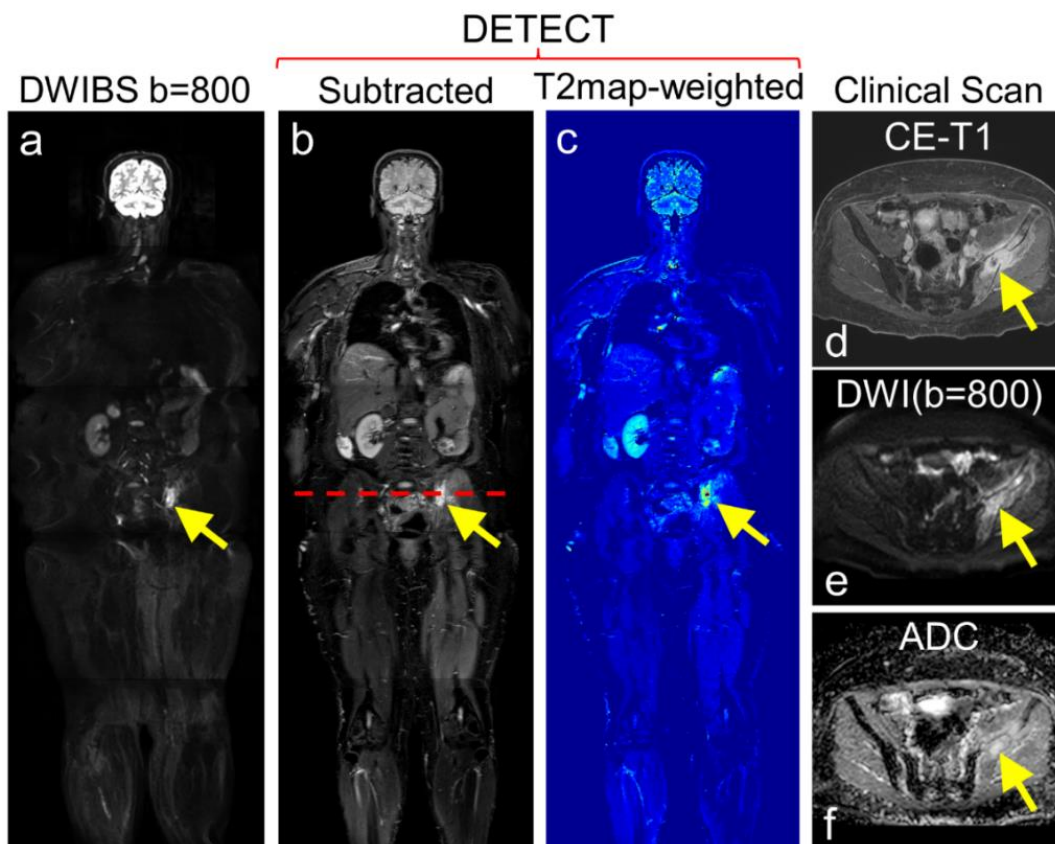


**Figure 7-8 Whole-body MRI of a 58-year old female patient volunteer with advanced renal cell carcinoma and underwent radiation treatment to the left iliac bone metastatic lesion**

DWIBS image at  $b=800 \text{ s/mm}^2$  (a), subtracted DETECT image (b) and the effective T2map-weighted image (c) show conspicuous lesion. Clinical contrast-enhanced fat saturated T1-weighted image of the same patient reveals an enhancing left iliac bone lesion (d, yellow arrow), which also appeared hyperintense on clinical DWI image with  $b = 800 \text{ s/mm}^2$  (e, yellow arrow), and ADC map (f) (calculated from 4 b-values; 0, 50, 400,  $800 \text{ s/mm}^2$ ), indicative of residual tumor with post-radiation effects.

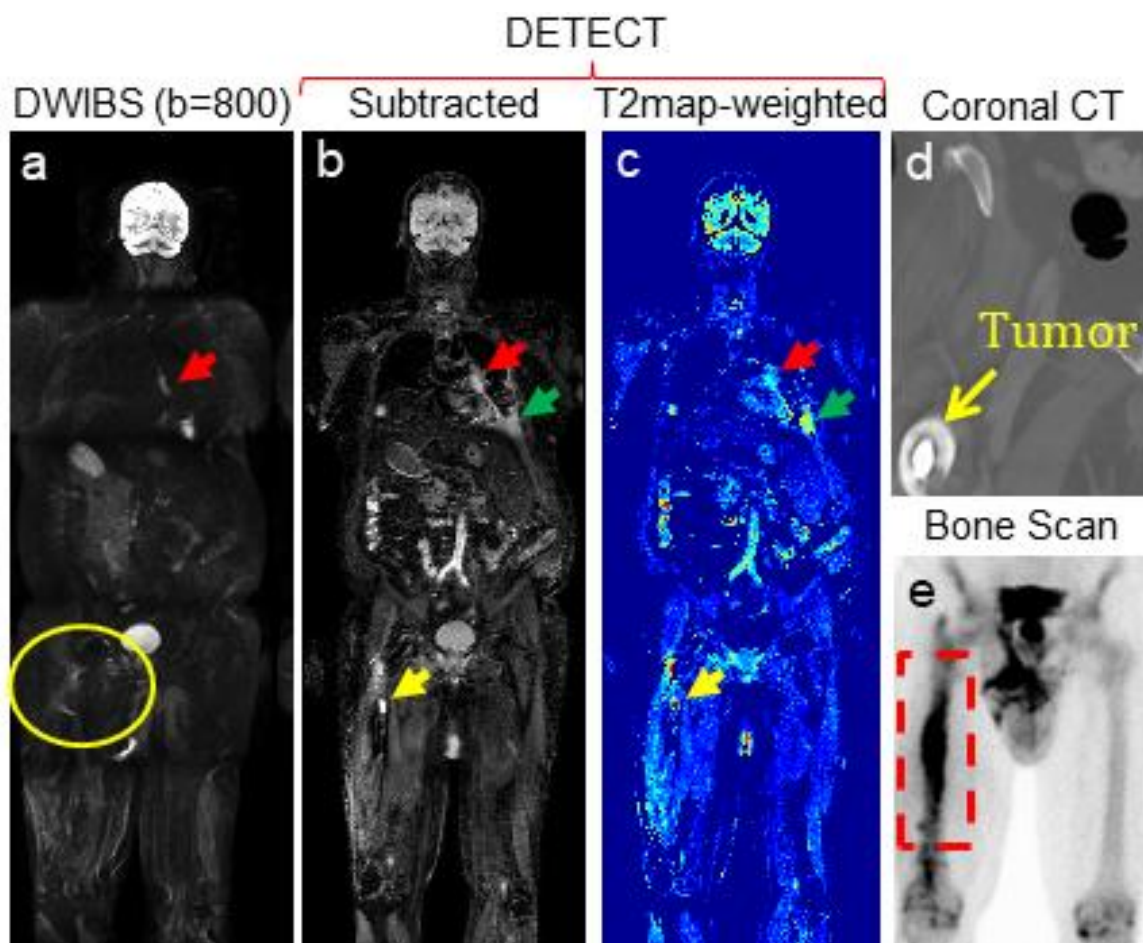


**Figure 7-9 Whole-body MRI of a 68-year old male patient volunteer with advanced renal cell carcinoma with a history of prophylactic rod placement and radiation treatment for a right femur metastatic lesion**

Coronal DWIBS image at  $b = 800 \text{ s/mm}^2$  (a), subtracted DETECT image (b), and T2-map weighted image (c) demonstrate metastatic disease involving the left hilum (red arrows) and the left 8<sup>th</sup> rib (green arrows). While a right femur lesion (yellow arrow) is clearly identified on the DETECT images (b, c yellow arrows), it is not visualized on the DWIBS images due to image distortion from the metallic implant (a, yellow circle). The lesion was clearly identified on the clinical CT (d), while the clinical bone scan (e) shows diffuse enhancement associated with metallic implant inflammation, without clear identification of the metastatic lesion.

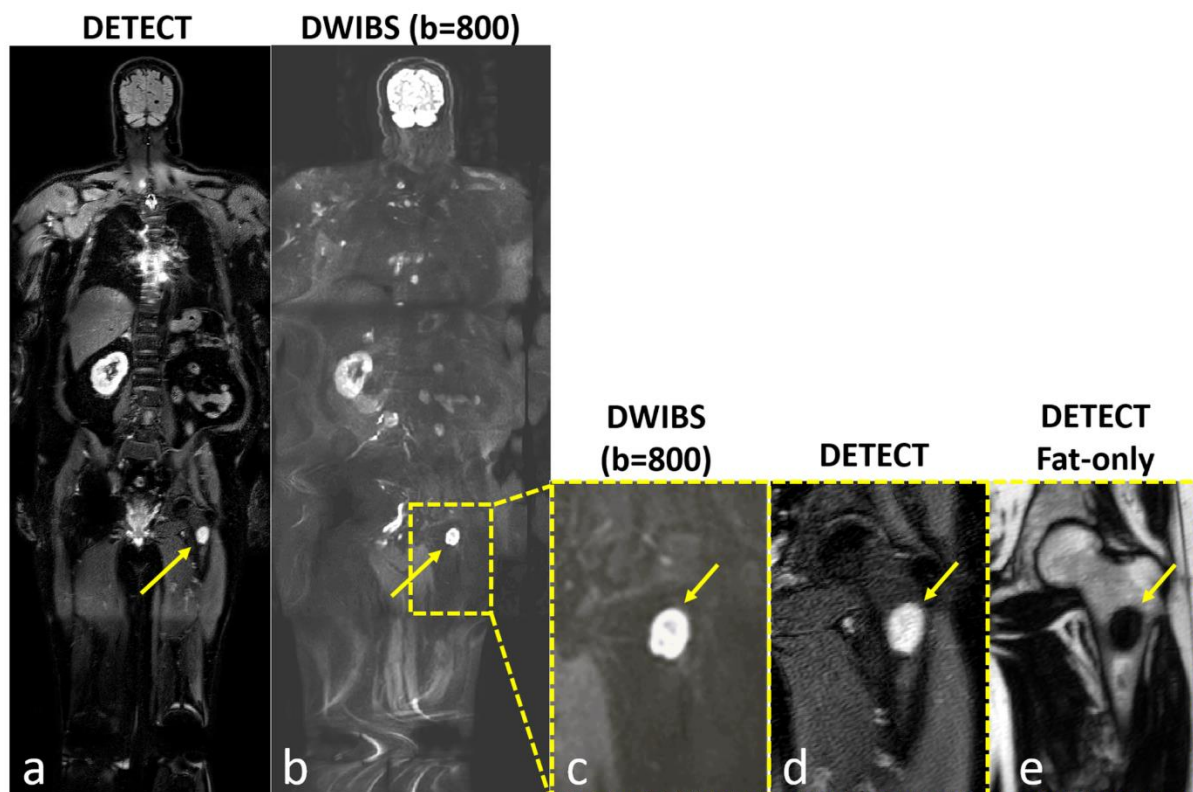


**Figure 7-10 Whole-body MRI of a 64-year old male patient volunteer with advanced renal cell carcinoma showing improved lesion localization capability of DETECT**

While both DETECT (a) and DWIBS (b) images show a left lower extremity lesion (arrows), the DWIBS image cannot localize the finding to bone, muscle or lymph node, even when zoomed in (c, arrow). However, DETECT clearly localizes the lesion within the left femur (a, d; arrows). (e) DETECT fat-only image, acquired in the same sequence, confirms the loss of normal marrow (arrow), increasing diagnostic confidence for both location and malignant nature of this lesion.

## 7.6 DISCUSSION

Whole-body MRI has emerged as a promising clinical option for noninvasive detection of metastatic cancer. The major goals of WB-MRI for cancer detection include, fast imaging, high spatial resolution, and high SNR while simultaneously suppressing the signals

from the background tissues to improve the conspicuity of the lesions. While the commonly used WB-MRI technique, DWIBS, provides improved conspicuity of the lesions, it often suffers from poor SNR, low spatial resolution and prolonged acquisition times (21,128,142). Additionally, DWIBS images suffer from geometric distortions, particularly at 3T, challenging the anatomical localization of the identified lesions. In this work, we have developed a dual-echo T2-weighted imaging technique for enhanced conspicuity of the tumors (DETECT), that generates fast, high-resolution, and high SNR images with simultaneous fat and fluid suppression, good tumor conspicuity and robustness of RF-refocused spin-echo acquisition in less than 7 minutes scan time for the whole-body imaging. Once the lesions are identified with the proposed DETECT technique, the lesions can be further characterized by dedicated functional MRI techniques such as diffusion, perfusion, hypoxia etc. Due to the use of mDixon acquisition, the DETECT technique also generates perfectly co-registered fat-suppressed T2-weighted images for improved anatomical localization of the lesions.

The multi-echo mDixon reconstruction combined with partial-echo acquisitions allowed high resolution T2W imaging with SSHTSE in a truly single acquisition, without increasing the scan time compared to SSHTSE acquisitions with and without fat suppression. Although, the slight increase in echo spacing ( $\sim 2.2$  ms) due to the acquisition of multi-echo mDixon increased T2 blurring, it was not substantial compared to the standard clinical SSHTSE images due to the use of small partial phase encoding factor (0.6), and parallel imaging (x3). However, the fat/water separation often failed at long TE using the standard mDixon reconstruction. Although several algorithms have been developed to improve the

fat/water separation, it is still challenging in images with low SNR (40,42,44). This is because the noise increases the uncertainty in solving the phase ambiguity during the phase-map estimation, especially for dual-echo IP/OP mDixon reconstruction. The proposed shared-field-map mDixon reconstruction used the  $B_0$  map from the short TE to overcome this limitation, and achieved uniform fat/water separation on the long TE images. Additionally, the shared field map between the two TEs also reduces the reconstruction times since the phase map estimation is often time consuming and needs to be estimated only once with shared-field-map mDixon reconstruction. Nevertheless, occasional fat/water swaps were noticed on short TE images at the edges of the FOV along the right/left direction (~52 cm FOV). However, these fat/water swaps were minor and restricted to the subcutaneous fat at the far edges of the FOV without affecting the detection of metastatic lesions in our study. Future optimization with improved fat/water separation methods (43) may potentially overcome these fat/water swaps.

The complex signal modeled by our phase-preserved homodyne reconstruction and the shared-field-map mDixon reconstruction allowed complex subtraction between the two water-only images. This complex subtraction eliminated the “dark-rim” artifacts, observed in the magnitude-subtracted water-only images. Since the fluid-like tissues have longer T2s, the Gibbs ringing artifacts observed with Cartesian view ordering are larger in images acquired with partial phase-encoding and partial readout than those acquired with full k-space. This amplifies the side lobes in PSF on magnitude images, which are canceled out by the complex subtraction and thus eliminating the “dark-rim” artifacts.

STIR is the most commonly used fat suppression method in WB-MRI due to its insensitivity to B0 inhomogeneities. However, STIR pulse imparts a mix of T1 and T2 contrast and thus, a T2W imaging sequence is typically included in the WB-MRI protocol. Compared to this, our DETECT imaging technique simultaneously provides standard T2W images with and without fat suppression in addition to the fat and fluid suppressed T2W images, all of them perfectly co-registered to each other, without increasing the total scan times as a consequence of the data for both TEs being acquired within the same excitation.

Whole-body DWIBS has been increasingly used for the detection of metastatic lesions, since the DWIBS images have increased lesion conspicuity (21,143). However, DWIBS images suffer from increased geometric distortions, combined with chemical shift artifacts and larger voxel size. Hence, the majority of DWIBS protocols are currently performed at 1.5T for whole-body imaging, necessitating longer scan times to compensate for the reduced SNR (21,144-146). Compared to DWIBS, our DETECT imaging technique provided images with superior SNR and higher spatial resolution in shorter scan times at 3T. Although the lesion-to-background conspicuity was not superior with DETECT compared to DWIBS, it generated images with fewer artifacts and minimal geometric distortions even in the presence of metal implants (e.g. Figure 7-9), making it more reliable. Due to the shorter acquisition times of less than 7 minutes for whole-body imaging, the DETECT imaging technique can also be performed in multiple orientations, if needed, to improve the lesion localization. Furthermore, DETECT imaging technique can be an appealing alternative technique for whole-body imaging, with the increasing availability of 3T scanners.

Our study has several limitations. First, although not directly considered a limitation, the DETECT imaging technique is based on prolonged T2 of the metastatic lesions, instead of the restricted diffusion that DWIBS relies on. Nevertheless, most lesions tend to have longer T2 with restricted diffusion and appear bright on T2W images (e.g. Figures 7-8 – 7-10). Some studies have shown better contrast with whole-body screening on lower b-value (50 s/mm<sup>2</sup>) than higher b-value (500 s/mm<sup>2</sup>) (130), where the contrast is primarily due to the longer T2 than the restricted diffusion. Next, the subtraction for fluid attenuation can reduce the contrast between the normal tissues and lesions, and may not be able to completely suppress the signals from complex fluids with moderate T2 values. However, the availability of water-only images at short TE and the use of effective T2 maps can offset these to improve the lesion conspicuity. Third, the DETECT acquisition of the thorax and abdomen required breath-holds. While this is an advantage compared to DWIBS to generate sharper images, it may be challenging in patients to perform multiple sequential breath-holds. In such scenario, DETECT images of the thorax and abdomen can be acquired using respiratory triggering, albeit at slightly prolonged acquisition times. Fourth, the use of variable refocusing flip angles reduced the signal intensities in the arteries, but veins appeared bright on the short TE image. The subtraction between the two TEs also did not reduce the vein vessel signal (reduced by ~5% only) since the T2 of the venous blood is relatively short (~70 ms) (147) and can obscure the lesion conspicuity. Future studies will consider the implementation of motion-sensitized driven equilibrium to reduce the signal intensities in these blood vessels (136). Finally, the DETECT imaging technique was initially tested in

only five mRCC patients and needs further evaluation in larger patient cohorts in multiple diseases.

## **7.7 CONCLUSION**

In conclusion, we have developed a fast, high-resolution, and high SNR T2-weighted imaging with simultaneous fat and fluid suppression, called DETECT, for whole-body MRI at 3T. Compared to the commonly used DWIBS for whole-body MRI, DETECT can be performed in significantly shorter scan times (17 min. vs. 7 min) and generates images with good lesion conspicuity, and without the image distortion associated with EPI. This sequence can serve as an initial imaging technique for whole-body cancer detection, followed by characterization of selected tumors by dedicated functional MR imaging.

## **CHAPTER EIGHT**

### **Diffusion Weighted Imaging using a Dixon based Single Shot Turbo Spin Echo**

#### **8.1 OVERVIEW**

Portions of this work were presented at the 25<sup>th</sup> annual meeting of International Society for Magnetic Resonance in Medicine (ISMRM) in Honolulu (April 2017) and the joint annual meeting ISMRM-ESMRMB in Paris (June 2018) respectively. The work will be submitted for publication.

#### **8.2 INTRODUCTION**

Diffusion Weighted Imaging (DWI) is an important diagnostic tool in neuroimaging and cancer imaging since it can provide high lesion conspicuity as well as quantitative information. The apparent diffusion coefficient (ADC) calculated from DW images can be used to quantify diffusion within the tissue, and to assess the cellular microstructure and cellular density.

In DWI, the image contrast is determined by the diffusion coefficients of protons in tissues. Tissues with the restricted diffusion of protons show high signal intensity, such as white matter and tumors. However, lipids, which are large molecules with abundant protons also show restricted diffusion. Combined with its long T<sub>2</sub>, fat shows large signal intensity in DW images, reduces the lesion conspicuity and may affect the measurement of the diffusion of water protons.

Fat suppression methods are commonly used in the DWI sequences, such as echo planar imaging (EPI) pulse sequences, which are routinely used in clinical DWI because of their fast speed and high SNR. The suppression of fat can improve the lesion conspicuity,

reduce the measurement bias of ADC and eliminate the chemical shift artifacts in diffusion weighted EPI (DW-EPI) image. However, EPI suffers from geometric distortions in areas with B0 inhomogeneity, resulting in poor localization, compromised sensitivity and specificity.

Diffusion weighted imaging using single-shot turbo spin-echo (DW-SShTSE) is increasingly used due to its robustness to geometric distortions compared to DW-EPI in challenging areas with B0 inhomogeneity such as spinal cord and inner auditory canal (IAC) imaging (148,149). Fat suppression with DW-SShTSE is achieved using spectrally selective inversion recovery (SPIR/SPAIR), but this approach suffers from incomplete fat suppression in challenging areas (e.g. spinal cord and IAC) with large field inhomogeneities. STIR can offer more uniform fat suppression but at the expense of reduced signal to noise ratio (SNR), which is a major challenge with DW-SShTSE.

Dixon methods have been proposed for uniform fat suppression in DWI (150-152). These methods use multi-acquisition Dixon, which acquires in-phase (IP) and out-of-phase (OP) images in separate repetition. The additional phase variations induced by DW gradients and motion can affect the water-fat separation, and image navigator is necessary to ensure robust water-fat separation (150). Multi-acquisition Dixon with image navigator will double the scan time for two-point Dixon. This will limit the application of Dixon method in DW-SShTSE because of already prolonged scan times. DW-SShTSE also suffers from low SNR, imposing an additional challenge for Dixon method.

Previously, we developed multi-echo Dixon based SShTSE sequence for robust water-fat separation in chapter 6 (135,153). Since IP and OP images were acquired in the

same repetition, multi-echo Dixon does not increase the total scan time compared to STIR and SPAIR (57,135). To improve the water-fat separation with low-SNR images, we also proposed a shared-field-map Dixon reconstruction method (153,154), which propagates a phase map estimated from high SNR images to the water-fat separation of low SNR images. The purpose of this work was to develop a DW SShTSE using a multi-echo Dixon based acquisition (135) combined with shared field map between lower and higher b-values for uniform fat suppression without increasing the total scan time.

## 8.3 METHODS AND MATERIALS

### 8.3.1 Pulse Sequence

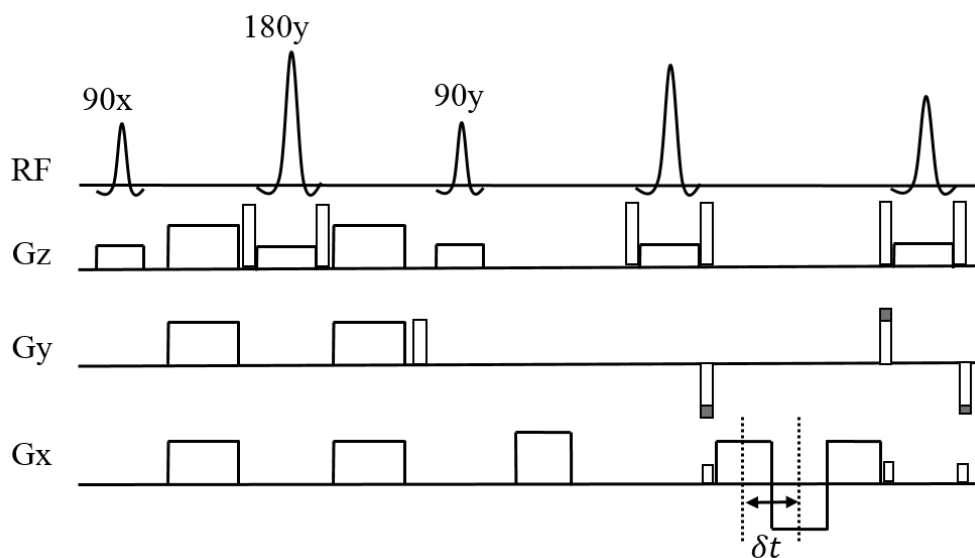


**Figure 8-1 DW-SShTSE with phase insensitive diffusion preparation and multi-echo Dixon**

Phase insensitive diffusion preparation and multi-echo Dixon was implemented in single-shot-TSE sequence. Phase insensitive diffusion preparation can eliminate the non-CPMG component. Multi-echo Dixon acquisition was implemented to acquire IP and OP images in the same repetition.

The schematic diagram of the proposed DW SShTSE pulse sequence with multi-echo Dixon is shown in Figure 8-1. Compared to the conventional diffusion preparation, an additional  $90^\circ$  pulse with a dephasing gradient and a crusher gradient was included in the phase insensitive diffusion preparation to eliminate the non-CPMG component and stabilize the signal (155). Half scan was used in SShTSE to reduce the echo train length, and it would cover k-space from  $-k$  to  $+k_{\max}$ . Since the dephasing gradients are applied in phase-encoding direction, it will overlap with the phase-encoding gradients. To reduce the gradient strength, a dephasing gradient with opposite sign (positive) to the maximum phase-encoding gradient was implemented. In the data acquisition, multi-echo Dixon was implemented. Between each pair of refocusing pulses, IP and OP images were acquired using the bipolar gradients. The sequence was implemented on a 3T Ingenia scanner (Philips Healthcare, Best, The Netherlands).

### 8.3.2 Reconstruction

The phase insensitive diffusion weighting preparation (155) was combined with a multi-echo Dixon SShTSE, where the In-Phase (IP) and Out-of-Phase (OP) images are acquired in the same repetition. After the reference point, the CPMG condition was imposed and the signal can be modeled as:

$$S_{n,m} = (W_m + c_n F_m) e^{i(\varphi_n + \psi_m)} \quad \text{Equation 8.1}$$

where  $n, m$  are the numbers of echo and b-value respectively. Water ( $W$ ) and fat ( $F$ ) are considered complex with  $\varphi_n$  corresponding to the field strength offset  $\Delta B_0$  and echo times (TE). The additional phase induced by motion and/or DW gradients ( $\psi_m$ ) would be nonzero at  $b > 0$  and simultaneously affects the echoes acquired in the same repetition.

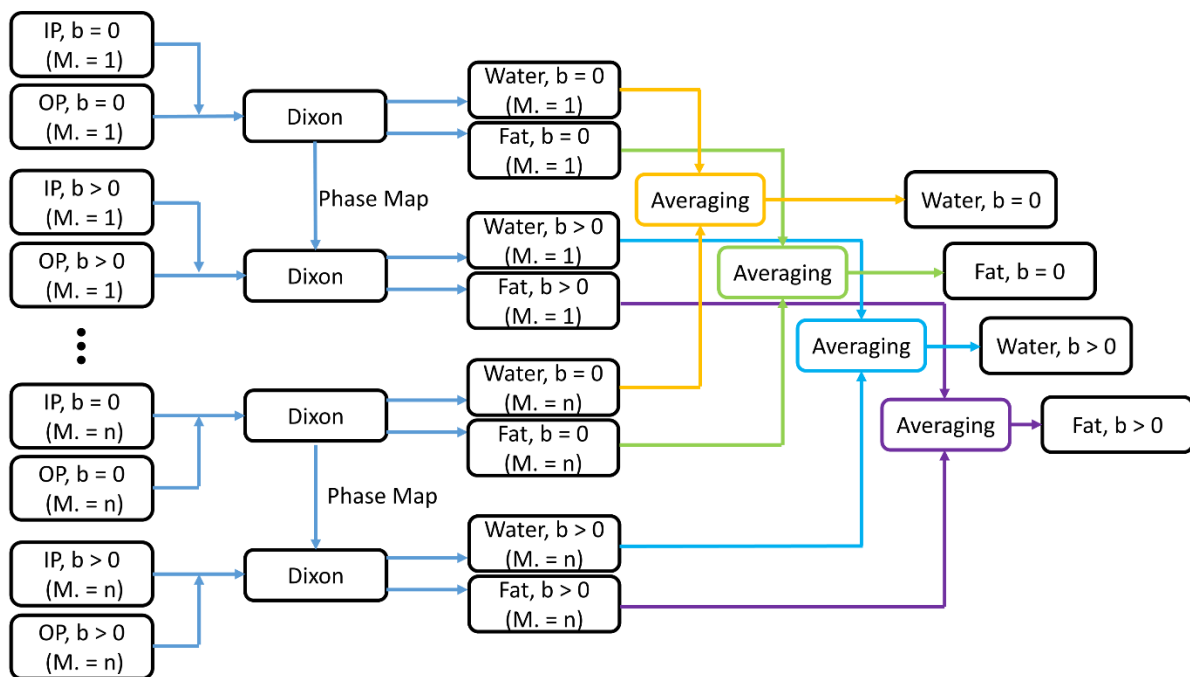


**Figure 8-2 Reconstruction pipeline of DW SShTSE with multi-echo Dixon and shared-field-map Dixon**

Standard Dixon reconstruction will be performed with IP and OP images acquired at  $b = 0$   $s/mm^2$ , generating water-only and fat-only images as well as phase map. The phase map estimated from  $b = 0$  images will be used in the shared-field-map Dixon reconstruction to separate water and fat with  $b > 0$  images. The water-only and fat-only images will be averaged using the amplitude averaging.

Phase insensitive diffusion preparation and multi-echo Dixon was implemented in a single-shot-TSE sequence. Phase insensitive diffusion preparation can eliminate the non-CPMG component. Multi-echo Dixon acquisition was implemented to acquire IP and OP images in the same repetition.

If IP and OP echoes are acquired at  $b=0$ , then  $\psi_0 = 0$  and  $\Delta\phi_0 = e^{i(\phi_2 - \phi_1)}$ .  $W_0$  and  $F_0$  at  $b=0$  can be calculated using the conventional fat/water separation method(40):

$$\begin{pmatrix} W_0 \\ F_0 \end{pmatrix} = \frac{1}{c_2 - c_1} \begin{bmatrix} c_2 & c_1 \\ -1 & 1 \end{bmatrix} \begin{pmatrix} S_{1,0} \\ S_{2,0} \Delta \phi_0^* \end{pmatrix} \quad \text{Equation 8.2}$$

where  $c_1$  and  $c_2$  are the complex vectors of fat with multiple spectral peaks at TE1 and TE2.

If  $\Delta B_0$  and TE are identical between different b values,  $\Delta \phi_m = e^{i(\phi_2 - \phi_1)} = \Delta \phi_0$ . For  $b > 0$ , eq.2 can be written as:

$$\begin{pmatrix} W_m \\ F_m \end{pmatrix} = \frac{1}{c_2 - c_1} \begin{bmatrix} c_2 & c_1 \\ -1 & 1 \end{bmatrix} \begin{pmatrix} S_{1,m} \\ S_{2,m} \Delta \phi_0^* \end{pmatrix} e^{i\psi_m} = \begin{pmatrix} W'_m \\ F'_m \end{pmatrix} e^{i\psi_m} \quad \text{Equation 8.3}$$

$\begin{pmatrix} W'_m \\ F'_m \end{pmatrix}$  can be estimated using  $S_{n,m}$  and shared field map  $\Delta \phi_0$ . Although  $\psi_m$  is

unknown, it only modulates the phase and doesn't affect the magnitude of the final reconstructed water and fat images at higher b-values, which are  $|W_m| = |W'_m e^{i\psi_m}|$  and  $|F_m| = |F'_m e^{i\psi_m}|$ . In DWI, magnitude averaging is used to eliminate the signal loss due to phase variations. Therefore, the additional phase  $\psi_m$  will also not affect the process of DWI images. The reconstruction pipeline is shown in Figure 8-2.

### 8.3.3 Imaging Studies

The proposed sequence and reconstruction method were first evaluated in a brain imaging of a 38-year-old female healthy volunteer. Then, phantom study was conducted to quantify the ADC measurements. Finally, 8 healthy volunteers (4 female, 4 male, age range: 23 – 37 years) were enrolled for the evaluation of the proposed method in the cervical spine imaging. The study protocol was approved by the institutional review board (IRB), Health Insurance Portability and Accountability Act (HIPAA)-compliant and all subjects provided written informed consent prior to their participation in the study.

### 8.2.3.1 Brain Imaging

A coronal brain imaging was performed with a 38-year-old female healthy volunteer to validate the shared-field-map Dixon reconstruction. The acquisition parameters for the coronal DW SShTSE Dixon sequence were: FOV =  $200 \times 180$  mm<sup>2</sup>; slice thickness/slice gap = 4 mm/1 mm; voxel size =  $0.9 \times 0.9$  mm<sup>2</sup>; SENSE = 3; echo spacing = 10.3 ms; diffusion echo time = 57 ms; TR = 8000 ms;  $\delta t = 1.1$  ms; number of slices = 12; NSA = 4; partial phase-encoding factor = 0.65; b = 0, 500, 1000 s/mm<sup>2</sup> and scan time = 2:08 min.

To compare DW single shot EPI and DW SShTSE, transverse brain imaging was performed with the same volunteer, because DW single shot EPI was commonly performed in the transverse plane to reduce the geometric distortions in brain imaging. The acquisition parameters for the DW single shot EPI sequence were: FOV =  $220 \times 220$  mm<sup>2</sup>; slice thickness/slice gap = 4 mm/1 mm; voxel size =  $1.1 \times 1.1$  mm<sup>2</sup>; SENSE = 3; TR = 1578 ms; number of slices = 12; NAS = 4; fat suppression: SPIR; partial phase-encoding factor = 0.65; b = 0, 500, 1000 s/mm<sup>2</sup> and scan time = 46 sec. The DW SShTSE Dixon used the same parameters as the DW single shot EPI, except TR = 8000 ms;  $\delta t = 1.1$  ms and scan time = 2 min. A 15-channel phased-array head coil was used for signal reception.

### 8.2.3.2 Phantom Imaging

To assess the ADC measurements using DW SShTSE Dixon sequence, a phantom study was performed. Phantoms with sucrose concentrations of 0.4, 0.8, 1.6 M and peanut oil were scanned with DW SShTSE Dixon, DW SShTSE SPIR and DW EPI sequences. DW SShTSE Dixon and SPIR sequences used same acquisition parameters: FOV =  $250 \times 120$  mm<sup>2</sup>; slice thickness = 4 mm; voxel size =  $1 \times 1$  mm<sup>2</sup>; SENSE = 2; TR = 5000 ms; number

of slices = 13; NSA =6; b = 0, 200, 400, 800 s/mm<sup>2</sup> and scan time = 5 min. DW EPI also used the same acquisition parameters, except TR = 2500 ms; partial phase-encoding factor =0.65 and scan time = 2:20 min. ADC maps were calculated using the log-linear fitting. Tukey's multiple comparison test was used to compared the ADC values measured from DW SShTSE Dixon, DW SShTSE SPIR and DW EPI images. GraphPad Prism6 (GraphPad, San Diego, CA) was used to perform the Tukey's multiple comparison test with p<0.05 considered statistically significant.

### 8.2.3.3 Cervical Spine Imaging

To assess the performance of the proposed DW SShTSE Dixon in challenging areas with large B<sub>0</sub> inhomogeneity, cervical spine imaging was performed on 8 healthy volunteers. The proposed method was optimized and compared against DW EPI and DW SShTSE SPIR. DW SShTSE Dixon and SPIR sequences used same acquisition parameters: FOV = 220 × 150 mm<sup>2</sup>; slice thickness = 4 mm; acquisition voxel size = 2 × 2 mm<sup>2</sup>; reconstruction voxel size = 1 × 1 mm<sup>2</sup>; SENSE = 2; TR = 5000 ms; number of slices = 13; NSA =6; b = 0, 400 s/mm<sup>2</sup> and scan time = 3:05 min. DW EPI also used the same acquisition parameters, except TR = 2500 ms; partial phase-encoding factor =0.65 and scan time = 1:40 min. One volunteer was scanned with three b-values (0, 400 and 800 s/mm<sup>2</sup>) to generate more accurate ADC maps.

## 8.4 RESULTS

Figure 8-3 demonstrates the use of shared field map between b=0 and 1000 s/mm<sup>2</sup> for uniform fat/water separation. The native B<sub>0</sub> from its own acquisition generates uniform fat/water separation at b = 0 s/mm<sup>2</sup> (Figure 8-3, top row), but fails at b = 1000 s/mm<sup>2</sup> due to

lower SNR (Figure 8-3, middle row). Using the shared field map from  $b = 0 \text{ s/mm}^2$ , uniform fat/water separation was achieved at  $b = 1000 \text{ s/mm}^2$  (Figure 8-3, bottom row).

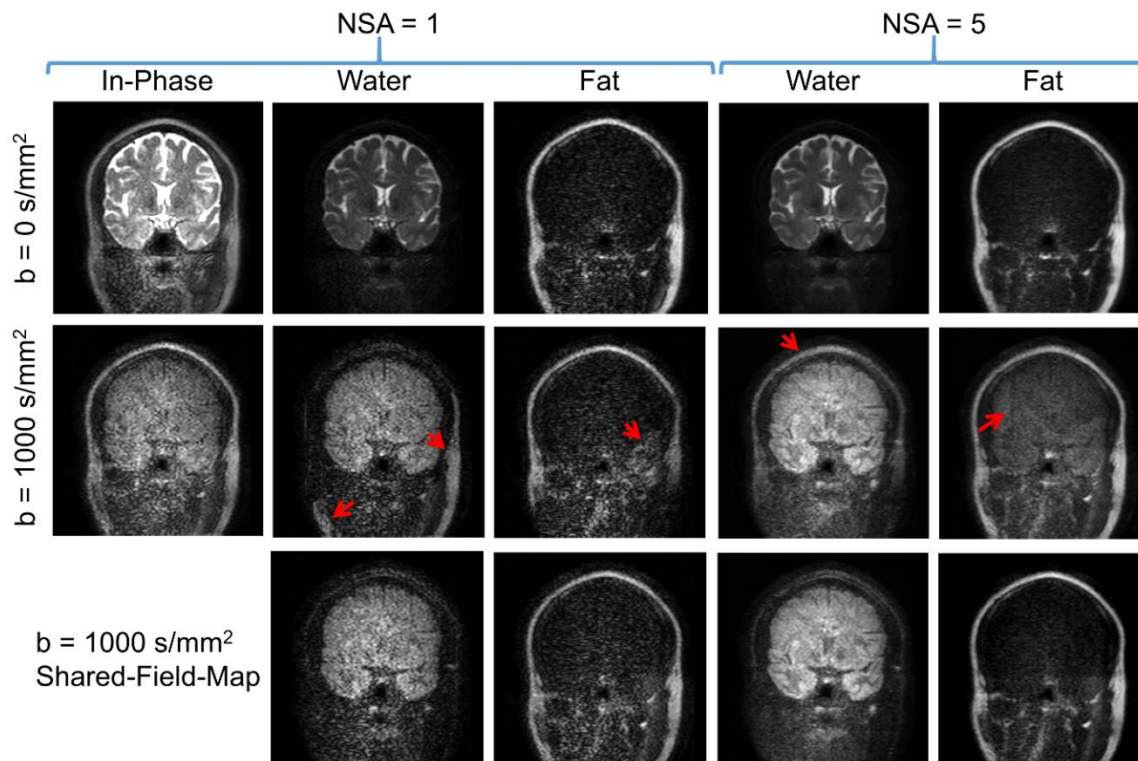


**Figure 8-3 DW SShTSE Dixon with standard reconstruction and shared field map Dixon reconstruction**

The standard Dixon achieved uniform water-fat separation at  $b = 0 \text{ s/mm}^2$ , while it failed to separate water and fat at  $b = 1000 \text{ s/mm}^2$  (red arrows) due to low SNR. Shared-field-map Dixon reconstruction eliminated the water-fat swaps at  $b = 1000 \text{ s/mm}^2$ .

The axial DW images of the brain are shown in Figure 8-4. Homogeneous water-fat separation was achieved using DW SShTSE Dixon (Figure 8-4, top and middle rows). SShTSE acquisition is not sensitive to  $B_0$  inhomogeneity, and no obvious geometric distortions can be observed in the DW SShTSE Dixon images. However, significant

geometric distortions are observed in skull base due to large B0 inhomogeneity (Figure 8-4, bottom row).

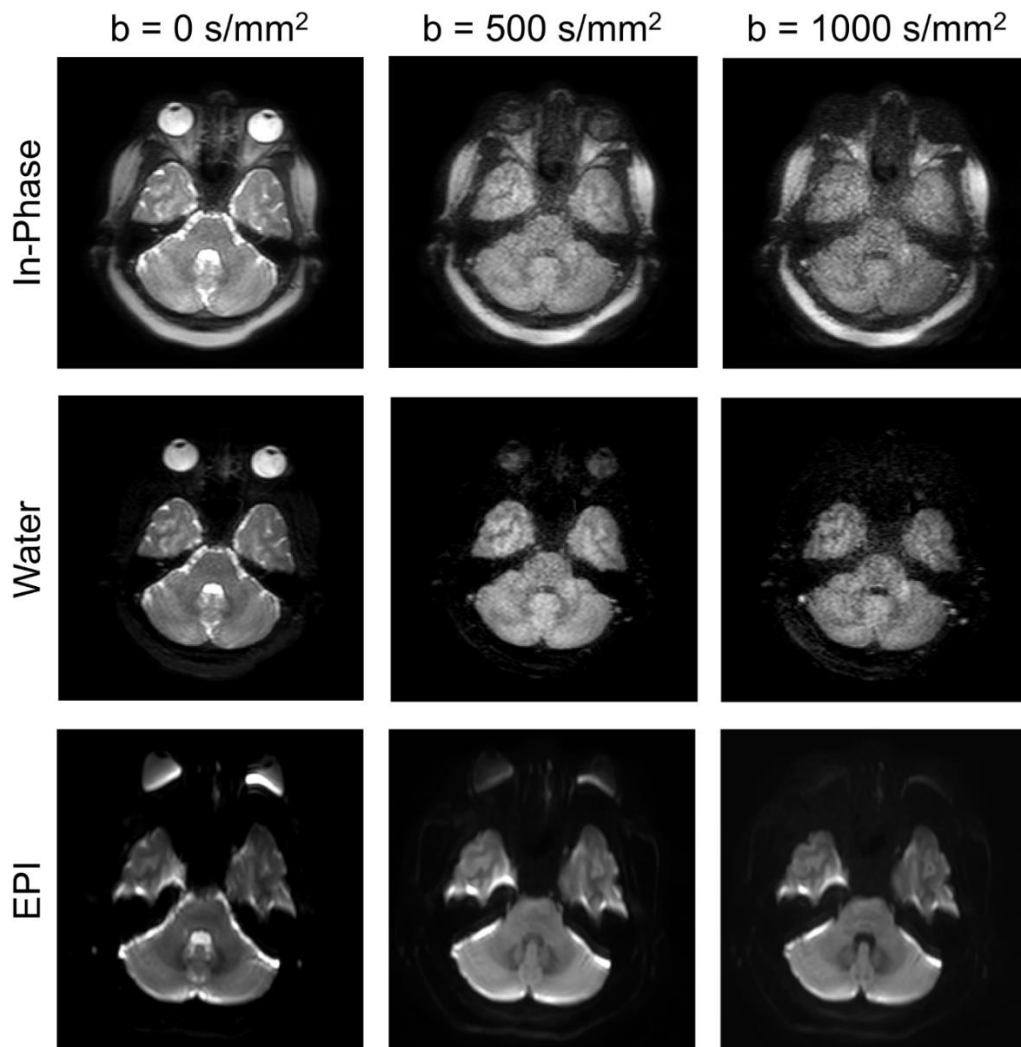


**Figure 8-4 Axial brain imaging using DW SShTSE Dixon and DW EPI**

With shared-field-map Dixon, DW SShTSE Dixon achieved uniform water-fat separation at all b-values. The IP and water-only images are free of geometric distortions, since SShTSE acquisition is robust to B0 inhomogeneity. However, EPI is sensitive to B0 inhomogeneity, and significant geometric distortions can be observed around temporal lobes and eyes.

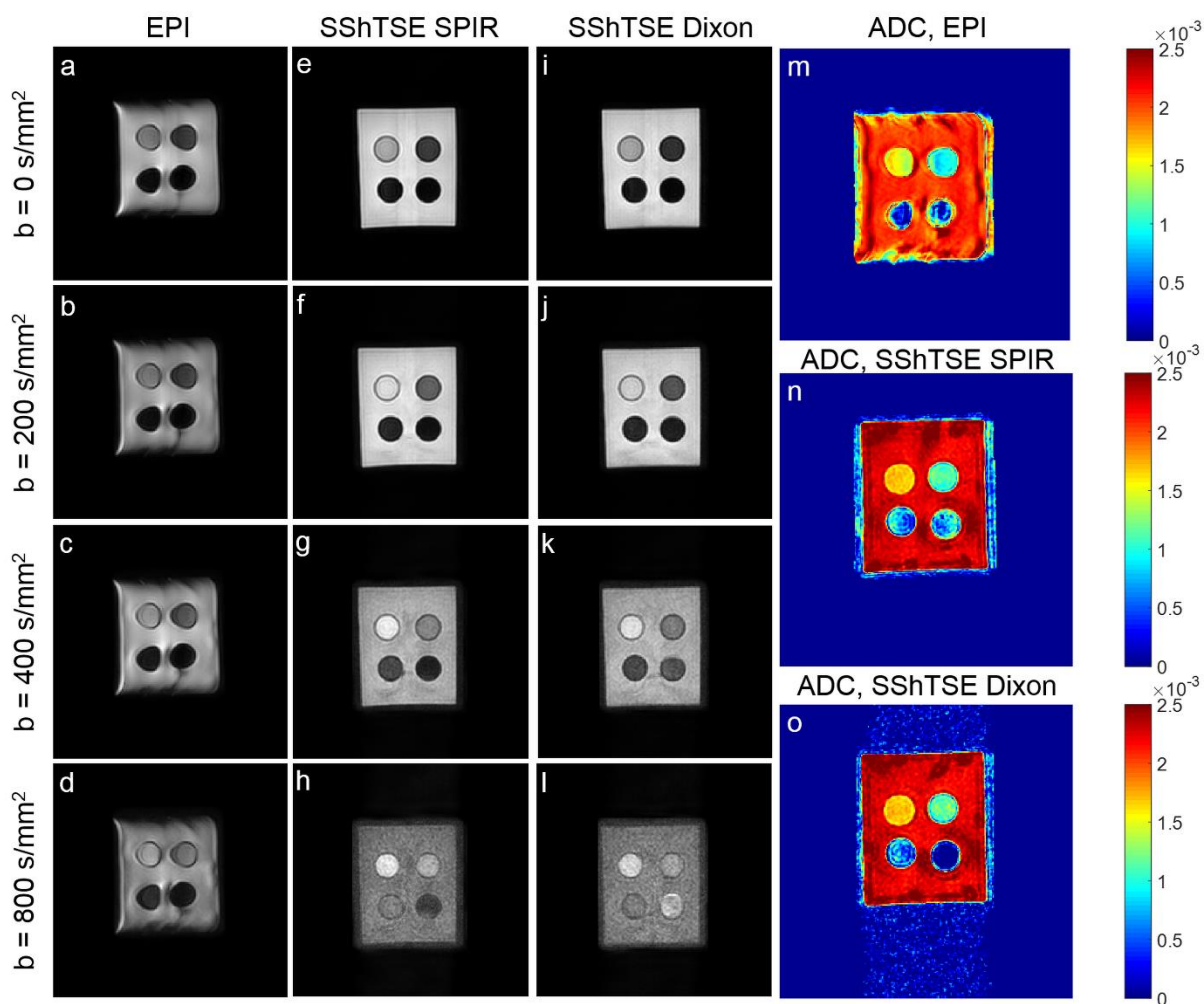


**Figure 8-5 Diffusion weighted images and ADC maps of sucrose phantoms**

$b = 0, 200, 400, 800 \text{ s/mm}^2$  images were acquired using DW EPI (a - d), DW SShTSE SPIR (e - h) and DW SShTSE Dixon (i - l). ADC maps (m - o) were calculated using the log-linear fitting. In the ADC map calculated from DW EPI images, the large ADC variations were due to the geometric distortions.

Figure 8-5 shows the phantom results. In DW EPI images (Figure 8-5a – 8-5d), geometric distortions are observed at corners and around the bottles. DW SShTSE SPIR (Figure 8-5e – 8-5h) and DW SShTSE Dixon (Figure 8-5i – 8-5l) generated images without

geometric distortions, but the SNR of the images is lower than that of DW EPI. SPIR and Dixon all achieved efficient fat suppression because of the small FOV and the utilization of water bath.

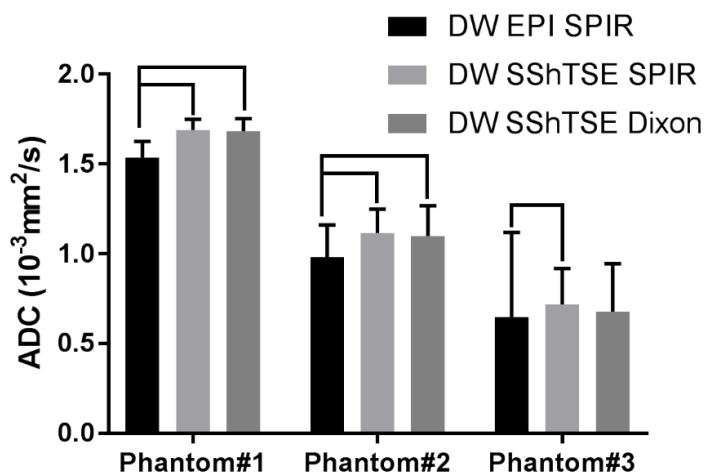


**Figure 8-6 ADC measurements of sucrose phantoms**

Phantoms were sucrose solutions with concentrations of 0.4 M (Phantom #1), 0.8 M (Phantom #2) and 1.6 M (Phantom #3). For phantom #1, the ADC values were  $1.53 \pm 0.10 \times 10^{-3} \text{ mm}^2/\text{s}$  (DW EPI SPIR),  $1.68 \pm 0.04 \times 10^{-3} \text{ mm}^2/\text{s}$  (DW SShTSE SPIR) and  $1.69 \pm 0.05 \times 10^{-3} \text{ mm}^2/\text{s}$  (DW SShTSE Dixon). For phantom #2, the ADC values were  $0.97 \pm 0.15 \times 10^{-3} \text{ mm}^2/\text{s}$  (DW EPI SPIR),  $1.11 \pm 0.07 \times 10^{-3} \text{ mm}^2/\text{s}$  (DW SShTSE SPIR) and  $1.17 \pm 0.11 \times 10^{-3} \text{ mm}^2/\text{s}$  (DW SShTSE Dixon). For phantom #3, the ADC values were  $0.65 \pm 0.6 \times 10^{-3} \text{ mm}^2/\text{s}$  (DW EPI SPIR),  $0.72 \pm 0.20 \times 10^{-3} \text{ mm}^2/\text{s}$  (DW SShTSE SPIR) and  $0.68 \pm 0.27 \times 10^{-3} \text{ mm}^2/\text{s}$  (DW SShTSE Dixon). The ADC values measured using DW SShTSE Dixon have a good agreement with that measured using DW SShTSE SPIR. The ADC values measured using SShTSE were slightly higher than that measured using EPI.

The measured ADC values of these sucrose phantoms were shown in Figure 8-6. There were no significant differences between the ADC values measured using DWI

SShTSE SPIR and DWI SShTSE Dixon (0.4 M sucrose phantom:  $1.68 \pm 0.04 \times 10^{-3} \text{ mm}^2/\text{s}$  vs.  $1.69 \pm 0.05 \times 10^{-3} \text{ mm}^2/\text{s}$ ; 0.8 M sucrose phantom:  $1.11 \pm 0.07 \times 10^{-3} \text{ mm}^2/\text{s}$  vs.  $1.7 \pm 0.11 \times 10^{-3} \text{ mm}^2/\text{s}$ ; 1.6 M sucrose phantom:  $0.72 \pm 0.20 \times 10^{-3} \text{ mm}^2/\text{s}$  vs.  $0.68 \pm 0.27 \times 10^{-3} \text{ mm}^2/\text{s}$ ). Compared to the ADC values measured using SShTSE SPIR and DWI SShTSE Dixon, the ADC values of phantoms with sucrose concentration of 0.4 and 0.8 M measured using DW EPI were significantly lower (0.4 M sucrose phantom:  $1.53 \pm 0.10 \times 10^{-3} \text{ mm}^2/\text{s}$ ,  $P < 0.001$ ; 0.8 M sucrose phantom:  $0.97 \pm 0.15 \times 10^{-3} \text{ mm}^2/\text{s}$ ,  $P < 0.001$ ). For the phantom with sucrose concentration of 1.6 M, the ADC value measured using DW EPI ( $0.65 \pm 0.6 \times 10^{-3} \text{ mm}^2/\text{s}$ ,  $P < 0.005$ ) was also significantly lower than that measured using DW SShTSE SPIR, while there were no significant differences between the ADC values of measured using DWI SShTSE SPIR and DWI SShTSE Dixon due to the large variation.

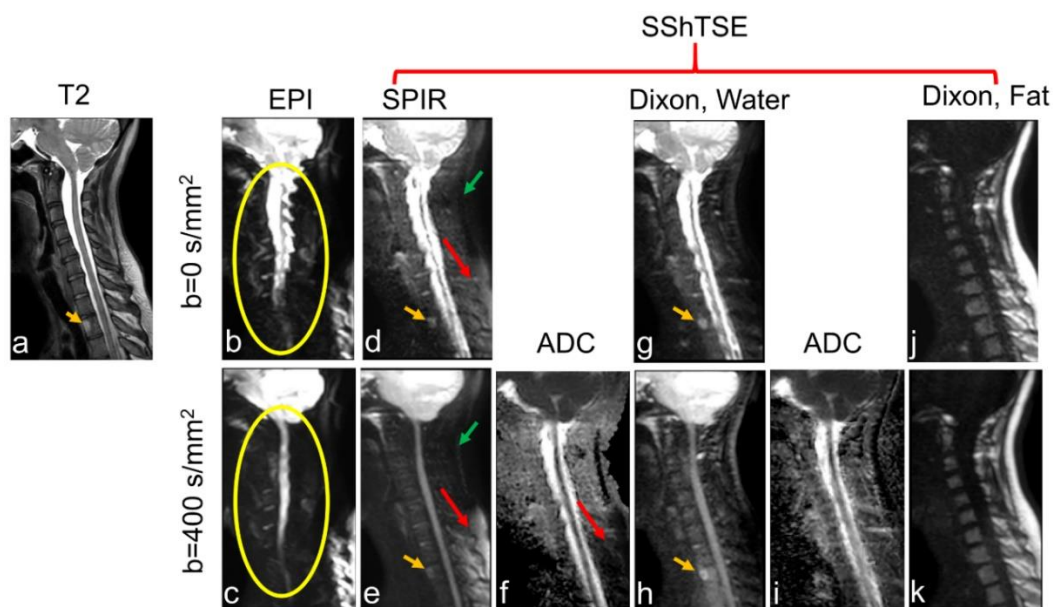


**Figure 8-7 Diffusion weighted imaging of cervical spinal cord**

Structural undistorted T2 reference (a), DWI-EPI (b,  $b = 0 \text{ s/mm}^2$ ; c,  $b = 400 \text{ s/mm}^2$ ), DWI-SShTSE-SPIR (d,  $b = 0 \text{ s/mm}^2$ ; e,  $b = 400 \text{ s/mm}^2$ ; f, ADC), water (g,  $b = 0 \text{ s/mm}^2$ ; h,  $b = 400$

s/mm<sup>2</sup>; i, ADC) and fat images (j, b = 0 s/mm<sup>2</sup>; k, b = 400 s/mm<sup>2</sup>) using proposed method of a volunteer with a suspected vertebral lesion (orange arrow). It is difficult to find the lesion in distorted DWI-EPI images. Incomplete fat suppression (d, e, red arrows) and shading artifacts (d, e, green arrows) can be observed in DWI-SShTSE-SPIR images, while the proposed method successfully separated water and fat for b = 0 s/mm<sup>2</sup> and b = 400 s/mm<sup>2</sup> (g, h, j, k). The resulting images were also free of distortion.

The shared field map approach using multi-echo Dixon also improved fat/water separation in spine imaging, which is more challenging due to significantly lower SNR and segmented appearance of the intervertebral discs (Figure 8-7). DW SShTSE Dixon provides diffusion weighted images (Figure 8-7g, 8-7h) with minimal to no image distortion compared to DW EPI (Figure 8-7b, 8-7c), and with uniform fat suppression compared to DW SShTSE SPIR (Figure 8-7d, 8-7e). A suspected vertebral lesion was more obvious in b = 400 s/mm<sup>2</sup> water-only image than SPIR because of the improved fat suppression, while the suspected vertebral lesion was not visible in DW EPI images due to distortions. With the DW SShTSE Dixon, uniform fat suppression across the entire field of view was also achieved, as shown in Figure 8-8.

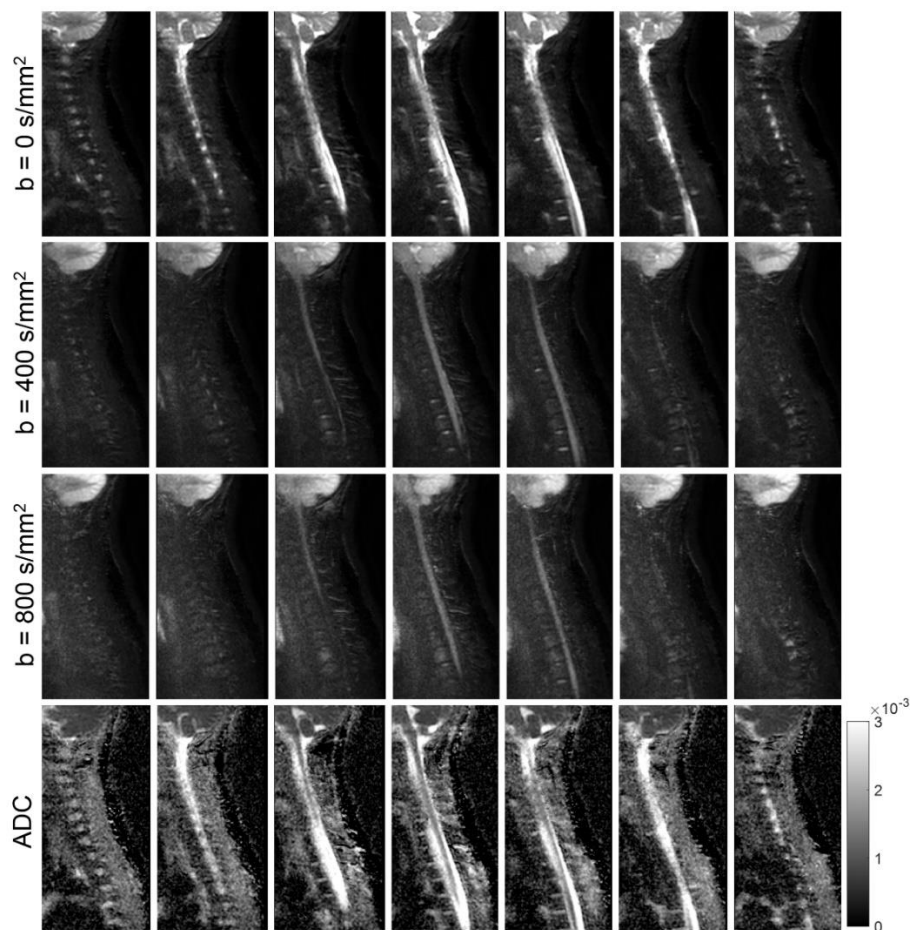


**Figure 8-8 Sagittal diffusion images of a healthy volunteer acquired with DW SShTSE Dixon**

The water-only images at different b-values demonstrated uniform water-fat separation using the proposed DW SShTSE Dixon sequence and shared-field-map Dixon reconstruction. Six averages were used for each direction. High b-value images were acquired in three directions (x-, y- and z-directions) and were combined by taking the geometric mean. The ADC maps were generated from the combined water-only images using a log-linear fitting.

## 8.5 DISCUSSION

TSE based diffusion weighted imaging is increasingly used in areas with B0 inhomogeneity because of its robustness to geometric distortions. Since it suffers from low

SNR, TSE based diffusion weighted imaging commonly uses spectral selective fat suppression methods to suppress fat instead of STIR. However, spectral selective fat suppression is sensitive to  $B_0$  inhomogeneity, resulting in incomplete fat suppression in TSE based diffusion weighted images. In this work, we have combined the multi-echo Dixon (57) with TSE based diffusion weighted imaging technique (155) to improve the fat suppression in diffusion weighted images without sacrificing the scan time and SNR. We have also demonstrated that the shared-field-map Dixon reconstruction can achieve robust water-fat separation in high b-value images, which suffers from low SNR.

Multi-echo Dixon acquired IP and OP images in the same repetition, and thus will not significantly increase the scan time compared to DW SShTSE with SPIR. Although the echo spacing was slightly increased ( $\sim 2.2$  ms) due to the acquisition of multi-echo mDixon, it will not significantly increase the repetition time due to the use of partial phase encoding and parallel imaging. The increased echo spacing may result in image blurring. However, the diffusion weighted images are often acquired with a low spatial resolution to reduce the scan time and to improve the SNR, the blurring due to the slightly increased echo spacing is subtle, as shown in the phantom and in vivo images.

It is difficult to unwrap the phase for water-fat separation where the image SNR is low (156). Therefore, the water-fat separation often failed at large b-values using the standard mDixon reconstruction. Although several algorithms have been developed to improve the fat/water separation (40,42,44), it is still challenging in images with low SNR. The previously proposed shared-field-map Dixon reconstruction used the  $B_0$  map from high SNR image to overcome this limitation (153,154). However, compared to the previous

studies (153,154), there will be an additional phase between  $b = 0 \text{ s/mm}^2$  image and high  $b$ -value images since they were acquired with different diffusion preparation in different repetitions. In this work, we demonstrated that the additional phase will not affect the water-fat separation using shared-field-map Dixon reconstruction, and the additional phase will only modulate the final water- and fat-only images as all the IP and OP images were acquired in the same repetition. Since magnitude averaging is commonly used in the DW imaging to avoid the problem of motion induced phase errors (157,158), the additional phase will also be removed, and will not affect the DW image post-processing. It should be noted that the water-fat separation in high  $b$ -value images relies on the water-fat separation in  $b = 0 \text{ s/mm}^2$  image. If the water-fat separation failed in  $b = 0 \text{ s/mm}^2$  image, same water-fat swaps will also be observed in high  $b$ -value images.

Since SSHTSE acquisition is insensitive to  $B_0$  inhomogeneity, the SSHTSE DW images are free from geometric distortions, while EPI DW images showed geometric distortions in phantoms and volunteers. The ADC values of phantoms measured by the DW SSHTSE Dixon and DW SSHTSE SPIR showed good agreement. However, DW SSHTSE Dixon and SPIR measured slightly higher ADC values compared to DW single-shot EPI. The differences in ADC measurement between DW SSHTSE and DW EPI has also been reported in previous comparison studies (159,160), and this is probably due to the geometric distortions in EPI DW images.

Diffusion weighted imaging of cervical spine is very challenging for DW EPI due to the large  $B_0$  inhomogeneity in the cervical spine. The geometric distortions in EPI DW images will not only hamper the quantification measurement, but also affect the

interpretation. However, diffusion weighted imaging of cervical spine with SShTSE acquisition is free of geometric distortions, improving the image quality. The major limitations of the DW SShTSE methods are long acquisition time and low SNR. The SNR can be increased by increasing the NSA, which will also prolong the acquisition time. Simultaneous multislice acquisition can be used to reduce the acquisition time (161).

In diffusion weighted imaging of cervical spine, multi-echo Dixon showed improved fat suppression compared to SPIR, which is commonly used in DW SShTSE for fat suppression due to high SNR. Incomplete fat suppression can affect the lesion conspicuity as well as the ADC measurements. Besides the improved fat suppression, DW SShTSE Dixon can also generate fat images, which can be used to measure the fat diffusion (162) in the future. However, a dramatically large b-values are required for the diffusion weighted imaging of fat.

There are several limitations of this study. First, the quantitative comparison of ADC measurements was not conducted with previously developed diffusion phantoms (163,164). Thus, there is a lack of comparison with previous studies. In the future, the proposed sequence will be evaluated with standardized diffusion phantoms. Second, the study focuses on the technical development, and the proposed methods were only optimized and evaluated in normal volunteers. The performance of the proposed method in diagnosis will be assessed with patients in the future. Finally, the comparison of in vivo ADC measurements was not conducted since the number of volunteers is small and only two b-values (0, 400) were used in most volunteer scans.

In conclusion, we have demonstrated multi-echo Dixon approach with shared-B0-map that can improve fat/water separation in DW-SShTSE imaging without the need for additional image navigators. The resulting images are free of geometric distortion with uniform fat suppression, allowing accurate measurement of water diffusion compared to DW-EPI and DW-SShTSE-SPIR even in locations with significant field inhomogeneities such as cervical spine. Furthermore, this approach also allows measurement of ADC in fat.

## **8.6 FUTURE**

Diffusion weighted imaging using single-shot turbo spin echo (DW-SShTSE) with Dixon showed uniform fat suppression without geometric distortions, compared to DW-EPI and DW-SShTSE with spectrally selective fat suppression (SPIR). However, the water-fat separation in high b-value images relied on the water-fat separation in  $b = 0$  s/mm<sup>2</sup> image. The phase insensitive preparation used in DW-SShTSE reduces the SNR by half, impeding the robustness of Dixon reconstruction in  $b = 0$  s/mm<sup>2</sup> image. To improve the SNR and Dixon reconstruction, I developed a hybrid DW-SShTSE, where the  $b=0$  s/mm<sup>2</sup> image was acquired without the phase insensitive preparation.

### **8.6.1 Hybrid DWI SShTSE Dixon**

The above DW-SShTSE-Dixon (Figure 8-9a) utilized the phase insensitive diffusion weighting preparation, followed by shared field-map between the  $b=0$  s/mm<sup>2</sup> image and the higher b-value images for robust fat/water separation across all b-values. However, the additional dephasing gradient that was employed to eliminate the non-CPMG component with the phase insensitive preparation decreased the original signal by half, reducing the overall SNR.

Since there is no diffusion gradient applied for  $b=0$  s/mm<sup>2</sup> image, the dephasing gradient can be safely removed to regain the original signal for improved SNR and robust fat/water separation. We refer this as the hybrid DWI-SShTSE Dixon sequence, in which the images at  $b = 0$  s/mm<sup>2</sup> and non-zero  $b$ -values are acquired without and with the dephasing gradient respectively (Figure 8-9b).

In the conventional DWI, the apparent diffusion coefficient (ADC) is calculated as

$$\text{ADC} = \frac{\ln\left(\frac{S_0}{S_1}\right)}{b_1 - b_0} \quad \text{Equation 8.1}$$

where  $S_0$  and  $S_1$  are the signal intensities at  $b_0$  and  $b_1$ . However, without the dephasing gradient, the signal obtained with the hybrid DWI-SShTSE-Dixon at  $b=0$  s/mm<sup>2</sup> will be doubled. Thus, the modified ADC can be calculated as:

$$\text{ADC} = \frac{\ln\left(\frac{S_0}{2S_1}\right)}{b_1 - b_0} \quad \text{Equation 8.2}$$

To minimize the effect of B0 drifts (165) on shared-filed-map, the image acquisition was interleaved by signal average (NSA) (Figure 8-9d) instead of  $b$ -values (Figure 8-9c) to shorten the gap between different  $b$ -value images.

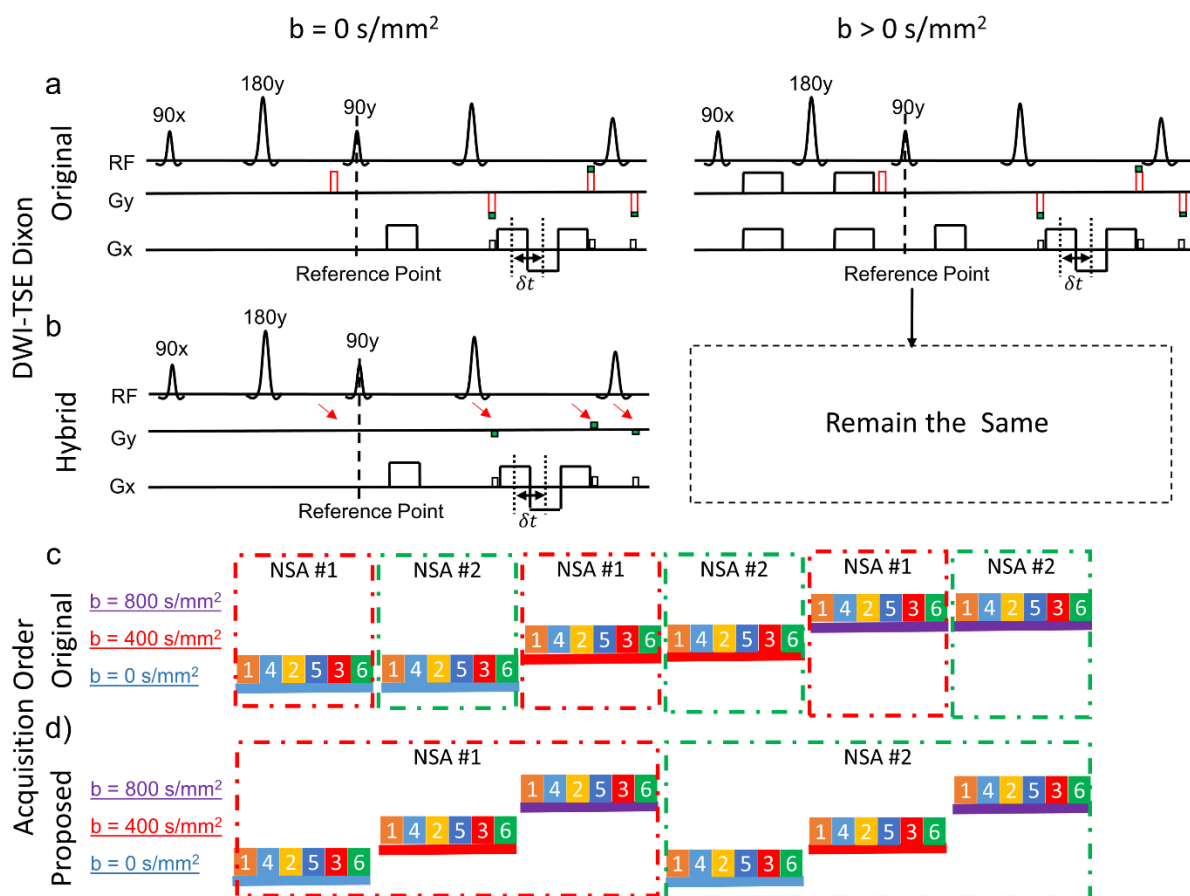


**Figure 8-9 Schematic diagram of the hybrid DWI-TSE Dixon and the proposed acquisition order**

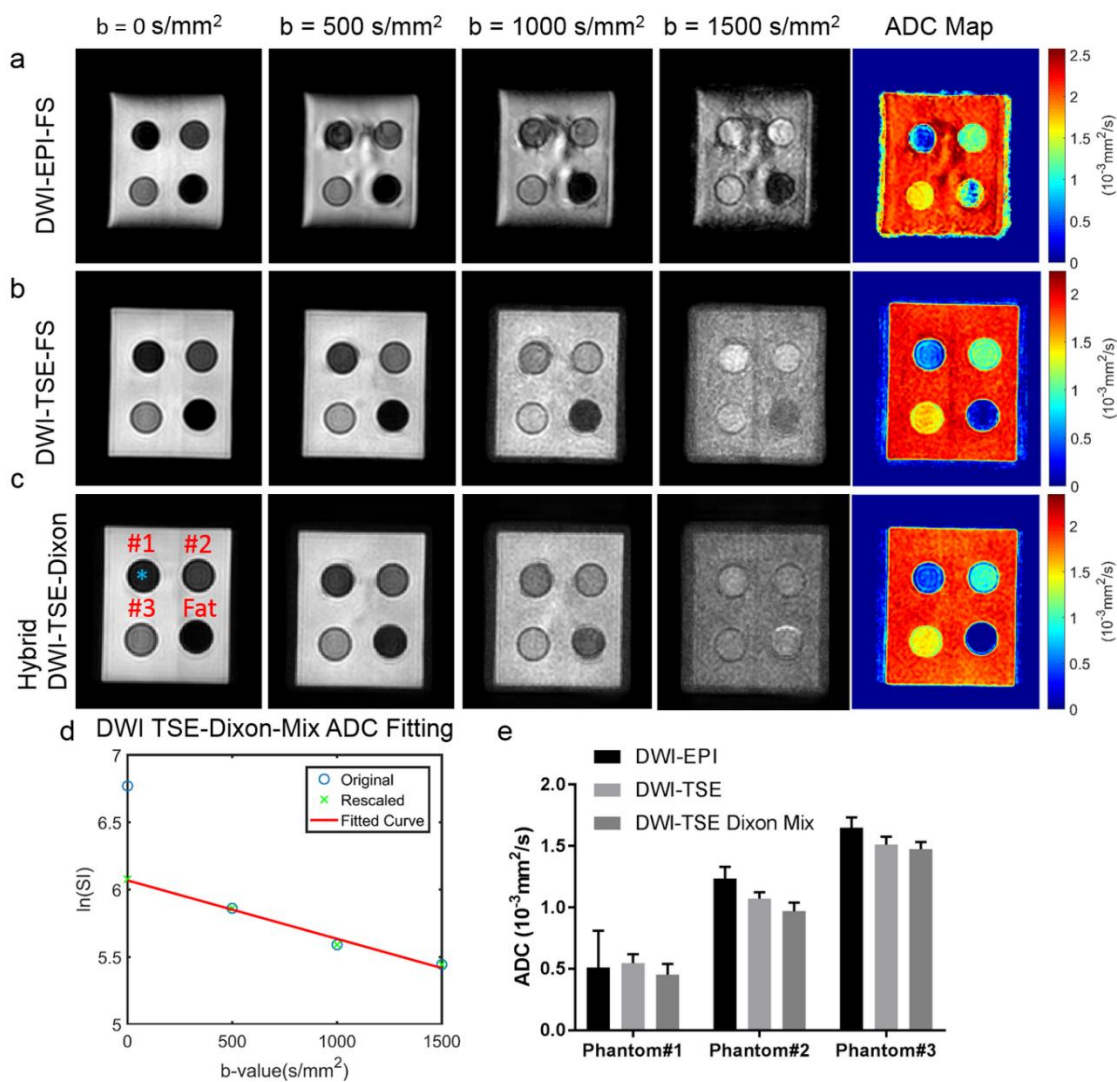
a) Previously proposed DW-SShTSE-Dixon method, combined phase insensitive diffusion preparation with multi-echo Dixon acquisition. b) Proposed hybrid DW-SShTSE-Dixon eliminates the dephasing gradient (arrows) at  $b=0 \text{ s/mm}^2$ . c) The original DWI acquisitions are interleaved by b-values, looping through the slices (color blocks) and the signal averages (NSAs) first, followed by b-values. d) The modified DWI acquisition is interleaved by signal averages, looping through the slices and b-values first, followed by the signal averages. This minimizes the field-map variations between different b-value images.

The sequence (Figure 8-9) was implemented on a 3T Ingenia scanner (Philips Healthcare, Best, The Netherlands). Phantoms with sucrose concentrations of 0.3, 0.6, 1.2 M

and peanut oil were used to validate the ADC measurements using the hybrid DW-SShTSE-Dixon. The proposed method was evaluated and compared against DW-EPI, DW-SShTSE with SPIR and Dixon in the spinal cord of 3 healthy volunteers with IRB approval and written informed consent. Segmented EPI was used to reduce the geometric distortions. The typical imaging parameters of the proposed sequence included: sagittal orientation; FOV = 220×220 mm; Slice Thickness = 4mm; TE = 70 ms, directions = 3 and  $\delta t = 1.1$  ms. The acquisition voxel size was 2×2 mm and 1.3×1.3 mm for the low and high resolution DWI respectively. The total scan time was approximately 5 and 8 min for the low and high resolution DWI with 13 slices, 3 b-values (e.g. 0, 400 and 800) and 6 NSAs.

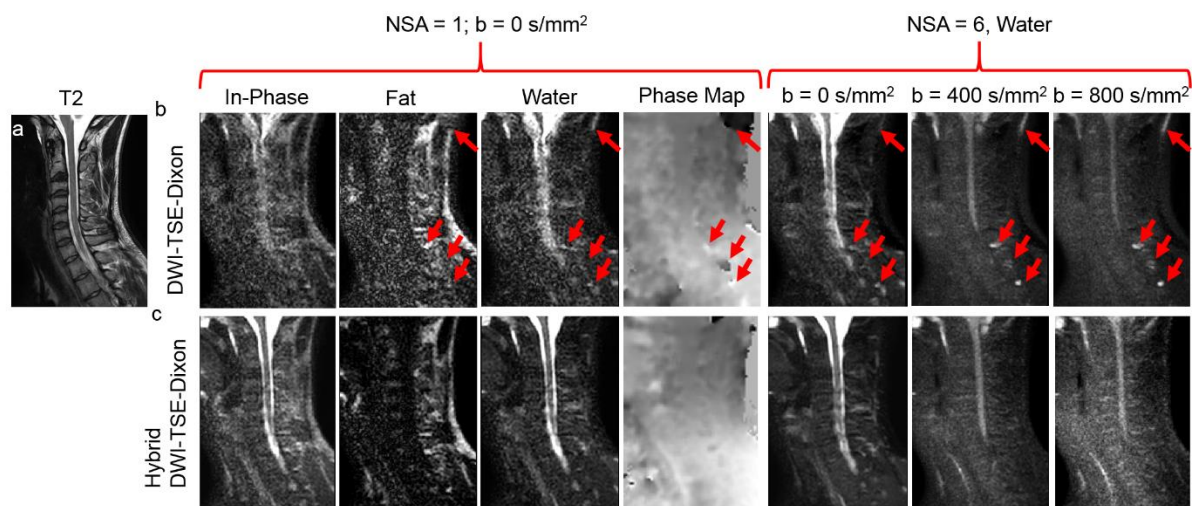
### **8.6.2 Preliminary Imaging Results using Hybrid DWI SShTSE Dixon**

Figure 8-10 demonstrates the correct ADC measurement achieved by the hybrid DW-SShTSE-Dixon using Equation 8.2 with the scaling factor of 2 at  $b = 0$  s/mm<sup>2</sup> (Figure 8-10d). Compared to segmented DW-EPI (Figure 8-10a) and DW-SShTSE with SPIR fat suppression (Figure 8-10b), the proposed hybrid DW-SShTSE-Dixon generated uniform fat suppression and similar ADC map (Figure 8-10c) showing good agreement in ADC values (Figure 8-10e). Figure 8-11 shows improved fat/water separation with the hybrid DW-SShTSE-Dixon compared to the original DW-SShTSE-Dixon. Fat/water swaps, mimicking lesions at higher b-value images were observed in the original DW-SShTSE-Dixon images (Figure 8-11a, red arrows) due to the inaccurate phase estimation at  $b = 0$  s/mm<sup>2</sup>. Uniform fat/water separation was achieved with the proposed hybrid DW-SShTSE-Dixon at  $b = 0$  s/mm<sup>2</sup>, which further improved the fat/water separation at higher b-values with the shared-field-map Dixon reconstruction.



**Figure 8-10 Phantom results and validation of the hybrid DWI-SShTSE Dixon**

The proposed hybrid DW-SShTSE-Dixon (c) achieved uniform fat suppression across all b-values and generated ADC maps that are in good agreement with DW-EPI (a) and DW-SShTSE with SPIR fat suppression (b). Phantoms 1, 2 and 3 were sucrose solutions with concentrations of 1.2, 0.6, and 0.3 M respectively, while the fat phantom was peanut oil. The ADC fitting of an exemplary voxel using Equation 8-2 was shown in d, where the b=0 s/mm<sup>2</sup> value was reduced by half to compensate for the increased signal achieved by the removal of the dephasing gradient. The measured ADC values of all three sucrose phantoms were in good agreement across all sequences (e).



**Figure 8-11 Comparison between DWI-TSE Dixon and hybrid DWI-TSE Dixon**

a) A reference T2-weighted image of the cervical spine. Images acquired with the previously proposed DW-SShTSE-Dixon (b) show low SNR compared to images acquired with the proposed hybrid DW-SShTSE-Dixon. The phase map and standard Dixon reconstruction was performed with  $b=0$  s/mm<sup>2</sup> images. The water images were finally averaged. Residual fat/water swaps (red arrows), mimicking the appearance of lesions were observed in the images acquired with the original DW-SShTSE-Dixon due to low SNR, that were fixed with the proposed hybrid DW-SShTSE-Dixon.

The single-shot DW-EPI suffers from severe geometric distortions (Figure 8-12a), resulting in inaccurate ADC map. DW-SShTSE with SPIR achieved negligible geometric distortion, but suffers from nonuniform fat suppression and low SNR at  $b = 0$  s/mm<sup>2</sup> due to the dephasing gradient (Figure 8-12b). Compared to these techniques, the proposed hybrid DW-SShTSE-Dixon generated high SNR images at  $b = 0$  s/mm<sup>2</sup>, and achieved robust fat/water separation and accurate ADC maps (Figure 8-12c). With the improved SNR at  $b=0$  s/mm<sup>2</sup>, DW-SShTSE-Dixon enables robust fat/water separation and allows high-resolution diffusion weighted images of the cervical spine (Figure 8-13).

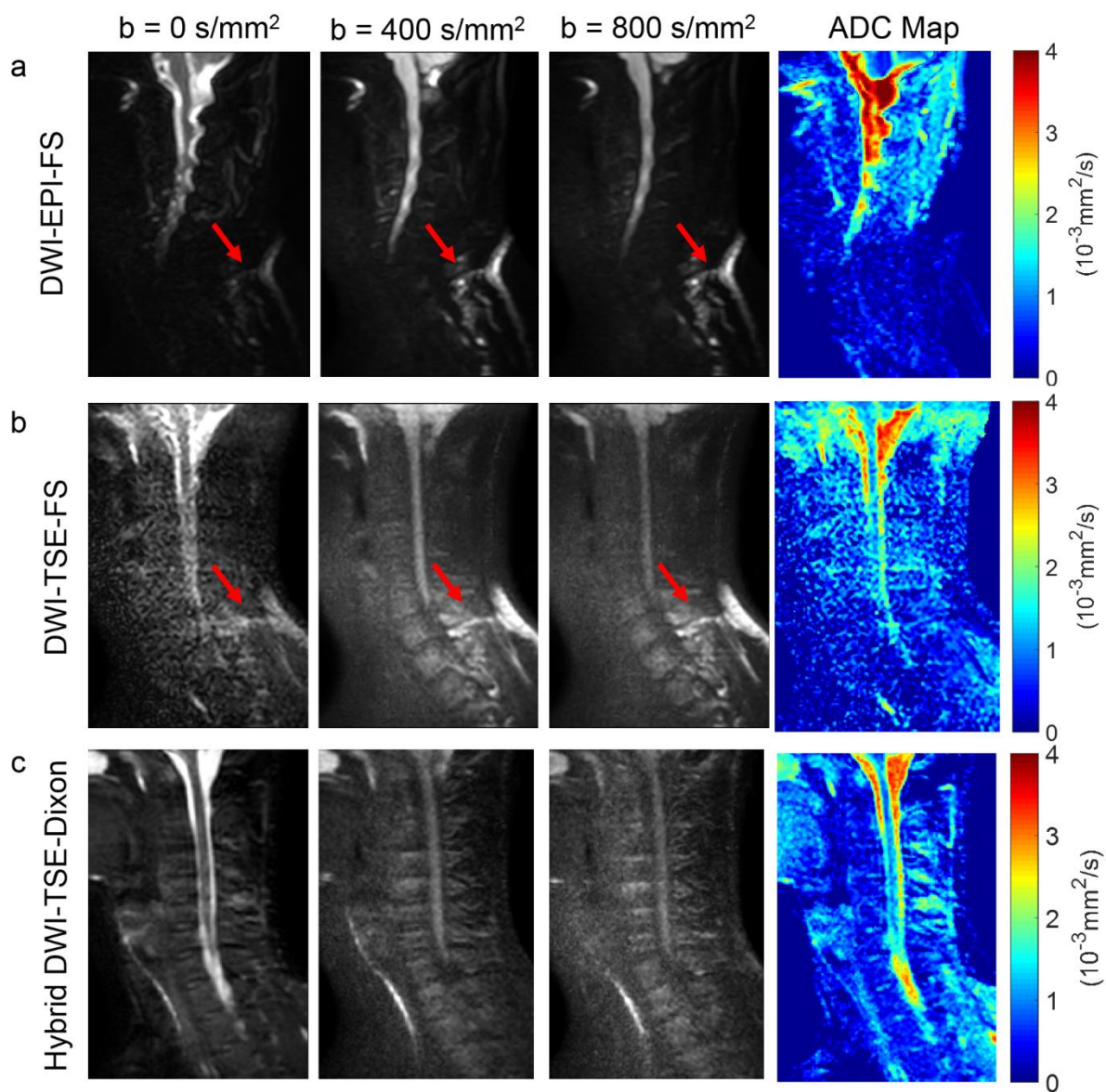


**Figure 8-12 Comparison among hybrid DWI-TSE Dixon, DWI-TSE FS and DWI-EPI FS**

Compared to DW-EPI (a), and DW-SShTSE with SPIR fat suppression (b), the proposed hybrid DW-SShTSE-Dixon (c) achieved uniform fat suppression without geometric distortions across all b-values in the cervical spine. At  $b=0 \text{ s/mm}^2$ , the image acquired with the hybrid DWI-SShTSE-Dixon (c) shows higher SNR compared to that acquired with DW-SShTSE (b). The ADC maps generated with all three sequences showed similar values.

We have demonstrated a hybrid DW-SShTSE-Dixon with shared-field-map to achieve robust diffusion-weighted images with uniform fat/water separation and accurate ADC measurements. This approach allows higher SNR images with negligible geometric distortions that can be used in challenging areas with increased B0 inhomogeneities such as spinal cord imaging and body applications.

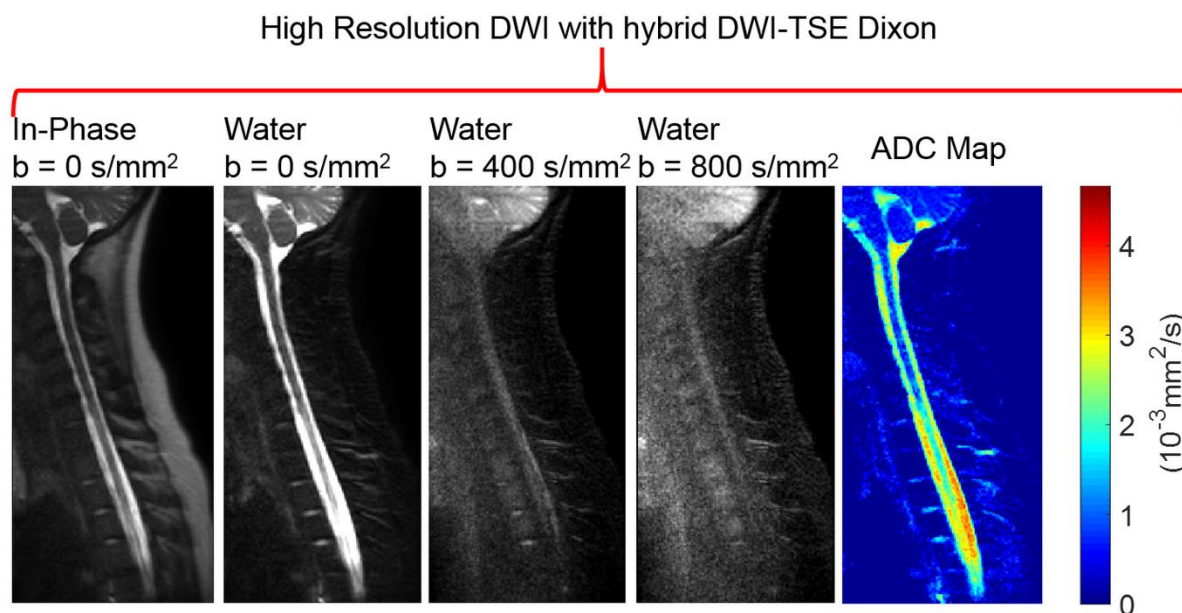


**Figure 8-13 High Resolution DWI of cervical spinal cord with hybrid DWI-TSE Dixon**  
The higher SNR achieved by the proposed hybrid DW-SShTSE-Dixon at  $b=0$  s/mm<sup>2</sup> allows the acquisition of high-resolution (1.3x1.3 mm) diffusion weighted images with good image quality. The ADC map was generated using all three b-values.

## **CHAPTER NINE**

### **Discussion and Conclusion**

T2-weighted MR imaging is a part of almost all MRI protocols due to its excellent soft tissue contrast. However, fat and fluid appear bright in T2w MRI, resulting in additional artifacts, reduced image contrast and sensitivity. Although multiple fat and fluid suppression methods have been proposed with a number of successful clinical applications, the disadvantages of these methods limit their performance in some advanced clinical applications, such as brachial plexus imaging, cervical spine imaging, abdominal imaging and whole-body imaging. The goal of this dissertation was to develop T2-weighted MRI techniques with robust fat and fluid suppressions at 3T for advanced clinical applications with ultimate goal of whole-body MRI with improved lesion conspicuity for metastatic cancer detection. Several T2w MR imaging techniques have been developed and evaluated in advanced clinical applications as a part of this goal.

In chapters 3, the frequency offset corrected inversion (FOCI) pulse based 3D STIR sequence was developed to improve fat suppression and nerve visualization in 3D brachial plexus imaging. Compared to the commonly used hyperbolic secant (HS) pulse, FOCI pulse achieved broader bandwidth at the same adiabatic threshold and lower adiabatic threshold at the same bandwidth, increasing the robustness to  $B_0$  and  $B_1$  inhomogeneities. With a broad bandwidth (2.5 kHz) and low adiabatic threshold (5 uT at 3.5 ppm), FOCI based 3D STIR achieved robust fat suppression in brachial plexus MR neurography.

Although FOCI based STIR demonstrated robust fat suppression, STIR mixes the T1 and T2 contrast and suffers from reduced SNR. To overcome these limitations, a 3D

variable-flip-angle TSE based dual-echo Dixon with partial echo acquisition has been developed in Chapter 4. Dual-echo Dixon showed robust fat suppression as well as improved SNR compared to 3D STIR. Besides brachial plexus imaging, the sequence can also be used for fat-suppressed lumbar plexus imaging in the future. Compared to STIR, the dual-echo Dixon method preserves the T2 contrast and can be used in T2 mapping sequence to quantitatively assess nerve pathology.

Chapter 5 combined the dual-echo Dixon with the dual-echo TSE to simultaneously suppress fat and fluid in multi-contrast cervical spine imaging. Conventional fat/water separation reconstruction methods successfully separated water and fat signals at short TE, while failed at long TE due to low SNR. Shared-field-map Dixon reconstruction was developed to improve the fat suppression in long TE images. The sequence also generated multi-contrast images, including the standard T2w, fat-suppressed T2w, fluid-suppressed T2w, both fat- and fluid-suppressed T2w, heavily T2w and fat-only images in a single acquisition. The volunteer images showed improved SNR and CR, as well as efficient fluid suppression. Further clinical evaluation will be performed in patients.

Chapters 3 – 5 showed multi-shot TSE based fat- and/or fluid-suppressed MR imaging. However, single-shot TSE (SShTSE) is commonly used in body imaging instead of multi-shot TSE due to its increased speed and robustness to respiratory motion. Chapter 6 extended the dual-echo Dixon with partial-echo acquisition to the SShTSE sequence for breathhold abdominal imaging. Compared to the commonly used SPAIR, SShTSE with dual-echo Dixon achieved improved fat suppression without increasing the scan time. However, dual-echo Dixon slightly increased the echo spacing, resulting in image blurring. In the

future, variable refocusing flip angles could be used to improve the in-plane resolution as well as to control image blurring.

Since SShTSE dual-echo Dixon demonstrated robust fat suppression in abdominal imaging, it was then extended to multi-station whole-body MR imaging. However, fat-suppressed whole-body MR images showed less lesion conspicuity compared to DWI due to the presence of high signals from the fluid. Chapter 7 combined the SShTSE dual-echo Dixon with dual-acquisition, and developed a fast, T2w whole-body MR imaging sequence (DETECT) with simultaneous fat and fluid suppression for metastatic cancer detection. The preliminary patient study demonstrated improved image quality and improved sensitivity compared to DW whole-body MRI. In the future, DETECT images will be compared against PET/CT in patients to determine the sensitivity and specificity.

Although DETECT is a promising alternative whole-body MR imaging method to whole-body DWI, it can only provide limited functional information. DWI is still preferred for quantitative evaluation. To reduce the EPI acquisition associated geometric distortions and improve the fat suppression, a SShTSE based DWI sequence with multi-echo Dixon was developed in Chapter 8. The DW imaging of the cervical spinal cord demonstrated robust fat suppression and reduced geometric distortions using the proposed sequence. In the future, the SShTSE based DWI sequence with multi-echo Dixon will be evaluated in patients.

In conclusion, robust fat and fluid suppression methods have been developed and evaluated in several advanced clinical applications (Chapters 3 – 6). Ultimately, whole-body MRI with improved lesion conspicuity has been developed for metastatic cancer detection (Chapter 7). In addition to these anatomical imaging methods, the multi-echo Dixon and

shared-field-map Dixon reconstruction were also extended to DWI for improved fat suppression and reduced geometric distortions, improving the quantitative assessment.

## APPENDIX A

### Adiabatic Threshold of the C-FOCI Pulse

For the effective  $B_1$  of the C-FOCI pulse, the two orthogonal components can be denoted as:

$$F_1(t) = C(t) \times A_0 \operatorname{sech}(\beta t) \quad \text{Equation A.1}$$

$$F_2(t, \Omega) = \frac{1}{\gamma} [-C(t) \times \mu\beta \tanh(\beta t) + \Omega] \quad \text{Equation A.2}$$

where  $F_1$  is in the transverse plane;  $F_2$  is along the longitudinal axis;  $\gamma$  is the gyromagnetic ratio and  $\Omega$  is the off-resonance frequency.

The amplitude and direction of the effective  $B_1$  as seen by an isochromat at offset frequency,  $\Omega$  can be expressed as:

$$|\vec{B}1_{eff}^\Omega| = \sqrt{F_1^2 + F_2^2} \quad \text{Equation A.3}$$

$$\psi = \arctan\left(\frac{F_1}{F_2}\right) \quad \text{Equation A.4}$$

Then the change of rate of the  $B1_{eff}^\Omega$  orientation is

$$\left| \frac{\partial \psi}{\partial t} \right| = \frac{F_2^2}{F_1^2 + F_2^2} \left| \frac{\partial F_1}{\partial t} \frac{1}{F_2} - \frac{\partial F_2}{\partial t} \frac{F_1}{F_2^2} \right| \quad \text{Equation A.5}$$

The adiabatic factor  $\eta$ , which states that  $\eta \gg 1$  to satisfy the adiabatic condition, is given as

$$\eta(t, \Omega) = \left| \frac{\gamma \overline{B_1^\Omega}}{\partial \psi / \partial t} \right| = \left| \frac{\gamma (F_1^2 + F_2^2)^{3/2}}{\frac{\partial F_1}{\partial t} F_2 - \frac{\partial F_2}{\partial t} F_1} \right| \quad \text{Equation A.6}$$

When  $\cosh(\beta t) < C_{max}$ ,  $C(t) = \cosh(\beta t)$ . Within this condition, at specific time,  $t = t_\Omega$ , the isochromat at  $\Omega$  is on resonance and thus  $F_2(t_\Omega) = 0$ . Then,

$$\eta(t_\Omega) = \left| \frac{\gamma (F_1^2 + F_2^2)^{3/2}}{\frac{\partial F_1}{\partial t} F_2 - \frac{\partial F_2}{\partial t} F_1} \right| = \frac{\gamma A_0^3}{A_0 \frac{\mu \beta^2}{\gamma} \cosh(\beta t_\Omega)} \gg 1 \quad \text{Equation A.7}$$

Here,  $A_0$  is noted as  $A_\Omega$ , which stands for the maximum amplitude of the  $B_1$  for an isochromat with off resonance frequency  $\Omega$  to satisfy the adiabatic condition. Then,

$$A_\Omega \gg \frac{\sqrt{\mu} \beta}{\gamma} \sqrt{\cosh(\beta t_\Omega)} \quad \text{Equation A.8}$$

Similarly, when  $C(t) = C_{max}$ ,

$$\eta(t_\Omega) = \frac{\gamma A_\Omega^2 C_{max}}{\frac{\mu \beta^2}{\gamma}} \gg 1 \quad \text{Equation A.9}$$

$$A_\Omega \gg \frac{\sqrt{\mu} \beta}{\gamma \sqrt{C_{max}}} \quad \text{Equation A.10}$$

## BIBLIOGRAPHY

1. Berglund J, Johansson L, Ahlström H, Kullberg J. Three-point dixon method enables whole-body water and fat imaging of obese subjects. *Magn Reson Med* 2010;63(6):1659-1668.
2. Maudsley AA, Domenig C, Govind V, Darkazanli A, Studholme C, Arheart K, Bloomer C. Mapping of brain metabolite distributions by volumetric proton MR spectroscopic imaging (MRSI). *Magnetic Resonance in Medicine: An Official Journal of the International Society for Magnetic Resonance in Medicine* 2009;61(3):548-559.
3. Buxton RB, Frank LR, Wong EC, Siewert B, Warach S, Edelman RR. A general kinetic model for quantitative perfusion imaging with arterial spin labeling. *Magn Reson Med* 1998;40(3):383-396.
4. Ishihara Y, Calderon A, Watanabe H, Okamoto K, Suzuki Y, Kuroda K, Suzuki Y. A precise and fast temperature mapping using water proton chemical shift. *Magn Reson Med* 1995;34(6):814-823.
5. Takahara T, Imai Y, Yamashita T, Yasuda S, Nasu S, Van Cauteren M. Diffusion weighted whole body imaging with background body signal suppression (DWIBS): technical improvement using free breathing, STIR and high resolution 3D display. *Matrix* 2004;160(160):160.
6. Brody AS, Frush DP, Huda W, Brent RL. Radiation risk to children from computed tomography. *Pediatrics* 2007;120(3):677-682.
7. Robbins E. Radiation risks from imaging studies in children with cancer. *Pediatr Blood Cancer* 2008;51(4):453-457.
8. Sodickson A, Baeyens PF, Andriole KP, Prevedello LM, Nawfel RD, Hanson R, Khorasani R. Recurrent CT, cumulative radiation exposure, and associated radiation-induced cancer risks from CT of adults. *Radiology* 2009;251(1):175-184.
9. Plewes DB, Kucharczyk W. Physics of MRI: a primer. *J Magn Reson Imaging* 2012;35(5):1038-1054.
10. Coombs BD, Szumowski J, Coshov W. Two-point Dixon technique for water-fat signal decomposition with B0 inhomogeneity correction. *Magn Reson Med* 1997;38(6):884-889.

11. Stanisz GJ, Odobina EE, Pun J, Escaravage M, Graham SJ, Bronskill MJ, Henkelman RM. T1, T2 relaxation and magnetization transfer in tissue at 3T. *Magn Reson Med* 2005;54(3):507-512.
12. De Bazelaire CM, Duhamel GD, Rofsky NM, Alsop DC. MR imaging relaxation times of abdominal and pelvic tissues measured in vivo at 3.0 T: preliminary results. *Radiology* 2004;230(3):652-659.
13. Hardy PA, Henkelman RM, Bishop JE, Poon ECS, Plewes DB. Why fat is bright in rare and fast spin-echo imaging. *J Magn Reson Imaging* 1992;2(5):533-540.
14. Qin Q. A simple approach for three-dimensional mapping of baseline cerebrospinal fluid volume fraction. *Magn Reson Med* 2011;65(2):385-391.
15. Delfaut EM, Beltran J, Johnson G, Rousseau J, Marchandise X, Cotten A. Fat suppression in MR imaging: techniques and pitfalls. *Radiographics* 1999;19(2):373-382.
16. De Coene B, Hajnal JV, Gatehouse P, Longmore DB, White SJ, Oatridge A, Pennock J, Young I, Bydder G. MR of the brain using fluid-attenuated inversion recovery (FLAIR) pulse sequences. *Am J Neuroradiol* 1992;13(6):1555-1564.
17. Jackson A, Sheppard S, Laitt RD, Kassner A, Moriarty D. Optic neuritis: MR imaging with combined fat-and water-suppression techniques. *Radiology* 1998;206(1):57-63.
18. Yoo HJ, Hong SH, Oh HY, Choi J-Y, Chae HD, Ahn JM, Kang HS. Diagnostic Accuracy of a Fluid-attenuated Inversion-Recovery Sequence with Fat Suppression for Assessment of Peripatellar Synovitis: Preliminary Results and Comparison with Contrast-enhanced MR Imaging. *Radiology* 2016:160155.
19. Del Grande F, Santini F, Herzka DA, Aro MR, Dean CW, Gold GE, Carrino JA. Fat-suppression techniques for 3-T MR imaging of the musculoskeletal system. *Radiographics* 2014;34(1):217-233.
20. Chien D, Kwong KK, Gress DR, Buonanno FS, Buxton RB, Rosen BR. MR diffusion imaging of cerebral infarction in humans. *Am J Neuroradiol* 1992;13(4):1097-1102.
21. Koh D-M, Blackledge M, Padhani AR, Takahara T, Kwee TC, Leach MO, Collins DJ. Whole-body diffusion-weighted MRI: tips, tricks, and pitfalls. *Am J Roentgenol* 2012;199(2):252-262.
22. Saritas EU, Cunningham CH, Lee JH, Han ET, Nishimura DG. DWI of the spinal cord with reduced FOV single-shot EPI. *Magnetic Resonance in Medicine: An*

- Official Journal of the International Society for Magnetic Resonance in Medicine  
2008;60(2):468-473.
23. Abragam A, Abragam A. The principles of nuclear magnetism: Oxford university press; 1961.
  24. Liang Z-P, Lauterbur PC. Principles of magnetic resonance imaging: a signal processing perspective: SPIE Optical Engineering Press; 2000.
  25. Reeder SB, Cruite I, Hamilton G, Sirlin CB. Quantitative assessment of liver fat with magnetic resonance imaging and spectroscopy. *J Magn Reson Imaging* 2011;34(4):729-749.
  26. Ren J, Dimitrov I, Sherry AD, Malloy CR. Composition of adipose tissue and marrow fat in humans by <sup>1</sup>H NMR at 7 Tesla. *J Lipid Res* 2008;49(9):2055-2062.
  27. Gold GE, Han E, Stainsby J, Wright G, Brittain J, Beaulieu C. Musculoskeletal MRI at 3.0 T: relaxation times and image contrast. *Am J Roentgenol* 2004;183(2):343-351.
  28. Liberman G, Louzoun Y, Ben Bashat D. T1 mapping using variable flip angle SPGR data with flip angle correction. *J Magn Reson Imaging* 2014;40(1):171-180.
  29. Chen L, Bernstein M, Huston J, Fain S. Measurements of T1 relaxation times at 3.0 T: implications for clinical MRA. 2001.
  30. Bydder G, Young I. MR imaging: clinical use of the inversion recovery sequence. 1985.
  31. Haase A, Frahm J, Hanicke W, Matthaei D. <sup>1</sup>H NMR chemical shift selective (CHESS) imaging. *Phys Med Biol* 1985;30(4):341.
  32. Oh C. Selective partial inversion recovery (SPIR) in steady state for selective saturation magnetic resonance imaging (MRI). *Abstr of Society of Magnetic Resonance in Medicine, San Francisco* 1988;1042.
  33. Lauenstein TC, Sharma P, Hughes T, Heberlein K, Tudorascu D, Martin DR. Evaluation of optimized inversion-recovery fat-suppression techniques for T2-weighted abdominal MR imaging. *J Magn Reson Imaging* 2008;27(6):1448-1454.
  34. Meyer CH, Pauly JM, Macovski A, Nishimura DG. Simultaneous spatial and spectral selective excitation. *Magn Reson Med* 1990;15(2):287-304.
  35. Hors P. A new method for water suppression in the proton NMR spectra of aqueous solutions. *Journal of Magnetic Resonance (1969)* 1983;54(3):539-542.

36. Morrell GR. Rapid fat suppression in MRI of the breast with short binomial pulses. *J Magn Reson Imaging* 2006;24(5):1172-1176.
37. Dixon WT. Simple proton spectroscopic imaging. *Radiology* 1984;153(1):189-194.
38. Reeder SB, Pineda AR, Wen Z, Shimakawa A, Yu H, Brittain JH, Gold GE, Beaulieu CH, Pelc NJ. Iterative decomposition of water and fat with echo asymmetry and least-squares estimation (IDEAL): application with fast spin-echo imaging. *Magn Reson Med* 2005;54(3):636-644.
39. Ma J, Son JB, Zhou Y, Le-Petross H, Choi H. Fast spin-echo triple-echo dixon (fTED) technique for efficient T2-weighted water and fat imaging. *Magn Reson Med* 2007;58(1):103-109.
40. Eggers H, Brendel B, Duijndam A, Herigault G. Dual-echo Dixon imaging with flexible choice of echo times. *Magn Reson Med* 2011;65(1):96-107.
41. Hernando D, Kellman P, Haldar J, Liang ZP. Robust water/fat separation in the presence of large field inhomogeneities using a graph cut algorithm. *Magn Reson Med* 2010;63(1):79-90.
42. Ma J, Son JB, Hazle JD. An improved region growing algorithm for phase correction in MRI. *Magn Reson Med* 2016;76(2):519-529.
43. Stinson EG, Trzasko JD, Fletcher JG, Riederer SJ. Dual echo Dixon imaging with a constrained phase signal model and graph cuts reconstruction. *Magn Reson Med* 2017;78(6):2203-2215.
44. Berglund J, Ahlström H, Johansson L, Kullberg J. Two-point dixon method with flexible echo times. *Magn Reson Med* 2011;65(4):994-1004.
45. Rydberg JN, Riederer SJ, Rydberg CH, Jack CR. Contrast optimization of fluid-attenuated inversion recovery (FLAIR) imaging. *Magn Reson Med* 1995;34(6):868-877.
46. Essig M, Deimling M, Hawighorst H, Debus J, van Kaick G. Assessment of cerebral gliomas by a new dark fluid sequence, high intensity REduction (HIRE): a preliminary study. *J Magn Reson Imaging* 2000;11(5):506-517.
47. Deimling M KR. HIRE (high intensity reduction), a new dark fluid sequence. 1996; New York. p 557.

48. Park J, Park S, Yeop Kim E, Suh JS. Phase-sensitive, dual-acquisition, single-slab, 3D, turbo-spin-echo pulse sequence for simultaneous T2-weighted and fluid-attenuated whole-brain imaging. *Magn Reson Med* 2010;63(5):1422-1430.
49. Chhabra A, Thawait G, Soldatos T, Thakkar R, Del Grande F, Chalian M, Carrino J. High-resolution 3T MR neurography of the brachial plexus and its branches, with emphasis on 3D imaging. *Am J Neuroradiol* 2013;34(3):486-497.
50. Bley TA, Wieben O, François CJ, Brittain JH, Reeder SB. Fat and water magnetic resonance imaging. *J Magn Reson Imaging* 2010;31(1):4-18.
51. Reeder SB, Yu H, Johnson JW, Shimakawa A, Brittain JH, Pelc NJ, Beaulieu CF, Gold GE. T1-and T2-weighted fast spin-echo imaging of the brachial plexus and cervical spine with IDEAL water-fat separation. *J Magn Reson Imaging* 2006;24(4):825-832.
52. Vargas MI, Gariani J, Delattre BA, Dietemann J-L, Lovblad K, Becker M. Three-dimensional MR imaging of the brachial plexus. 2015. Thieme Medical Publishers. p 137-148.
53. Tagliafico A, Bignotti B, Tagliafico G, Martinoli C. Usefulness of IDEAL T2 imaging for homogeneous fat suppression and reducing susceptibility artefacts in brachial plexus MRI at 3.0 T. *Radiol Med* 2016;121(1):45-53.
54. Madhuranthakam AJ, Yu H, Shimakawa A, Busse RF, Smith MP, Reeder SB, Rofsky NM, Brittain JH, McKenzie CA. T2-weighted 3D fast spin echo imaging with water-fat separation in a single acquisition. *J Magn Reson Imaging* 2010;32(3):745-751.
55. Chalian M, Faridian-Aragh N, Soldatos T, Batra K, Belzberg AJ, Williams EH, Carrino JA, Chhabra A. High-resolution 3T MR neurography of suprascapular neuropathy. *Acad Radiol* 2011;18(8):1049-1059.
56. Tagliafico A, Succio G, Neumaier C, Baio G, Serafini G, Ghidara M, Calabrese M, Martinoli C. Brachial plexus assessment with three-dimensional isotropic resolution fast spin echo MRI: comparison with conventional MRI at 3.0 T. *The British journal of radiology* 2012;85(1014):e110-e116.
57. Wang X, Harrison C, Mariappan YK, Gopalakrishnan K, Chhabra A, Lenkinski RE, Madhuranthakam AJ. MR Neurography of Brachial Plexus at 3.0 T with Robust Fat and Blood Suppression. *Radiology* 2016;283(2):538-546.
58. Brandão S, Seixas D, Ayres-Basto M, Castro S, Neto J, Martins C, Ferreira J, Parada F. Comparing T1-weighted and T2-weighted three-point Dixon technique with conventional T1-weighted fat-saturation and short-tau inversion recovery

- (STIR) techniques for the study of the lumbar spine in a short-bore MRI machine. *Clin Radiol* 2013;68(11):e617-e623.
59. Silver M, Joseph R, Hoult D. Highly selective  $\pi/2$  and  $\pi$  pulse generation. *Journal of Magnetic Resonance* (1969) 1984;59(2):347-351.
  60. Bernstein MA, King KF, Zhou XJ. *Handbook of MRI pulse sequences*: Elsevier; 2004.
  61. Ordidge RJ, Wylezinska M, Hugg JW, Butterworth E, Franconi F. Frequency offset corrected inversion (FOCI) pulses for use in localized spectroscopy. *Magn Reson Med* 1996;36(4):562-566.
  62. Tesiram YA. Implementation equations for HSn RF pulses. *J Magn Reson* 2010;204(2):333-339.
  63. Wells J, Siow B, Lythgoe M, Thomas D. The importance of RF bandwidth for effective tagging in pulsed arterial spin labeling MRI at 9.4 T. *NMR Biomed* 2012;25(10):1139-1143.
  64. Silver M, Joseph R, Hoult D. Selective spin inversion in nuclear magnetic resonance and coherent optics through an exact solution of the Bloch-Riccati equation. *Physical Review A* 1985;31(4):2753.
  65. Cunningham CH, Pauly JM, Nayak KS. Saturated double-angle method for rapid B1+ mapping. *Magn Reson Med* 2006;55(6):1326-1333.
  66. Zhang J, Garwood M, Park JY. Full analytical solution of the Bloch equation when using a hyperbolic-secant driving function. *Magn Reson Med* 2017;77(4):1630-1638.
  67. Truong T-K, Clymer BD, Chakeres DW, Schmalbrock P. Three-dimensional numerical simulations of susceptibility-induced magnetic field inhomogeneities in the human head. *Magn Reson Imaging* 2002;20(10):759-770.
  68. Boer VO, Klomp DW, Juchem C, Luijten PR, de Graaf RA. Multislice 1H MRSI of the human brain at 7 T using dynamic B0 and B1 shimming. *Magn Reson Med* 2012;68(3):662-670.
  69. Yongbi MN, Branch CA, Helpert JA. Perfusion imaging using FOCI RF pulses. *Magn Reson Med* 1998;40(6):938-943.
  70. Hurley AC, Al-Radaideh A, Bai L, Aickelin U, Coxon R, Glover P, Gowland PA. Tailored RF pulse for magnetization inversion at ultrahigh field. *Magn Reson Med* 2010;63(1):51-58.

71. Warnking JM, Pike GB. Bandwidth-modulated adiabatic RF pulses for uniform selective saturation and inversion. *Magn Reson Med* 2004;52(5):1190-1199.
72. Gerevini S, Agosta F, Riva N, Spinelli EG, Pagani E, Caliendo G, Chaabane L, Copetti M, Quattrini A, Comi G. MR Imaging of Brachial Plexus and Limb-Girdle Muscles in Patients with Amyotrophic Lateral Sclerosis. *Radiology* 2015;279(2):553-561.
73. Madhuranthakam AJ, Lenkinski RE. Technical advancements in MR neurography. *Seminars in musculoskeletal radiology* 2015;19(2):86-93.
74. Vargas MI, Viallon M, Nguyen D, Beaulieu JY, Delavelle J, Becker M. New approaches in imaging of the brachial plexus. *Eur J Radiol* 2010;74(2):403-410.
75. Baumer P, Kele H, Kretschmer T, Koenig R, Pedro M, Bendszus M, Pham M. Thoracic outlet syndrome in 3T MR neurography-fibrous bands causing discernible lesions of the lower brachial plexus. *Eur Radiol* 2014;24(3):756-761.
76. Reeder SB, Yu H, Johnson JW, Shimakawa A, Brittain JH, Pelc NJ, Beaulieu CF, Gold GE. T1- and T2-weighted fast spin-echo imaging of the brachial plexus and cervical spine with IDEAL water-fat separation. *J Magn Reson Imaging* 2006;24(4):825-832.
77. Lichy MP, Wietek BM, Mugler JP, 3rd, Horger W, Menzel MI, Anastasiadis A, Siegmann K, Niemeyer T, Konigsrainer A, Kiefer B, Schick F, Claussen CD, Schlemmer HP. Magnetic resonance imaging of the body trunk using a single-slab, 3-dimensional, T2-weighted turbo-spin-echo sequence with high sampling efficiency (SPACE) for high spatial resolution imaging: initial clinical experiences. *Invest Radiol* 2005;40(12):754-760.
78. Busse RF, Brau AC, Vu A, Michelich CR, Bayram E, Kijowski R, Reeder SB, Rowley HA. Effects of refocusing flip angle modulation and view ordering in 3D fast spin echo. *Magn Reson Med* 2008;60(3):640-649.
79. Madhuranthakam AJ, Yu H, Shimakawa A, Busse RF, Smith MP, Reeder SB, Rofsky NM, Brittain JH, McKenzie CA. T<sub>2</sub>-weighted 3D fast spin echo imaging with water-fat separation in a single acquisition. *J Magn Reson Imaging* 2010;32(3):745-751.
80. McMahon CJ, Madhuranthakam AJ, Wu JS, Yablon CM, Wei JL, Rofsky NM, Hochman MG. High-resolution proton density weighted three-dimensional fast spin echo (3D-FSE) of the knee with IDEAL at 1.5 Tesla: comparison with 3D-FSE and 2D-FSE--initial experience. *J Magn Reson Imaging* 2012;35(2):361-369.

81. Hardy PA, Hinks RS, Tkach JA. Separation of fat and water in fast spin-echo MR imaging with the three-point Dixon technique. *J Magn Reson Imaging* 1995;5(2):181-185.
82. Ma J, Son JB, Zhou Y, Le-Petross H, Choi H. Fast spin-echo triple-echo dixon (fTED) technique for efficient T2-weighted water and fat imaging. *Magn Reson Med* 2007;58(1):103-109.
83. Noll DC, Nishimura DG, Macovski A. Homodyne detection in magnetic resonance imaging. *IEEE Trans Med Imaging* 1991;10(2):154-163.
84. Foo TK, Polzin JA; System and method of phase sensitive MRI reconstruction using partial k-space data and including a network. USA patent 6,198,283 B1. 2001.
85. Eggers H, Brendel B, Duijndam A, Herigault G. Dual-echo Dixon imaging with flexible choice of echo times. *Magn Reson Med* 2011;65(1):96-107.
86. Chin EE, Zimmerman PT, Grant EG. Sonographic evaluation of upper extremity deep venous thrombosis. *Journal of ultrasound in medicine : official journal of the American Institute of Ultrasound in Medicine* 2005;24(6):829-838; quiz 839-840.
87. Chhabra A, Thawait GK, Soldatos T, Thakkar RS, Del Grande F, Chalian M, Carrino JA. High-resolution 3T MR neurography of the brachial plexus and its branches, with emphasis on 3D imaging. *AJNR Am J Neuroradiol* 2013;34(3):486-497.
88. Soldatos T, Andreisek G, Thawait GK, Guggenberger R, Williams EH, Carrino JA, Chhabra A. High-resolution 3-T MR neurography of the lumbosacral plexus. *Radiographics* 2013;33(4):967-987.
89. Chhabra A, Soldatos T, Subhawong TK, Machado AJ, Thawait SK, Wang KC, Padua A, Flammang AJ, Williams EH, Carrino JA. The application of three-dimensional diffusion-weighted PSIF technique in peripheral nerve imaging of the distal extremities. *J Magn Reson Imaging* 2011;34(4):962-967.
90. Murtz P, Kaschner M, Lakghomi A, Gieseke J, Willinek WA, Schild HH, Thomas D. Diffusion-weighted MR neurography of the brachial and lumbosacral plexus: 3.0 T versus 1.5 T imaging. *Eur J Radiol* 2015;84(4):696-702.
91. Wang J, Yarnykh VL, Hatsukami T, Chu B, Balu N, Yuan C. Improved suppression of plaque-mimicking artifacts in black-blood carotid atherosclerosis imaging using a multislice motion-sensitized driven-equilibrium (MSDE) turbo spin-echo (TSE) sequence. *Magn Reson Med* 2007;58(5):973-981.

92. McKinney AM, Lohman BD, Sarikaya B, Benson M, Lee MS, Benson MT. Accuracy of routine fat-suppressed FLAIR and diffusion-weighted images in detecting clinically evident acute optic neuritis. *Acta Radiol* 2013;54(4):455-461.
93. Tschampa HJ, Urbach H, Malter M, Surges R, Greschus S, Gieseke J. Magnetic resonance imaging of focal cortical dysplasia: comparison of 3D and 2D fluid attenuated inversion recovery sequences at 3T. *Epilepsy Res* 2015;116:8-14.
94. Mascalchi M, Bianchi A, Basile M, Gulino P, Trifan M, Difeo D, Bartolini E, Defilippi C, Diciotti S. Effectiveness of 3D T2-Weighted FLAIR FSE Sequences with Fat Suppression for Detection of Brain MR Imaging Signal Changes in Children. *Am J Neuroradiol* 2016;37(12):2376-2381.
95. Listerud J, Mitchell J, Bagley L, Grossman R. OIL FLAIR: Optimized interleaved fluid-attenuated inversion recovery in 2D fast spin echo. *Magn Reson Med* 1996;36(2):320-325.
96. Lee H, Sohn CH, Park J. Rapid hybrid encoding for high-resolution whole-brain fluid-attenuated imaging. *NMR Biomed* 2013;26(12):1751-1761.
97. Wang X, Harrison C, Mariappan YK, Gopalakrishnan K, Chhabra A, Lenkinski RE, Madhuranthakam AJ. MR Neurography of Brachial Plexus at 3.0 T with Robust Fat and Blood Suppression. *Radiology* 2016:152842.
98. Vis J, Zwanenburg J, Kleij L, Spijkerman J, Biessels G, Hendrikse J, Petersen E. Cerebrospinal fluid volumetric MRI mapping as a simple measurement for evaluating brain atrophy. *Eur Radiol* 2016;26(5):1254-1262.
99. Yoo H-M, Kim S, Choi C, Lee D, Lee J, Suh D, Choi J, Jeong K, Chung S, Kim JS. Detection of CSF leak in spinal CSF leak syndrome using MR myelography: correlation with radioisotope cisternography. *Am J Neuroradiol* 2008;29(4):649-654.
100. Mirowitz S, Apicella P, Reinus W, Hammerman A. MR imaging of bone marrow lesions: relative conspicuousness on T1-weighted, fat-suppressed T2-weighted, and STIR images. *AJR American journal of roentgenology* 1994;162(1):215-221.
101. Zajick Jr DC, Morrison WB, Schweitzer ME, Parellada JA, Carrino JA. Benign and Malignant Processes: Normal Values and Differentiation with Chemical Shift MR Imaging in Vertebral Marrow 1. *Radiology* 2005;237(2):590-596.
102. Mugler JP. Optimized three-dimensional fast-spin-echo MRI. *J Magn Reson Imaging* 2014;39(4):745-767.

103. Neubert A, Fripp J, Engstrom C, Walker D, Weber M, Schwarz R, Crozier S. Three-dimensional morphological and signal intensity features for detection of intervertebral disc degeneration from magnetic resonance images. *J Am Med Inform Assoc* 2013;20(6):1082-1090.
104. Miyazaki T, Yamashita Y, Tsuchigame T, Yamamoto H, Urata J, Takahashi M. MR cholangiopancreatography using HASTE (half-Fourier acquisition single-shot turbo spin-echo) sequences. *AJR American journal of roentgenology* 1996;166(6):1297-1303.
105. Aerts P, Van Hoe L, Bosmans H, Oyen R, Marchal G, Baert A. Breath-hold MR urography using the HASTE technique. *AJR American journal of roentgenology* 1996;166(3):543-545.
106. Tang Y, Yamashita Y, Namimoto T, Abe Y, Takahashi M. Liver T2-weighted MR imaging: comparison of fast and conventional half-Fourier single-shot turbo spin-echo, breath-hold turbo spin-echo, and respiratory-triggered turbo spin-echo sequences. *Radiology* 1997;203(3):766-772.
107. Klessen C, Asbach P, Kroencke TJ, Fischer T, Warmuth C, Stemmer A, Hamm B, Taupitz M. Magnetic resonance imaging of the upper abdomen using a free-breathing T2-weighted turbo spin echo sequence with navigator triggered prospective acquisition correction. *J Magn Reson Imaging* 2005;21(5):576-582.
108. Henzler T, Dietrich O, Krissak R, Wichmann T, Lanz T, Reiser MF, Schoenberg SO, Fink C. Half-fourier-acquisition single-shot turbo spin-echo (HASTE) MRI of the lung at 3 Tesla using parallel imaging with 32-receiver channel technology. *J Magn Reson Imaging* 2009;30(3):541-546.
109. Lu D, Saini S, Hahn P, Goldberg M, Lee M, Weissleder R, Gerard B, Halpern E, Cats A. T2-weighted MR imaging of the upper part of the abdomen: should fat suppression be used routinely? *AJR American journal of roentgenology* 1994;162(5):1095-1100.
110. Kanematsu M, Hoshi H, Itoh K, Murakami T, Hori M, Kondo H, Yokoyama R, Nakamura H. Focal hepatic lesion detection: comparison of four fat-suppressed T2-weighted MR imaging pulse sequences. *Radiology* 1999;211(2):363-371.
111. Chavhan GB, Babyn PS, Vasanaawala SS. Abdominal MR imaging in children: motion compensation, sequence optimization, and protocol organization. *Radiographics* 2013;33(3):703-719.
112. Ma J. Breath-hold water and fat imaging using a dual-echo two-point dixon technique with an efficient and robust phase-correction algorithm. *Magn Reson Med* 2004;52(2):415-419.

113. Low RN, Ma J, Panchal N. Fast spin-echo triple-echo Dixon: Initial clinical experience with a novel pulse sequence for fat-suppressed T2-weighted abdominal MR imaging. *J Magn Reson Imaging* 2009;30(3):569-577.
114. Polzin JA, Bernstein MA, Foo TK. MRI reconstruction using partial echo and partial NEX data acquisitions. Google Patents; 2000.
115. Dietrich O, Raya JG, Reeder SB, Reiser MF, Schoenberg SO. Measurement of signal-to-noise ratios in MR images: Influence of multichannel coils, parallel imaging, and reconstruction filters. *J Magn Reson Imaging* 2007;26(2):375-385.
116. Xu Y, Haacke EM. Partial Fourier imaging in multi-dimensions: A means to save a full factor of two in time. *J Magn Reson Imaging* 2001;14(5):628-635.
117. Paul JS, Pillai UKS. A higher dimensional homodyne filter for phase sensitive partial Fourier reconstruction of magnetic resonance imaging. *Magn Reson Imaging* 2015;33(9):1114-1125.
118. Reeder SB, McKenzie CA, Pineda AR, Yu H, Shimakawa A, Brau AC, Hargreaves BA, Gold GE, Brittain JH. Water-fat separation with IDEAL gradient-echo imaging. *J Magn Reson Imaging* 2007;25(3):644-652.
119. Loening AM, Saranathan M, Ruangwattanapaisarn N, Litwiller DV, Shimakawa A, Vasanawala SS. Increased speed and image quality in single-shot fast spin echo imaging via variable refocusing flip angles. *J Magn Reson Imaging* 2015;42(6):1747-1758.
120. Antoch G, Saoudi N, Kuehl H, Dahmen G, Mueller SP, Beyer T, Bockisch A, Debatin JF, Freudenberg LS. Accuracy of whole-body dual-modality fluorine-18-2-fluoro-2-deoxy-D-glucose positron emission tomography and computed tomography (FDG-PET/CT) for tumor staging in solid tumors: comparison with CT and PET. *J Clin Oncol* 2004;22(21):4357-4368.
121. Schöder H, Gönen M. Screening for cancer with PET and PET/CT: potential and limitations. *J Nucl Med* 2007;48(1 suppl):4S-18S.
122. Hall E, Brenner D. Cancer risks from diagnostic radiology. *Br J Radiol* 2008;81(965):362-378.
123. Klenk C, Gawande R, Uslu L, Khurana A, Qiu D, Quon A, Donig J, Rosenberg J, Luna-Fineman S, Moseley M. Ionising radiation-free whole-body MRI versus 18 F-fluorodeoxyglucose PET/CT scans for children and young adults with cancer: a prospective, non-randomised, single-centre study. *Lancet Oncol* 2014;15(3):275-285.

124. Park J-W, Kim JH, Kim SK, Kang KW, Park KW, Choi J-I, Lee WJ, Kim C-M, Nam BH. A prospective evaluation of 18F-FDG and 11C-acetate PET/CT for detection of primary and metastatic hepatocellular carcinoma. *J Nucl Med* 2008;49(12):1912-1921.
125. Nomori H, Watanabe K, Ohtsuka T, Naruke T, Suemasu K, Uno K. Evaluation of F-18 fluorodeoxyglucose (FDG) PET scanning for pulmonary nodules less than 3 cm in diameter, with special reference to the CT images. *Lung Cancer* 2004;45(1):19-27.
126. Kim SM, Cha R-h, Lee JP, Kim DK, Oh K-H, Joo KW, Lim CS, Kim S, Kim YS. Incidence and outcomes of contrast-induced nephropathy after computed tomography in patients with CKD: a quality improvement report. *Am J Kidney Dis* 2010;55(6):1018-1025.
127. Schmidt GP, Reiser MF, Baur-Melnyk A. Whole-body MRI for the staging and follow-up of patients with metastasis. *Eur J Radiol* 2009;70(3):393-400.
128. Takenaka D, Ohno Y, Matsumoto K, Aoyama N, Onishi Y, Koyama H, Nogami M, Yoshikawa T, Matsumoto S, Sugimura K. Detection of bone metastases in non-small cell lung cancer patients: Comparison of whole-body diffusion-weighted imaging (DWI), whole-body MR imaging without and with DWI, whole-body FDG-PET/CT, and bone scintigraphy. *J Magn Reson Imaging* 2009;30(2):298-308.
129. Kwee TC, Takahara T, Ochiai R, Nievelstein RA, Luijten PR. Diffusion-weighted whole-body imaging with background body signal suppression (DWIBS): features and potential applications in oncology. *Eur Radiol* 2008;18(9):1937-1952.
130. Eiber M, Holzapfel K, Ganter C, Epple K, Metz S, Geinitz H, Kübler H, Gaa J, Rummeny EJ, Beer AJ. Whole-body MRI including diffusion-weighted imaging (DWI) for patients with recurring prostate cancer: Technical feasibility and assessment of lesion conspicuity in DWI. *J Magn Reson Imaging* 2011;33(5):1160-1170.
131. Walker R, Kessar P, Blanchard R, Dimasi M, Harper K, DeCarvalho V, Yucel E, Patriquin L, Eustace S. Turbo STIR magnetic resonance imaging as a whole-body screening tool for metastases in patients with breast carcinoma: Preliminary clinical experience. *J Magn Reson Imaging* 2000;11(4):343-350.
132. Punwani S, Taylor SA, Bainbridge A, Prakash V, Bandula S, De Vita E, Olsen OE, Hain SF, Stevens N, Daw S. Pediatric and Adolescent Lymphoma: Comparison of Whole-Body STIR Half-Fourier RARE MR Imaging with an Enhanced PET/CT Reference for Initial Staging 1. *Radiology* 2010;255(1):182-190.

133. Schwartz L, Seltzer S, Tempany C, Silverman S, Piwnica-Worms D, Adams D, Herman L, Herman L, Hooshmand R. Prospective comparison of T2-weighted fast spin-echo, with and without fat suppression, and conventional spin-echo pulse sequences in the upper abdomen. *Radiology* 1993;189(2):411-416.
134. Jackson A, Sheppard S, Johnson AC, Annesley D, Laitt RD, Kassner A. Combined fat-and water-suppressed MR imaging of orbital tumors. *Am J Neuroradiol* 1999;20(10):1963-1969.
135. Wang X, Greer JS, Pedrosa I, Rofsky NM, Madhuranthakam AJ. Robust abdominal imaging with uniform fat suppression using Dixon based single shot turbo spin echo. In Proceedings of the 24th Annual Meeting of ISMRM. Singapore2016. p 0573.
136. Madhuranthakam AJ, Lee KS, Yassin A, Brittain JH, Pedrosa I, Rofsky NM, Alsop DC. Improved short tau inversion recovery (iSTIR) for increased tumor conspicuity in the abdomen. *Magn Reson Mater Phy* 2014;27(3):245-255.
137. Wang X, Greer JS, Pinho MC, Lenkinski RE, Madhuranthakam AJ. Volumetric T2-weighted and FLAIR Imaging of Spine with Uniform Fat Suppression in a Single Acquisition. In Proceedings of the 25th Annual Meeting of ISMRM. Honolulu, Hawaii, USA2017. p 0191.
138. Busse RF, Brau A, Vu A, Michelich CR, Bayram E, Kijowski R, Reeder SB, Rowley HA. Effects of refocusing flip angle modulation and view ordering in 3D fast spin echo. *Magn Reson Med* 2008;60(3):640-649.
139. Sarkar SN, Alsop DC, Madhuranthakam AJ, Busse RF, Robson PM, Rofsky NM, Hackney DB. Brain MR imaging at ultra-low radiofrequency power. *Radiology* 2011;259(2):550-557.
140. Smith SA, Edden RA, Farrell JA, Barker PB, Van Zijl P. Measurement of T1 and T2 in the cervical spinal cord at 3 tesla. *Magn Reson Med* 2008;60(1):213-219.
141. Badve C, Yu A, Dastmalchian S, Rogers M, Ma D, Jiang Y, Margevicius S, Pahwa S, Lu Z, Schluchter M. MR Fingerprinting of Adult Brain Tumors: Initial Experience. *Am J Neuroradiol* 2017;38(3):492-499.
142. Inada Y, Matsuki M, Nakai G, Tatsugami F, Tanikake M, Narabayashi I, Yamada T, Tsuji M. Body diffusion-weighted MR imaging of uterine endometrial cancer: is it helpful in the detection of cancer in nonenhanced MR imaging? *Eur J Radiol* 2009;70(1):122-127.
143. Padhani AR, Koh D-M, Collins DJ. Whole-body diffusion-weighted MR imaging in cancer: current status and research directions. *Radiology* 2011;261(3):700-718.

144. Lavdas I, Rockall AG, Castelli F, Sandhu RS, Papadaki A, Honeyfield L, Waldman AD, Aboagye EO. Apparent diffusion coefficient of normal abdominal organs and bone marrow from whole-Body DWI at 1.5 T: the effect of sex and age. *Am J Roentgenol* 2015;205(2):242-250.
145. Jambor I, Kuisma A, Ramadan S, Huovinen R, Sandell M, Kajander S, Kemppainen J, Kauppila E, Auren J, Merisaari H. Prospective evaluation of planar bone scintigraphy, SPECT, SPECT/CT, 18F-NaF PET/CT and whole body 1.5 T MRI, including DWI, for the detection of bone metastases in high risk breast and prostate cancer patients: SKELETA clinical trial. *Acta Oncol* 2016;55(1):59-67.
146. Kwee TC, Takahara T, Ochiai R, Katahira K, Van Cauteren M, Imai Y, Nievelstein RA, Luijten PR. Whole-body diffusion-weighted magnetic resonance imaging. *Eur J Radiol* 2009;70(3):409-417.
147. Lu H, Ge Y. Quantitative evaluation of oxygenation in venous vessels using T2-Relaxation-Under-Spin-Tagging MRI. *Magn Reson Med* 2008;60(2):357-363.
148. Stroman PW, Wheeler-Kingshott C, Bacon M, Schwab J, Bosma R, Brooks J, Cadotte D, Carlstedt T, Ciccarelli O, Cohen-Adad J. The current state-of-the-art of spinal cord imaging: methods. *Neuroimage* 2014;84:1070-1081.
149. De Foer B, Vercruyse J-P, Bernaerts A, Maes J, Deckers F, Michiels J, Somers T, Pouillon M, Offeciers E, Casselman JW. The value of single-shot turbo spin-echo diffusion-weighted MR imaging in the detection of middle ear cholesteatoma. *Neuroradiology* 2007;49(10):841-848.
150. Burakiewicz J, Charles-Edwards GD, Goh V, Schaeffter T. Water-fat separation in diffusion-weighted EPI using an IDEAL approach with image navigator. *Magn Reson Med* 2015;73(3):964-972.
151. K-P Hwang JM, A.J. Madhuranthakam, E. T. Han, W. Sun, Z. W. Slavens, D. C. Alsop. Diffusion weighted SSFSE with Dixon fat-water separation. Proceedings of the ISMRM, Toronto 2008.
152. Hwang K-P, Ma J. Feasibility of water-fat separation with diffusion weighted EPI. 2011 2011; Montreal, Quebec, Canada.
153. Wang X, Pirasteh A, Brugarolas J, Rofsky NM, Lenkinski RE, Pedrosa I, Madhuranthakam AJ. Whole-body MRI for metastatic cancer detection using T2-weighted imaging with fat and fluid suppression. *Magn Reson Med* 2018.

154. Wang XGJSP, Marco C.; Lenkinski Robert E.; Madhuranthakam, Ananth J. Volumetric T2-weighted and FLAIR Imaging of Spine with Uniform Fat Suppression in a Single Acquisition. 2017; Honolulu, HI, USA. p 0191.
155. Alsop DC. Phase insensitive preparation of single-shot RARE: Application to diffusion imaging in humans. *Magn Reson Med* 1997;38(4):527-533.
156. Jenkinson M. Fast, automated, N-dimensional phase-unwrapping algorithm. *Magn Reson Med* 2003;49(1):193-197.
157. Chow LC, Bammer R, Moseley ME, Sommer FG. Single breath-hold diffusion-weighted imaging of the abdomen. *J Magn Reson Imaging* 2003;18(3):377-382.
158. Kristoffersen A. Optimal estimation of the diffusion coefficient from non-averaged and averaged noisy magnitude data. *J Magn Reson* 2007;187(2):293-305.
159. Mikayama R, Yabuuchi H, Sonoda S, Kobayashi K, Nagatomo K, Kimura M, Kawanami S, Kamitani T, Kumazawa S, Honda H. Comparison of intravoxel incoherent motion diffusion-weighted imaging between turbo spin-echo and echo-planar imaging of the head and neck. *Eur Radiol* 2018;28(1):316-324.
160. Deng J, Miller FH, Salem R, Omary RA, Larson AC. Multishot diffusion-weighted PROPELLER magnetic resonance imaging of the abdomen. *Invest Radiol* 2006;41(10):769-775.
161. Breuer FA, Blaimer M, Heidemann RM, Mueller MF, Griswold MA, Jakob PM. Controlled aliasing in parallel imaging results in higher acceleration (CAIPIRINHA) for multi-slice imaging. *Magn Reson Med* 2005;53(3):684-691.
162. Verma SK, Nagashima K, Yaligar J, Michael N, Lee SS, Xianfeng T, Gopalan V, Sadananthan SA, Anantharaj R, Velan SS. Differentiating brown and white adipose tissues by high-resolution diffusion NMR spectroscopy. *J Lipid Res* 2017;58(1):289-298.
163. Boss M, Chenevert T, Waterton J, Morris D, Ragheb H, Jackson A, DeSouza N, Collins D, Van Beers B, Garteiser P. Temperature-controlled isotropic diffusion phantom with wide range of apparent diffusion coefficients for multicenter assessment of scanner repeatability and reproducibility. *Proc 22nd Int Soc Magnet Reson Med* 2014;4505.
164. Wang X, Reeder SB, Hernando D. An acetone-based phantom for quantitative diffusion MRI. *J Magn Reson Imaging* 2017;46(6):1683-1692.

165. Vos SB, Tax CM, Luijten PR, Ourselin S, Leemans A, Froeling M. The importance of correcting for signal drift in diffusion MRI. *Magn Reson Med* 2017;77(1):285-299.